

Robust stability analysis
of power electronic systems

Sharmila Sumsurooah (MSc)

Submitted to the University of Nottingham for the degree of Doctor of Philosophy,
October 2016.

Abstract

Power electronics is the enabling technology that can put transportation on a more sustainable pathway. The key problem with power electronic (PE) systems is that they are prone to instability. Classical techniques are insufficient at assessing the stability of these systems, as they do not take into account the uncertain nature of physical systems. This thesis presents the structured singular value-based μ method as an effective, reliable and robust stability analysis approach that justifiably incorporates uncertainties which are inherently present in physical systems.

Although the μ approach has numerous benefits, it has a few drawbacks that tend to make it hard to apply. Its theoretical framework remains complex. The practical approaches to applying the μ method to PE systems seem lacking in the literature. The μ approach is generally applied to linear system models while most systems are non-linear in nature. This thesis demonstrates the applicability of the μ method to PE systems, by addressing these limitations. The work first brings deeper and clearer insights into key concepts of μ theory. It demonstrates the significance and usefulness of the robust stability measure μ in the space of multiple parametric uncertainties, through the concept of the hypercube. Secondly, it presents several practical approaches to applying the μ method to PE systems. Finally, it develops a modelling methodology that converts a non-linear system to an equivalent linear model, suited for μ analysis. The findings are supported by simulation and experimental results of the buck converter, permanent magnet machine drive, ideal constant power load and resistance-inductance-capacitance systems.

This thesis provides the design engineer with some crucial theoretical and practical tools for applying the μ approach to both linear and non-linear models of PE systems, while showing how to reap the full benefits of the method. It is the author's belief that the μ method can be used as widely as classical methods, and to great effect.

Acknowledgements

“To do a PhD or not to do a PhD?” That was the hard question which I struggled with four years ago. After reaching the journey’s end about a month back, and now knowing what the path entails, would I advise my former self to set forth on the great adventure or not? Oh yes, I would! The labyrinth, with its pits and falls, honed and shaped both the intellect and the character. Self-doubt was tamed and turned into self-confidence. Challenges awakened the dormant intelligence of the wider mind, leading to a number of delicious hurrah moments along the way.

During the PhD odyssey, guidance from the wise certainly saved me from floundering excessively. Dr Milijana Odavic, a yardstick for research excellence, gave me no choice but be driven to set and maintain the loftiest of standards. “Apply and test the big idea on a simple circuit”, as advised by Professor Greg Asher, worked like a miracle and set the project on firm foundations. Working with Dr Dushan Boroyevic at CPES was a privilege. His passion for power electronics is contagious and he sure inspired me in my journey. When Dr Serhiy Bozhko hammered home the need for me to assert the novelty of my work, it finally dawned upon me that I had in fact contributed to new knowledge. The four years felt even more worth it.

The journey was strewn with plenty of perks such as my travels to Toronto, Aachen, and amazing cities in Japan. Living in Blacksburg, USA gave me an exposure to a wider world and new ways of thinking. My family was very supportive about my return to student status. My friends at the Tower Building and in different parts of the world, over coffee breaks and over VoIP uplifted my spirits during good and less good times. Today, I feel more robust in attitude and intellectual acumen, and ever more enthusiastic to meander through the next maze of exploration of the mind and the inner intelligence.

List of Terms

CO_2 - Carbon dioxide

DC - Direct current

AC - Alternating current

CPL - Constant power load

EMA - Electromechanical actuator

EPS - Electrical power system

$ESAC$ -Energy source analysis consortium

$GMPM$ - Gain Margin Phase Margin

LC -Inductor capacitor

LFT - Linear fractional transformation

LTI - Linear time invariant

MEA - More electric aircraft

MET - More electric transport

$MIMO$ - Multi input multi output

PE - Power electronic

PM - Permanent magnet

RLC -Resistor inductor capacitor

$SISO$ - Single input single output

SSV - Structural singular value

Z_i - Input impedance

Z_o - Output impedance

μ - Structural singular value

$\underline{\mu}$ - μ lower bound

$\bar{\mu}$ - μ upper bound

Contents

1	Introduction	2
1.1	Motivation	2
1.1.1	More electric transport	2
1.1.2	System stability	4
1.1.3	Robust stability	11
1.1.4	μ method	13
1.2	Research objectives	17
1.3	Contributions	18
1.4	Thesis structure	19
1.5	Published Papers	20
2	Theoretical framework	22
2.1	Introduction	22

2.2	Uncertain system model	23
2.3	Linear fractional transformation	24
2.4	Structural singular value (μ)	27
2.4.1	The μ framework	27
2.4.2	μ bounds	29
2.4.3	Robust stability margin ($1/\mu$)	31
2.5	Applicative example	32
2.5.1	LFT modelling	33
2.5.2	μ analysis	41
2.6	Limitations of the μ approach	44
2.6.1	Problem of convergence of the μ lower bound	44
2.6.2	Size of the uncertainty matrix	46
2.7	Conclusion	47
3	μ approach to robust stability domains	49
3.1	Introduction	49
3.2	Modelling of an EPS with an ideal CPL	51
3.2.1	Non-linear model of the ideal CPL	51
3.2.2	Small-signal ac model of the ideal CPL	52

3.2.3	Linear model of the ideal CPL	53
3.2.4	The EPS with the ideal CPL	55
3.3	Analytical assessment of system stability	57
3.4	System with single parametric uncertainty	59
3.4.1	μ analysis	59
3.4.2	Analytical verification	61
3.4.3	Robust stability domains	63
3.5	System with two parametric uncertainties	64
3.5.1	μ analysis	64
3.5.2	Analytical verification	66
3.5.3	Stability domains	66
3.5.4	Robust stability domains	69
3.6	System with three parametric uncertainties	71
3.6.1	μ analysis	71
3.6.2	Analytical verification	73
3.6.3	Stability domains	74
3.6.4	Robust stability domains	80
3.7	System with multiple parametric uncertainties	83

3.8	Conclusion	84
4	A practical approach to μ analysis	86
4.1	Introduction	86
4.2	Modelling of the buck converter for μ analysis	88
4.2.1	The experimental buck converter	88
4.2.2	Power stage model	90
4.2.3	Controller model	96
4.2.4	Closed loop controlled converter model	97
4.3	Model refinement	99
4.3.1	Initial simulation model	100
4.3.2	Individual system components models	100
4.3.3	Refined system model	102
4.4	Load uncertainty	104
4.4.1	μ analysis	105
4.4.2	Experimental results in time domain	107
4.4.3	Experimental results in frequency domain	109
4.4.4	Simulation time	112
4.5	Source impedance uncertainty	114

4.5.1	μ analysis	114
4.5.2	Experimental results	116
4.5.3	Results analysis	117
4.6	Temperature uncertainty	119
4.6.1	Uncertain parameters	119
4.6.2	μ analysis	120
4.6.3	Simulation verification	121
4.6.4	Results analysis	122
4.7	Model uncertainties	123
4.7.1	System with no model uncertainties	124
4.7.2	System with model uncertainties	125
4.7.3	Results analysis	128
4.8	Conclusion	130
5	A modelling methodology for μ analysis of non-linear systems	132
5.1	Introduction	132
5.2	Permanent magnet machine drive system	134
5.2.1	System structure	134
5.2.2	Experimental hardware	136

5.3	Modelling methodology	138
5.3.1	Symbolic linearisation	138
5.3.2	State space matrix elements expressed in terms of system parameters and inputs	140
5.3.3	Rational approximation of non-rational terms	141
5.3.4	The equivalent linear model	142
5.3.5	Validity of the equivalent linear model over a range of operating points	142
5.4	Load uncertainty	145
5.4.1	LFT modelling	146
5.4.2	μ analysis	147
5.4.3	Simulation results	150
5.4.4	Experimental results	151
5.4.5	Discussion	151
5.5	Effect of parameter variations on stability robustness	152
5.5.1	System frequency	153
5.5.2	Bandwidth of the DC-link voltage filter	153
5.5.3	Natural frequency of the speed loop	155
5.5.4	Discussion	156

5.6	Conclusion	156
6	Conclusions	158
6.1	Research outcomes	159
6.1.1	Theoretical aspects	159
6.1.2	Practical aspects	160
6.1.3	Application to non-linear systems	162
6.1.4	Research summary	163
6.2	Future research	164
A	Computational aids	174
A.1	μ analysis	174
A.2	Problem of convergence of the μ lower bound	175
A.3	Accuracy of μ bounds	176
A.4	Accuracy of the upper bound	176
B	Experimental measurements of input impedance	177

List of Figures

1.1	A DC voltage regulator behaving as a CPL to the AC power supply	5
1.2	An actuator system behaving as a CPL to the AC power supply	6
1.3	An ideal CPL representing tightly controlled power conversion systems	6
1.4	Characteristic curve of an ideal CPL	7
1.5	Linear model of an ideal CPL	7
1.6	Effect of bandwidth on the negative impedance behaviour of a DC/DC buck converter	9
2.1	Uncertain parameters (a) P as an LFT (b) $1/l$ as an LFT	25
2.2	Uncertain system (a) the original uncertain system in state space form (b) indeterminate uncertainties “pulled” out of the system using LFT	26
2.3	Uncertain system (a) in the LFT or $N\Delta$ form (b) stability depends on $M\Delta$ loop where $M = N_{11}$	27
2.4	Representative figure to illustrate μ bounds and robust stability margin	31
2.5	Robust stability margin for a system with a single parametric uncertainty	32

2.6	<i>RLC</i> circuit	33
2.7	Basic block diagram of the example <i>RLC</i> circuit	34
2.8	Block diagram of the example <i>RLC</i> circuit with uncertainties in r, l, c	35
2.9	<i>RLC</i> system (a) μ chart to predict critical r (b) zoomed area near peak of μ chart	42
2.10	<i>RLC</i> system (a) μ chart to predict critical r, l, c (b) zoomed area near peak of μ chart	43
2.11	<i>RLC</i> system - μ bounds to predict critical r , with no added complexity	45
3.1	Non-linear model of the ideal CPL	51
3.2	Characteristic curve of the ideal CPL	52
3.3	Small-signal model of the ideal CPL	53
3.4	Linear model of the ideal CPL	54
3.5	Single uncertain parameter system (a) μ chart to determine critical P_{in} (b) zoomed area near peak of μ chart	60
3.6	Single uncertain parameter system - Plot of eigenvalues based μ lower bound predictions, (*) eigenvalues with nominal $P_{in} = 10.4 W$, (o) eigenvalues with critical $P_{in} = 11.53 W$	62
3.7	Single uncertain parameter system - Largest linear segment of coordi- nate size $(1/\mu)$ centred about nominal point within which system is robustly stable	63

3.8	Two uncertain parameters system (a) μ chart to determine critical C_{in} and P_{in} (b) zoomed area near peak of μ chart	65
3.9	Two uncertain parameters system - Points A, B, C chosen to illustrate construction of stability domain	67
3.10	Two uncertain parameters system - stability domain from μ analysis and analytical method	68
3.11	Two uncertain parameters system - rectangle centred about nominal point and connecting point A	69
3.12	Two uncertain parameters system - rectangle centred about nominal point and connecting point C	70
3.13	Two uncertain parameters system - largest square of coordinate size $(1/\mu)$ centred about nominal point and connecting point B, within which system is robustly stable	70
3.14	Two uncertain parameters system (a) μ chart to determine critical C_{in} , L_{in} , P_{in} (b) zoomed area near peak of μ chart	72
3.15	Three uncertain parameters system - points A, B, C chosen to illustrate construction of stability domains	75
3.16	Three uncertain parameter system - μ lower bound chart translated into parametric space	76
3.17	Three uncertain parameters system - stability boundary plane from analytical method and μ chart translated into parametric space . . .	77
3.18	Flow chart for computing the smallest critical uncertainty matrix for a given system frequency	78

3.19	Three uncertain parameters system - frequency curves for 700 Hz, 720.5 Hz and 750 Hz on stability boundary plane, obtained from analytical method	79
3.20	Three uncertain parameters system - part of the cuboid centred about the origin and connecting point A falls in the unstable region	81
3.21	Three uncertain parameters system - largest cube of coordinate size $(1/\mu)$ centred about nominal point and connecting point B, within which system is stable	82
3.22	Three uncertain parameters system - top view of Fig. 3.21	82
4.1	Circuit representation of the closed loop controlled buck converter with input filter	89
4.2	The experimental closed loop controlled buck converter with input filter	90
4.3	Model of the buck converter in steady state	94
4.4	Duty cycle D as a function of load R	95
4.5	System model refinement procedure	99
4.6	Output impedance of power supply estimated through curve fitting of experimental measurements	101
4.7	Input filter inductance including measuring cable resistance estimated through curve fitting of experimental measurements	101
4.8	Input filter capacitance estimated through curve fitting of experimental measurements	102

4.9	Validation of simulation model loop gain against experimental measurements of loop gain	103
4.10	Validation of simulation model input impedance against experimental measurements of input impedance	103
4.11	System with load uncertainty (a) μ chart to predict critical R (b) zoomed area near peak of μ chart	106
4.12	Experimental results for system with load uncertainty (a) system is at boundary of stability with $R = 1.63 \Omega$ from $t = 0.253 s - 0.503 s$ (b) zoomed area near $t = 0.253 s$	108
4.13	Experimental measurements of Z_o and Z_i at point X of buck converter for system with load uncertainty (i) at point C, system is stable with $R = 5.37 \Omega$ (ii) at point B, system is near boundary stability with $R = 1.62 \Omega$ (iii) at point A, system is unstable with $R = 1.02 \Omega$. . .	111
4.14	Zoomed view of the phase of the input impedance in Fig. 4.13	111
4.15	Nyquist plots of experimentally measured Z_o/Z_i for system with load uncertainty at point X of buck converter (a) system is stable with $R = 5.37 \Omega$ (b) system is unstable with $R = 1.02 \Omega$ (c) system is near boundary stability with $R = 1.62 \Omega$ (d) zoomed view of Fig. 4.15c . . .	113
4.16	System with uncertain load and $R_{in} = 185 m\Omega$ (a) μ chart to predict critical R (b) zoomed area near peak of μ chart	115
4.17	System with uncertain load and $R_{in} = 278 m\Omega$ (a) μ chart to predict critical R (b) zoomed area near peak of μ chart	115

4.18	Experimental results for system with uncertain load and $R_{in} = 185\text{ m}\Omega$ (i) top figure: system is stable with $R = 1.89\ \Omega$ (ii) middle figure: system is at boundary of stability with $R = 1.54\ \Omega$ (iii) bottom figure: system is unstable with $R = 1.50\ \Omega$	117
4.19	Experimental results for system with uncertain load and $R_{in} = 278\text{ m}\Omega$ (a) system is at boundary of stability with $R = 1.17\ \Omega$ at $t = 0.08\text{ s}$ (b) zoomed area near $t = 0.08\text{ s}$	118
4.20	System with temperature and load uncertainties - μ chart to predict critical resistive components R_{es} and load R	121
4.21	System with temperature and load uncertainties (a) top figure - voltage v_o , bottom figure - current i_o (i) at $t = 1.0\text{ s}$, $R = 1.1 \times 1.87\ \Omega$ (ii) at $t = 1.3\text{ s}$, $R = 1.87\ \Omega$ (iii) at $t = 1.6\text{ s}$, $R = 0.9 \times 1.87\ \Omega$, where $R = 1.87\ \Omega$ is the critical load predicted by μ analysis (b) zoomed area near $t = 1.3\text{ s}$	122
4.22	System with load uncertainty and no model uncertainty (case I) (a) μ chart to predict critical R (b) zoomed area near peak of μ chart . . .	125
4.23	System with load and model uncertainties - μ charts to predict critical R (a) for case II (b) case III	127
4.24	System with load and model uncertainties for case II (a) plot of eigen- values based on μ lower bound predictions, (*) eigenvalues with nom- inal parameters, (o) eigenvalues with critical parameters (b) zoomed view near the imaginary axis	128
5.1	The main elements of a distribution system of the aircraft power system architecture	135
5.2	Block diagram of the PM motor drive system	135

5.3	Averaged model of the system in Fig. 5.1	136
5.4	Polynomial approximation of the steady state DC-link voltage V_{outo} .	141
5.5	Polynomial approximation of the steady state DC-link voltage V_{outo} with $R_e = 3.6 \Omega$ and $w_r^* = 3000 \text{ rpm}$	144
5.6	Operating points with varying torque T_o and line resistance R_e . . .	145
5.7	Relationship between torque and the normalised disturbance in torque	147
5.8	System with uncertain torque (a) μ chart to predict critical T (b) zoomed area near peak of μ chart	148
5.9	Robust stability margin and hypercube for system with uncertain torque	149
5.10	Time domain simulation of DC-link voltage $v_{out}(t)$ (a) (i) at $t=4s$, $T = 0.95T_{cr}$ (ii) at $t=8s$, $T = T_{cr}$ (iii) at $t=12s$, $T = 1.05T_{cr}$, where T_{cr} is the critical torque (b) zoomed area near $t = 9.1 \text{ s}$	150
5.11	Experimental results and μ predictions of critical power with varying system frequency	154
5.12	Experimental results and μ predictions of critical power with varying bandwidth of the DC-link voltage filter	154
5.13	Experimental results and μ predictions of critical power with varying natural frequency of the speed loop	155
B.1	Practical implementation of input impedance measurements	179
B.2	Equipment set-up for input impedance measurements	179

List of Tables

2.1	Uncertain parameter for Case I	41
2.2	Uncertain parameters for Case II	43
3.1	Nominal values for system parameters	52
3.2	Single uncertain parameter system (case I) - the uncertain parameter	59
3.3	Single uncertain parameter system - μ analysis results	61
3.4	Single uncertain parameter system - μ analysis and analytical results	62
3.5	Two uncertain parameters system (case II) - the uncertain parameters	64
3.6	Two uncertain parameters system - μ analysis results	64
3.7	Two uncertain parameters system - Critical values of C_{in} , P_{in} from μ analysis	66
3.8	Two uncertain parameters system - μ analysis and analytical results	66
3.9	Two uncertain parameters system - μ lower bound for points A, B, C	67

3.10	Two uncertain parameters system - critical parameter values for points A, B, C	68
3.11	Three uncertain parameters system (case III) - the uncertain parameters	71
3.12	Three uncertain parameters system - μ analysis results	72
3.13	Three uncertain parameters system - critical values of C_{in} , L_{in} , P_{in} from μ analysis	73
3.14	Three uncertain parameters system - μ analysis and analytical results of critical P_{in} and f	74
3.15	Three uncertain parameters system - critical parameter values for points A, B and C	75
3.16	Three uncertain parameters system -maximum singular value of ma- trices 1, 2 and 3 on frequency curve 700 Hz	79
3.17	Three uncertain parameters system - smallest matrices on frequency lines 700 Hz, 720.5 Hz and 750 Hz	80
3.18	Three uncertain parameters system - μ computed from coordinate points on stability plane	80
3.19	Variation of robust stability margin with number of uncertain parameters	83
4.1	Nominal values for system parameters	91
4.2	Initial and measured values for the system parameters	104
4.3	Uncertain resistive load	105
4.4	System with load uncertainty - μ analysis results	107

4.5	System with load uncertainty - μ analysis and experimental results . . .	109
4.6	System with load uncertainty - Experimental measurements of Z_o and Z_i	112
4.7	System with load and model uncertainties - Evaluation of polynomial approximations of D	114
4.8	System with uncertain load and different R_{in} - μ analysis results . . .	116
4.9	System with uncertain load and different R_{in} - μ analysis and experimental results	116
4.10	Uncertainties in temperature and resistive components	119
4.11	System with temperature uncertainty - μ analysis results	120
4.12	System with temperature uncertainties - μ analysis and time domain simulation results	123
4.13	Effect of temperature on stability margin with D constant	123
4.14	Uncertainties in system model	124
4.15	System with load uncertainty and no model uncertainty- μ analysis results	125
4.16	System with load and model uncertainties - μ analysis results	127
4.17	Evaluation of system with load and model uncertainties	129
5.1	Nominal values for system parameters	137
5.2	Torque Uncertainty	145

Chapter 1

Introduction

1.1 Motivation

1.1.1 More electric transport

Transport accounts for nearly two thirds of the global crude oil consumption and about a quarter of carbon dioxide (CO_2) emissions [1],[2],[3]. The energy use and CO_2 emissions in this sector are predicted to increase by 80% by 2050 [1]. The major contributors of greenhouse effects are expected to be light duty vehicles (43%), trucks (21%), aviation (20%) and shipping(8%) by 2050 [1]. Buses and rails are already sustainable modes of transport. In order to mitigate the impact of the emissions on climate change, the Intergovernmental Panel on Climate Change recommends a reduction of at least 50% in global CO_2 emissions by 2050 [1]. This target cannot be met unless there is a deep cut in CO_2 emissions from the transportation sector. On the other hand, independently of climate policy actions, the projections are that fossil fuel reserves will become exhausted within the next 50 years. If a more sustainable future is to be achieved, the issues of greenhouse emissions and energy security are to be addressed at this very point in time. One of the long-term solutions may well

lie in both the adoption of current best technologies and in the development of more advanced technologies, in all sectors including transportation [1]. A shift towards more efficient modes of transport, including the “more electric transport” (MET) are not only needed but seem inevitable.

The “more electric aircraft” (MEA) is a good example of the MET [4]. Although the electrical power system (EPS) of the MEA is different from those of the more electrical road vehicles, rails and ships, they share similar characteristics and benefits. In conventional aircraft, power is generated by engines from fuel. The bulk of the power is used for propulsion; the remainder is transformed to hydraulic, pneumatic, mechanical and electrical power to supply different loads in the aircraft [5]. Pneumatic power is used for the environmental control system (ECS) and wing anti-icing [5]. Hydraulic energy is used to power flight controls and landing gear [5]. Mechanical systems are driven by mechanical power through gearboxes [5]. Electrical power is used for lighting, avionics and commercial loads [5]. Moving towards the MEA involves increasing the electrical power generation and distribution capability of the aircraft to supply most of the aforementioned loads. This shift towards electricity rests on the development power electronics. It is the enabling technology that can contribute to high efficiency improvements in the aircraft, based on its distinctive features such as high power capability and controllability [6].

Power electronic technology is paving the way towards the more-electric engine and more-electric loads in the aircraft. The engines of the MEA will be started with in-built starter/generator instead of high pressure air [4]. The vanes to control airflow to the engine central core will be driven by PE converters. Power electronics will enable fuel pumps to run at their optimum speed in according with prevailing operating conditions [4]. This will significantly reduce wasted pumping energy. A large part of the aircraft loads, which run on pneumatic or hydraulic energy, will be controlled by PE converters, leading to further increase in efficiency [4]. These include environmental control system and wing anti-icing. Pressurisation will be performed by electrically powered compressors. Most hydraulic and pneumatic actuators will be replaced by electromechanical actuators (EMA) [5],[7]. Further, flight control systems

and flight control actuation are expected to be PE-based. Of note is that many of these functions are already implemented on current aircraft such as the Boeing 787 Dreamliner [4].

In the face of growing greenhouse emissions and declining fossil fuel reserves, the world, now more than ever, needs to move towards a more sustainable and truly low CO_2 future [1]. In this effort, transport needs to be put on a more sustainable pathway [1]. This implies the partial to complete electrification of all transport modes. And power electronics certainly lies at the heart of this technology transition.

1.1.2 System stability

Power electronic driven loads have numerous benefits. However, one key drawback is that they are prone to instability. As the aircraft electrical network becomes larger and more complex, the multitude of PE-based loads can thus challenge the stability of the EPS [8],[9],[10]. This is owing to the fact that the loads interfaced through power electronic converters exhibit constant power load (CPL) behaviour, under fast controller actions [11],[12]. They are seen in the network as negative impedances [12]. It is the negative impedance of the PE-based loads, when combined with input filter impedances, that may drive the system to instability. The CPL behaviour of two dominant PE-based subsystems in the MEA architecture are presented herein for illustration, together with the non-linear and linear models of the ideal CPL.

1.1.2.1 Constant power load

The DC/DC converter is an important component of the MEA architecture. It is commonly used to supply certain avionics DC loads [7]. Fig. 1.1 depicts such a converter connected to a resistive load [7]. Power system applications for the DC/DC converter requires the output voltage v_o to remain fairly constant despite perturbations in the input line voltage and step changes in load currents. This is achieved

by having a compensator in the negative feedback loop of the converter, which automatically adjusts the duty cycle under various conditions of disturbances, so as to keep the output voltage v_o constant and close to the reference voltage v_{ref} [13]. Since the electrical load as well as the output voltage are constant in steady state condition, the power supplied to the load is constant. With the converter efficiency considered unvarying, the input power P_{in} drawn from the source is also constant. The DC/DC buck converter, which is a commonly employed in the aircraft EPS, is further examined in Chapter 4.

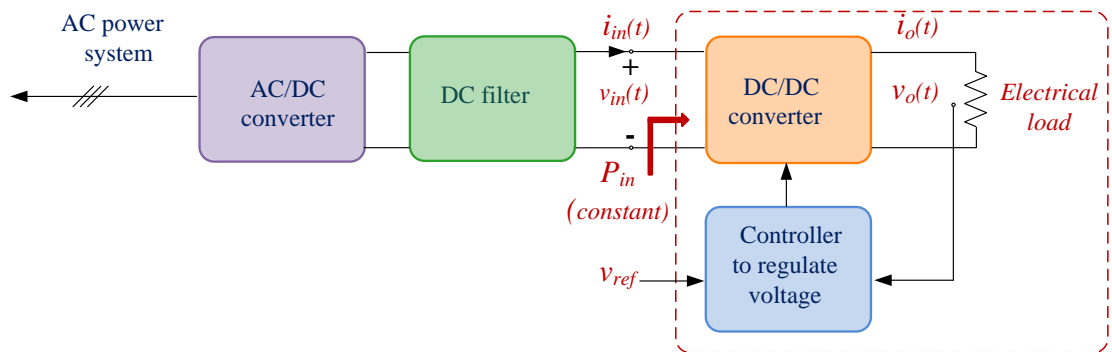


Figure 1.1: A DC voltage regulator behaving as a CPL to the AC power supply

Another key component of the aircraft EPS is the DC/AC converter. It is employed to drive loads such as flight control actuators [7]. Fig. 1.2 depicts such a system where the controller regulates the speed w_r of a permanent magnet (PM) machine such that it follows the reference speed w_r^* [7]. Since the speed w_r as well as the torque T are constant at a given operating point, the power supplied to the load is constant. Considering that the losses of the motor and converter are constant, the input power P_{in} drawn from the source is also constant. The DC/AC PM machine drive system is examined in greater detail in Chapter 5.

The aforementioned examples of the power electronics driven loads exhibit CPL behaviour. Under infinitely fast controller actions, they can mathematically be represented as ideal CPLs, as shown in Fig. 1.3.

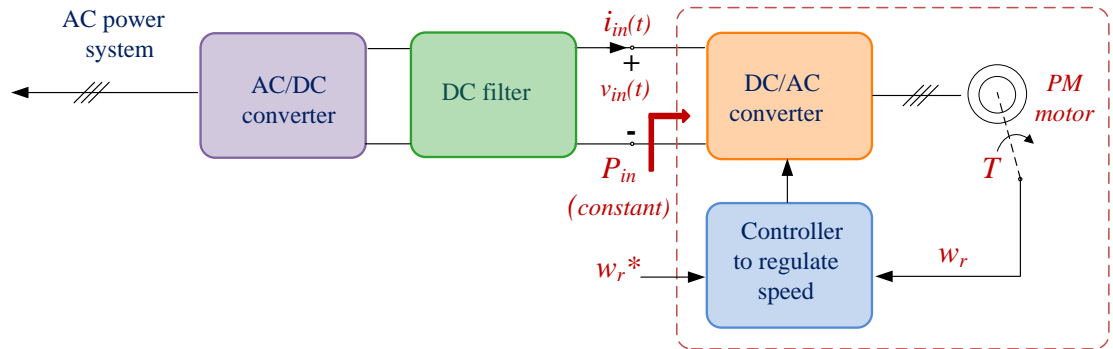


Figure 1.2: An actuator system behaving as a CPL to the AC power supply

The CPL characteristics are depicted in the non-linear equation (1.1) and in the curve in Fig. 1.4.

$$i_{in}(t) = \frac{P_{in}}{v_{in}(t)} \tag{1.1}$$

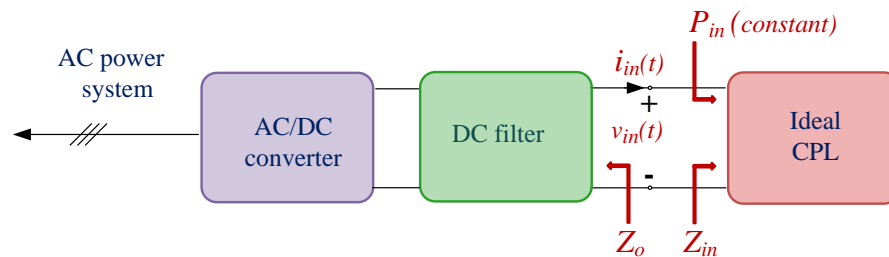


Figure 1.3: An ideal CPL representing tightly controlled power conversion systems

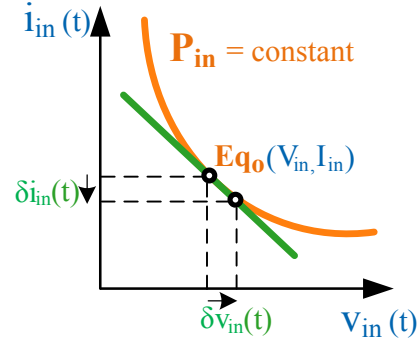


Figure 1.4: Characteristic curve of an ideal CPL

The ideal CPL can be represented by a linear model under steady state conditions. This is shown at the operating point E_{qo} on the curve in Fig. 1.4. The linear model of the ideal CPL is depicted by (1.2) and the circuit model in Fig. 1.5. Equation (1.2) can be derived from the partial differentiation and tangent line approximation of (1.1). The ideal CPL will be examined in more detail Chapter 3.

$$i_{in}(t) \approx -\frac{P_{in}}{V_{in}^2}v_{in}(t) + \frac{2P_{in}}{V_{in}} = \frac{1}{(-R_{cpl})}v_{in} + I_{cpl} \quad (1.2)$$

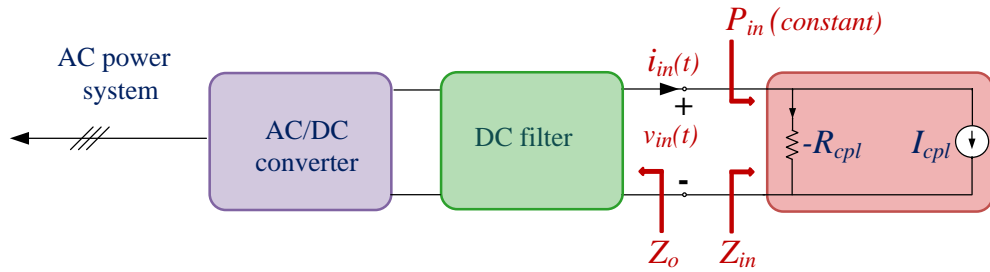


Figure 1.5: Linear model of an ideal CPL

At any given operating point, the input current and input voltage to the converter system may be represented by DC values (V_{in}, I_{in}) , as shown in Fig. 1.4. If the

voltage increases by $\delta v_{in}(t)$, the input current has to decrease by $\delta i_{in}(t)$ to keep the input power P_{in} constant [7],[12]. Hence, while the instantaneous impedance V_{in}/I_{in} is positive, the incremental impedance $(\delta i_{in}(t)/\delta v_{in}(t))$ is negative as shown in Fig. 1.4. This negative impedance, also represented by $-R_{cpl}$ for the ideal CPL, can lead to stability issues within the network, as will be described in the subsequent section.

1.1.2.2 Issue of stability

The negative impedance of the PE-based loads, when combined with input filter impedances, under certain circumstances, may cause the system to oscillate and become unstable [14]. This phenomenon can be more clearly explained through the Nyquist stability criterion. An EPS can be viewed as a cascade of its source and load components. The transfer function of the interconnected system is given by (1.3), where F_A and F_B are the transfer functions of the source and load subsystems respectively, and T is referred to as the minor loop gain [15],[16],[17]. As illustrated in Fig. 1.3 and 1.5, Z_o and Z_i are the output and input impedances of the source and load subsystems respectively.

$$F_{AB} = \frac{F_A F_B}{1 + T}, \quad \text{with} \quad T = \frac{Z_o}{Z_i} = \frac{|Z_o|}{|Z_i|} \angle(\phi_{zo} - \phi_{zi}) \quad (1.3)$$

According to the Nyquist stability criterion, for the system to be stable, $1 + T$ must not have any roots in the right half plane [14],[15]. It is seen from (1.3), that if T equals -1 , the denominator becomes zero and the transfer function F_{AB} tends to infinity. At this point, the system oscillates and is at the boundary of stability. For a system to be stable, the Nyquist contour must not encircle the point $(-1,0)$ [14].

In order to illustrate the issue of stability, a DC/DC buck converter connected to an input LC filter is examined. This is an example of the EPS shown in Fig. 1.1. The buck converter, with an efficiency of 93 %, draws an input power P_{in} of 17.2 W from the source, to feed a resistive load of 16 W, under steady state condition. Under

infinitely fast controller action, the buck converter can be represented as an ideal CPL of 17.2 W, as shown in Fig. 1.3 and 1.5. The buck converter and its ideal CPL representation are examined in later Chapters 4 and 3 respectively. Since these systems are being used for the purpose of illustration herein, they are not defined at this stage.

The input impedance of the buck converter, measured in simulation at different values of its bandwidths (2.8 kHz, 4.0 kHz, 15.3 kHz, 91 kHz), are shown in Fig. 1.6. It can be observed from the chart in Fig. 1.6, that the converter behaves as a negative resistance at low frequency with its phase being close to -180° . Further, it is noted from the chart that the negative resistance or CPL behaviour of the buck converter tends to prolong over a wider range of frequency under tighter controller action or increasing bandwidth. The ideal CPL representation of the buck converter is also shown in Fig. 1.6. It is equivalent to the negative resistance $-R_{cpl}$, with a magnitude of 27 dB and a phase of -180° over the entire frequency range.

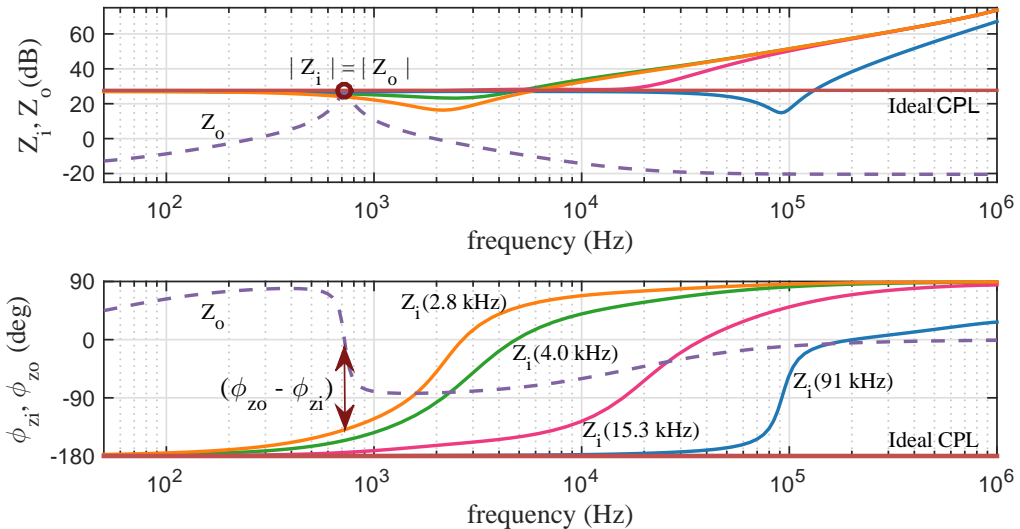


Figure 1.6: Effect of bandwidth on the negative impedance behaviour of a DC/DC buck converter

In addition, the output impedance of the LC input filter, including the power supply, is shown in Fig. 1.6. According to Middlebrook criterion, $|Z_o| \ll |Z_i|$ is a sufficient

condition for the stability of the system [14]. For cases where the input impedance $|Z_i|$ decreases or the output impedance $|Z_o|$ increases, at some point $|Z_i|$ may be equal to $|Z_o|$, as shown in Fig. 1.6. At that point, if $\angle(\phi_{zo} - \phi_{zi}) = 180^\circ$, which will cause T , as shown in (1.3), to be equal to -1 , the system will reach boundary stability. In order to keep the system stable, it is clear from Fig. 1.6, that the phase difference $\angle(\phi_{zo} - \phi_{zi})$ should be kept as small as possible and far from the critical 180° value. However, when a converter is tightly controlled, $\angle\phi_{zi}$ tends to -180° . This increases the likelihood of the phase difference between source and load impedances reaching 180° , and leading the system to instability. It is the interaction of the negative impedance of the PE-based load with the impedance of the input filter that tends to make the system susceptible to instability.

1.1.2.3 Stability analysis

Stability assessment is thus crucial in the design of power electronic systems. It is to be emphasised that system stability can be analysed both at the small and large signal level. Small-signal analysis investigates the stability of an EPS when it is subject to small disturbances [7],[12],[15],[18]. The analysis is performed on a linear system model about a certain operating point [7],[12],[15],[18]. In contrast, large signal stability analysis investigates the system's behaviour under large disturbances including transients and sudden large changes in loads [19],[20]. The large signal stability of a simplified electric ship power system is assessed in [21] based on Lyapunov's theorem. Although stability assessment of large signal disturbances is important, the subject is not treated in this study. This work focusses on small-signal stability analysis, which is an important concern in the reliable operation of the system.

The issue of system stability is not confined to the electrification of the aircraft but extends to the other transport modes [3],[22]. As power electronics plays a key role in developing more sustainable modes of transport, there is a dire need to address the issue of stability. Stringent assessment techniques are required to ensure the stability of electrical network for the MET.

1.1.3 Robust stability

The stability of electrical power systems is generally assessed by using classical stability analysis techniques [23],[24]. These include the eigenvalue method, and impedance methods based on the Nyquist stability criterion. The eigenvalue theorem verifies that all the eigenvalues of the Jacobian system matrix evaluated at a given equilibrium point have negative real parts, as a condition for system stability [7],[25]. According to the Nyquist stability criterion, for a system to be stable, the Nyquist contour of the minor loop gain must not encircle the point $(-1,0)$ [14],[15]. The Middlebrook criterion and its extensions, which are based on the Nyquist criterion, provide sufficient, but not necessary conditions of stability. Middlebrook criterion requires that the source impedance be less than the load impedance to ensure system stability [14],[15],[17]. The method is known to be very practical. Yet, the results can be conservative which may lead to the design of larger filter than is actually required [15],[17]. A number of extensions to Middlebrook criterion, such as the Gain Margin and Phase Margin (GMPM) criterion, and the Energy source analysis consortium (ESAC) criterion, were later developed to reduce the conservatism of the design [15],[17]. The different methods define various forbidden regions which contain the point $(-1,0)$. The results are made less conservative by specifying less restrictive forbidden regions [15],[17].

The classical methods work on the nominal model of the physical system [7],[14]. The outcome of the stability assessment is therefore heavily dependent on the quality of the system model. The model may be refined to great detail by matching its response to that of the physical system. Yet, in practice, excessive model refinement is unlikely to be viable or practical. Further, the exact values of system components may not be known accurately. For instance, system parasitics, often hard to quantify, can have a significant influence on the quality of the model. The power supply and external filters, to be connected on site, may be unknown at the design stage. This may significantly alter the impedance of the power stage. In addition, electrical power systems may be exposed to large variations in their loads. Thus, it can be safely argued that, in practice, nominal system models are bound to contain uncertainties.

From another perspective, even though a nominal model is deemed to be accurate, it may not truly represent the actual system, which is generally subject to various operating conditions uncertainties. For instance, in aerospace applications power electronics based systems may be exposed to temperatures typically ranging from $-40\text{ }^{\circ}\text{C}$ to $125\text{ }^{\circ}\text{C}$ [26]. These large variations in temperature may have considerable effect on the properties of system components. Ageing is another factor which brings uncertainty to the system elements over time. Although an EPS is assessed as stable based on fixed parameters and conditions, it is questionable whether it continues to be stable in the face of all the aforementioned possible types of uncertainties.

Despite the fact that exact values of system components, system loads or operating conditions may not be known accurately, their range of variation can generally be estimated to good accuracy. For instance, the tolerance of most components can be obtained from data sheets. The variation of resistances can be computed from the range of change in operating temperatures. Uncertainty sets of power supply and filter impedances may be obtained based on possible make and type. Given that uncertainties seem to be inherent in EPS, it may be more natural to work around uncertain system models. In contrast with nominal models, uncertain models define both the nominal values and the possible range of variation of their parameters. The uncertain model is thus closer to the physical system. While classical methods are applied for stability analysis of nominal system models, a robust approach is needed for the stability assessment of uncertain system models. The structural singular value (SSV)-based μ approach is a robust stability method that incorporates all sources of uncertainties within the system [27],[28],[29].

It can be argued that uncertainties can be incorporated when using classical methods [7],[30]. In an attempt to include uncertainties in stability analysis, classical approaches such as the eigenvalue method are combined with the Monte Carlo simulation. This probabilistic stability assessment approach can be employed to determine probability density functions of critical eigenvalues but cannot guarantee to identify the most critical system scenarios with respect to stability [31],[32]. Additionally, [30] presents an admittance space stability analysis method that incorporates uncer-

tainties in the application of the classical impedance-based ESAC criterion approach. Yet, the aforementioned methods involve exhaustive iterations of parameter variations, linearisation at a number of equilibrium points and computation of eigenvalues or impedances. The approaches tend to be laborious. The authors in [30] have developed a software to make the process automatic. However, applying single input single output (SISO) methods to multi input multi output systems (MIMO) may not produce reliable results, as reported in a number of studies [31],[33].

The μ approach is a deterministic method, that can provide a direct measure of stability robustness of a system with respect to its uncertain elements. It is founded on the aforementioned concept of the uncertain system model. Hence, by working directly on an uncertain model, μ analysis eliminates the burden from a user of performing exhaustive iterations. Further, the μ approach has proven to produce reliable results in robust stability analysis of power systems subject to multiple simultaneous uncertainties [27],[33],[34],[35],[36].

Following the above discussion, it is evident that there is a need to ensure that an EPS is not only stable but robustly stable, i.e. it must remain stable in the face of all system uncertainties. This is especially important for safety-critical applications. This thesis presents the structural singular value based μ method as an effective and reliable stability robustness approach, that justifiably takes into account all possible system perturbations.

1.1.4 μ method

Important developments in the multivariable control theory since the early eighties have made the μ approach more rigorous and applicable, when compared to the early stages of its development [28]. However, despite its numerous advantages, the method has a few limitations, which could explain why it is still not as widely used as classical methods, as discussed herein.

1.1.4.1 Theoretical aspects

The mathematical complexity underlying the μ theorem is such that certain aspects of the approach are not well understood and interpretation thereof may not be evident from the engineering viewpoint [33]. In fact, a great amount of literature is devoted to the theoretical framework [27],[28],[29],[33],[35],[37]. It discusses linear fractional transformation (LFT), which is a modelling technique required to convert a system model into a form that is suitable for μ analysis. The theory also discusses the principle of SSV, which is a measure of stability robustness of the system. Understanding the μ theory is of utmost importance; yet, the practical significance and applicability of the key concepts are equally important. Unfortunately, this aspect is not widely discussed in the literature. Although the operation of LFT and the computation of μ remain complex, the processes have been automated with the help of software such as MATLAB[®] Robust Stability Toolbox and ONERA[®] Skew mu toolbox [38],[39],[40].

Another feature of the μ approach that adds to the aforementioned limitation is that μ cannot be computed as an exact value particularly for large problems, since the computational burden increases exponentially with the size of the problem. A lower bound and an upper bound are calculated instead of its exact value. It is to be pointed out that these bounds are usually interpreted from a theoretical rather than from a practical viewpoint. It has been reported in the literature that the method can be computationally expensive for the analysis of complex systems with a large number of uncertainties [34],[41]. However, a number of algorithms have been developed to reduce the gap between the μ bounds while maintaining reasonable computational time [34],[40],[42]. Further, the computation of μ is dependent on the types of uncertainties being considered. These can be structured parametric uncertainties, unstructured unmodeled dynamics or a combination of these two types of perturbations [27],[35]. Unmodeled dynamics group uncertainties that are often hard to quantify, such as perturbations arising outside the control bandwidth at high frequencies. They are often represented as frequency-dependent uncertain transfer functions. Of note is that this study focusses on parametric uncertainties, which is particularly relevant to engineering problems.

For the μ approach to be more applicable, a thorough understanding of the μ theory as well the practical implications of its key concepts is essential.

1.1.4.2 Practical aspects

Many works have proven that the μ approach can be applied to realistic models of power systems with successful results. Unfortunately, certain key aspects of the employed methodology have not been presented in sufficient detail, that would enable a user to reapply the method. Further, the practical approach to applying the method to power electronic based systems seems to be lacking in the literature.

The authors in [43],[44],[45],[46],[47] successfully apply μ analysis to determine the maximum power transfer of large scale power systems. The studies analyse the μ upper bound, however they do not evaluate the μ lower bound. Besides, the methodology applied through associated software is not discussed. The work in [48] investigates the maximum range of variation in the load, that a university campus microgrid can withstand before becoming unstable. The results, based on μ upper bound, are reported to be satisfactory, and in addition are shown to be less conservative as compared to Middlebrook method. However, the work neither discusses the conservatism in the μ upper bound nor presents the method employed. Although, the authors in [31] investigate the stability of the PE-based buck converter system, the focus of the work is, nonetheless, on μ sensitivity. This method identifies the system parameters which are most critical to stability robustness. The study shows that both Middlebrook method and Monte Carlo method, in contrast to the μ sensitivity approach, cannot be used reliably to identify the most critical parameters that cause instability. Certain works such as [34],[49] have treated the practical aspects of the μ approach in good depth. The work presented in [34] shows the practical approaches to using μ analysis for aeronautical applications. While the results are clearly examined, the systems analysed and the method employed are not presented in a manner that is comprehensive enough to reapply them. Further, [38],[49] and [50] demonstrate the use of the computational functions in MATLAB[®] Robust control toolbox. However,

the example systems deal mainly with the design and analysis of robust controllers. In addition, the computational functions, that are presented in these works, have long been replaced by new functions in the updated versions of the toolbox. The work presented in [51] applies μ analysis to a buck-boost converter. Nonetheless, the focus is on the design of a robust controller for the converter and similarly to previous studies, it does not present the method applied.

In order to make the μ approach more applicable, sufficient knowledge as regards its practical application, particularly to power electronic systems, is necessary. The methodology required to apply the μ method, through available software, needs to be presented in a manner comprehensive enough to enable a user to reapply it.

1.1.4.3 Application to non-linear systems

The μ method is generally applied for robust small-signal stability analysis of linear uncertain system models. However, most electrical power systems are generally non-linear in nature. The small-signal stability assessment of non-linear systems may be challenging in the face of uncertainties. This is due to the fact that small-signal stability analysis is performed on a linear model about a certain operating point; and depending on the amount of variations considered in the system, there may be an arbitrarily large number of linearised models to be generated and assessed, over a large range of operating points.

In order to analyse the small-signal stability of an EPS, the classical approach employs an extensive iterative process. For instance, [52] uses the eigenvalue method to determine the critical torque of the PM machine based electromechanical actuation system. Firstly, the operating range is divided into a finite number of points. Then, for each operating point, numerical linearisation is performed and eigenvalues are calculated. The iterative process has to be further refined until the critical parameter value is obtained to a satisfactory accuracy. The process can be laborious.

Few methods, proposed in the literature, have aimed to apply the μ method to non-

linear systems. A combined numerical and symbolic linearisation technique is presented in [41]. Another approach identifies the elements of state space matrices that vary with changes in operating conditions and system parameters, and then approximates those varying elements by polynomial functions [43],[44],[45],[46]. Yet, these methods, similarly to the classical approach, cannot fully take into account dependencies of operating points on parameter uncertainties and may lead to conservative results. Nonetheless, it should be noted that these techniques were proposed for larger power systems, for which the loss in accuracy in the results may be justified.

In order to make the μ approach more applicable power electronic systems, it is necessary to have adequate techniques that can extend the applicability of the method to non-linear systems, while ensuring accuracy of results.

1.2 Research objectives

Power electronic based systems plays a key role in moving towards more sustainable modes of transport. It is therefore essential that the issue of stability in PE-based systems be addressed in a rigorous manner. Classical methods are not sufficient to assess the stability of such EPS as they neglect uncertainties, which are inherent in the physical system. The μ approach is presented as a reliable method that can be employed to ensure the stability robustness of EPS, in the face of system uncertainties. Even though the μ method has great advantages, it also has a few drawbacks. First, its theoretical framework remains complex and is not always well understood. The practical significance of μ and its bounds is not always clear. Secondly, the practical approaches to applying the μ method to PE systems seem lacking in the literature. Finally, the μ approach is generally applied to linear system models while most systems are non-linear in nature.

The μ approach has numerous benefits as compared to classical methods. However, the aforementioned limitations may suggest why this robust method is not widely employed by design engineers. It is the author's belief that the μ approach can be

employed as commonly as the classical techniques and to great effect. In order to make the μ approach more application-friendly and to fully realise the benefits of the method, this work addresses its limitations, through the following key objectives.

- The first objective is to bring clearer and deeper insights into certain key theoretical aspects of the μ approach, in view of making it more applicable.
- The second objective is to demonstrate the practical and flexible aspects of the μ method, and present approaches to applying it to PE-based systems.
- The final objective is to extend the application of the μ method to non-linear systems, while reducing the conservativeness in the results.

1.3 Contributions

The research methods, that have been implemented to meet the aforementioned objectives, are presented in the main chapters of this thesis and are outlined in the next section. This effort has resulted in three main contributions.

- By extending and applying the concept of the hypercube to PE systems, this work provides important insights into the meaning and usefulness of the robust stability measure μ , for systems subject to multiple parametric uncertainties. The hypercube represents the largest normalised parametric space centred about the nominal point, within which robust stability is guaranteed.
- This study presents practical and flexible approaches to applying the μ method to PE-based systems. It demonstrates how different types of uncertainties, such as uncertainties in the model, the load and operating conditions, can be easily incorporated in the stability exercise, while employing the same system model and the same analysis tool.

- This thesis develops a general modelling methodology to represent a non-linear system by an equivalent linear state space model, that is suited for μ analysis. By expressing dependencies of operating points on system parameters, the developed modelling approach reduces conservativeness in the results.

1.4 Thesis structure

The thesis is organised in six main chapters.

Chapter 1 provides the motivation for this work and highlights the major contributions.

Chapter 2 presents the theoretical framework to the μ method, and illustrates the key concepts by applying them to the well established resistance-inductance-capacitance *RLC* circuit. The technique of LFT and the principle of SSV are discussed. Two different approaches to uncertain system modelling, based on LFT techniques, are analysed in detail. These include the interconnection of LFT models and Morton's method. Furthermore, the chapter examines the μ bounds and the associated robust stability margin. The main limitations of the μ method are discussed.

Chapter 3 applies the concept of the μ -based hypercube to a basic EPS connected to an ideal constant power load, to determine the robust stability domains within which the EPS can be guaranteed to operate safely. It demonstrates the applicability of the μ approach in evaluating stability robustness and robust stability domains of an EPS subject to multiple parametric perturbations. This is achieved by translating μ results from the frequency domain into the more perceivable parametric space. μ analysis predictions are evaluated against analytical results.

Chapter 4 demonstrates the practical approaches to μ analysis by applying it to the buck converter as an example EPS. The first part of the chapter applies μ analysis

to the refined model of the system, when it is subject to load uncertainties. The investigation is performed for source impedance of varying values. The μ predictions of the critical destabilising load are verified against experimental results performed both in the time domain and the frequency domain. The second part examines the robust stability margin of the EPS under extreme temperature variations. Finally, the chapter demonstrates how model uncertainties can be incorporated in stability analysis of a system. It evaluates the robust stability margin when model uncertainties are accounted for, as compared to the case when these uncertainties are neglected.

Chapter 5 develops a modelling method for robust stability analysis of non-linear EPS over a range of operating points and under parameter uncertainties. The proposed modelling approach is applied to a 4 kW permanent magnet (PM) machine drive. μ analysis, applied to the developed equivalent linear model of the EPS, is then used to predict the destabilising torque over a range of different operating points and parameter variations. The stability of the PM machine drive system has been analysed based on the classical eigenvalue method and also tested experimentally in [52]. The methodology, presented in this chapter, is validated by evaluating the predictions from μ analysis to the experimental reported in [52].

Chapter 6 discusses the significance as well as the implications of the findings presented in the thesis, and provides suggestions for future works.

1.5 Published Papers

- S. Sumsurooah, M. Odavic, and D. Boroyevich, “Modelling and robust stability analysis of uncertain systems,” in *Proceedings of the 2013 Grand Challenges on Modeling and Simulation Conference*, p.13, Society for Modeling & Simulation International, 2013.
- S. Sumsurooah, M. Odavic, and S. Bozhko, “Development of LFT-based models for robust stability analysis of a generic electrical power system over all oper-

ating conditions,” in *Electrical Systems for Aircraft, Railway, Ship Propulsion and Road Vehicles (ESARS), 2015 International Conference on*, pp. 1-6, IEEE, 2015.

- S. Sumsurooah, M. Odavic, S. Bozhko and D. Boroyevich, “Stability and robustness analysis of a dc/dc power conversion system under operating conditions uncertainties,” in *Industrial Electronics Society, IECON 2015 - 41st Annual Conference of the IEEE*, pp. 003110-003115, Nov 2015.
- S. Sumsurooah, M. Odavic, and S. Bozhko, “A modelling methodology for robust stability analysis of nonlinear electrical power systems under parameter uncertainties,” *IEEE Transactions on Industry Applications*, vol. 52 pp. 4416-4425, Sept. 2016.

Chapter 2

Theoretical framework

2.1 Introduction

Power electronic systems play a key role in the development of the more electric transportation. However, they are prone to instability and call for the adoption of robust stability assessment techniques. The μ approach is a robust tool that can be used effectively to assess the stability of such systems. One factor that tends to make the method hard to apply is the complexity of its theory, which is not always fully understood [27],[33]. This chapter aims to bring a good comprehension of the basic μ theory, in view of making the μ approach more applicable. The theoretical framework consists of certain key concepts which include the modelling technique of LFT as applied to uncertain system models, as well as the principle of structural singular value μ and its bounds.

The LFT technique, which forms the basis of the μ approach, is explained widely in the literature. It is described as a technique that is used to “pull out” uncertainties from the uncertain model. While the method is often discussed in theoretical terms, the authors in [35] and [38] illustrate LFT by applying it to a mechanical mass-spring-damper system. These studies have provided a good basis to further explore

the concept of LFT in this chapter. Even though the process of LFT, being extensive, is generally performed by the aid of associated software, understanding the basic steps involved in the process is important, prior to employing the μ approach.

While the principle of μ and the computation of its bounds are widely examined in the literature, the discussion is generally done from a mathematical viewpoint. Few works have tried to interpret the concepts from a practical or engineering stand point [34],[49]. μ can generally not be calculated as an exact value as it is computationally expensive. A lower and an upper bound are provided instead. A number of studies work with the μ upper bound. However, they neither discuss its conservative nature nor compare it with the μ lower bound [43],[44],[45],[47]. Yet, the authors in [38] suggest to use both bounds for a more reliable use of the μ approach. The examination of μ and its bounds, from an application point of view, seems lacking in the literature. Fortunately, [34] brings a clearer understanding of the μ bounds by discussing their implications on stability assessments. If the basic theory of the μ approach is unclear, its application will remain be a daunting task. Hence, there is a need to gather the dispersed knowledge of the key underlying concepts and bring a comprehensive examination of the μ framework.

This chapter provides a perspective on the modelling technique of LFT, as applied to uncertain system models. It examines two different approaches to LFT, namely the interconnection of LFT models and Morton's method. It then explores the theoretical framework of SSV by discussing the μ bounds and the μ -based robust stability margin. It illustrates the two approaches to LFT and the principle of μ by applying them to an example *RLC* circuit. The limitations of the μ approach are also discussed.

2.2 Uncertain system model

A great advantage of the μ approach is that it works with the uncertain system model as opposed to the nominal model [29],[35],[36],[37]. In practice, parameters of an actual system may vary within a certain range of the nominal values owing

to some perturbation effects such as parameter changes, noise, variation in material properties, design errors [35]. An uncertain system model considers not only nominal values of the system parameters but also the possible range of parameter changes [35]. In contrast, a system that is designed around fixed parameters is referred to as the nominal model. The advantage of designing around an uncertain system model is that it brings the model closer to the physical system. Standard techniques are sufficient to verify stability of nominal systems with no uncertainties. However to analyse stability of uncertain systems, the principle of structural singular value (μ) can be used. Prior to applying μ analysis, the system must be expressed in the linear fractional transformation (LFT) form [27],[36]. The aim is to verify that a system remains stable for all conditions that may arise within the defined uncertainty set, in which case it is said that the system is robustly stable. The systems dealt in this work are Multiple-Input-Multiple-Output (MIMO) systems that vary with frequency and are linear time-invariant (LTI). The focus of this study is on parametric uncertainties, which are particularly relevant to engineering problems.

2.3 Linear fractional transformation

LFT is a modelling technique which is employed to “pull out” the indeterminate part from the known part of a system model and place it in the feedback form. If a general uncertain parameter P is considered to be bounded in the region $[P_{min}, P_{max}]$, it may be represented in its normalised form δ_P bounded within $[-1, 1]$. It is easy to show that P can be modelled as an LFT in δ_P in the expression (2.1) and in the matrix form in Fig. 2.1a [35],[53]. It should be added that an inverse of an LFT is also an LFT. This is illustrated by the inverse of the parameter l in (2.2) and in the matrix form in Fig. 2.1b, where l is bounded within $[l_{min}, l_{max}]$. Considering that the parameters P and $1/l$ are constituent parts of a dynamic system, the input and output signals of the parameters with respect to the system, are denoted as u_{sp} , u_{sl} and y_{sp} , y_{sl} respectively, while $u_{\Delta P}$, $u_{\Delta l}$ and $y_{\Delta P}$, $y_{\Delta l}$ denote the outputs and inputs of δ_P and δ_l respectively, as shown in Figs. 2.1a and 2.1b [35],[49].

$$P = P_o + P_o P_{var} \delta_P, \quad \delta_P \in [-1, 1] \quad (2.1)$$

where $P_o = (P_{min} + P_{max})/2$

and $P_{var} = \frac{(P_{max} - P_{min})}{2} / \frac{(P_{max} + P_{min})}{2}$

$$1/l = 1/l_o - l_{var} \delta_l (1 + l_{var} \delta_l)^{-1} (1/l_o), \quad \delta_l \in [-1, 1] \quad (2.2)$$

where $l_o = (l_{min} + l_{max})/2$

and $l_{var} = \frac{(l_{max} - l_{min})}{2} / \frac{(l_{max} + l_{min})}{2}$

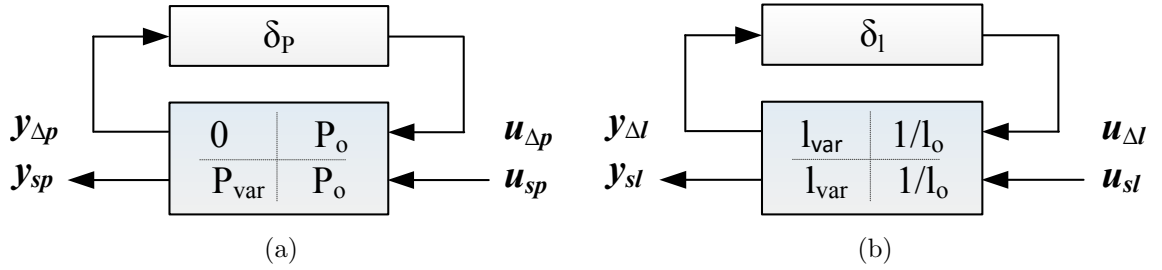


Figure 2.1: Uncertain parameters (a) P as an LFT (b) $1/l$ as an LFT

Similarly, the model of an entire system with parametric uncertainties can be represented in the LFT form [36],[50]. For the purpose of illustration, a general uncertain system expressed in the state space form with input u and output y , as shown in Fig. 2.2a, is considered. The elements of the state space matrix $\begin{pmatrix} A & B \\ C & D \end{pmatrix}$ are functions of either fixed or uncertain parameters. For instance, element A_{ij} of the state matrix A can be expressed as $A_{ij} = f_1(P_1, P_2, \dots, P_m)$ where P_1 to P_m denote uncertain parameters of the system [45]. Based on the technique of LFT, it is possible to extract the set of uncertainties in their normalised form and regroup them in the diagonal uncertainty matrix Δ as shown in Fig. 2.2b, where $\Delta = \text{diag}\{\delta_{P_1}, \delta_{P_2}, \dots, \delta_{P_m}\}$. As a result, the initial state space matrix is expanded to accommodate two sets of inputs namely u_Δ and u_s and two sets of output y_Δ and y_s as shown in Fig. 2.2b [35],[43].

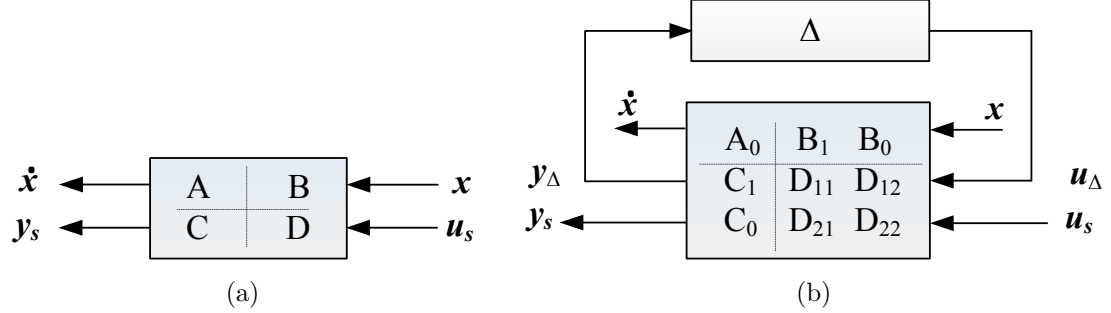


Figure 2.2: Uncertain system (a) the original uncertain system in state space form (b) indeterminate uncertainties “pulled” out of the system using LFT

The expanded state space matrix can be simplified by absorbing the “states” through the use of equations (2.3) - (2.6). In this manner, the state space matrix in Fig. 2.2b is converted into the $N\Delta$ configuration in Fig. 2.3a.

$$N_{11}(s) = C_1(sI - A_0)^{-1}B_1 + D_{11} \quad (2.3)$$

$$N_{12}(s) = C_1(sI - A_0)^{-1}B_0 + D_{12} \quad (2.4)$$

$$N_{21}(s) = C_0(sI - A_0)^{-1}B_1 + D_{21} \quad (2.5)$$

$$N_{22}(s) = C_0(sI - A_0)^{-1}B_0 + D_{22} \quad (2.6)$$

Further, the system matrices in Fig. 2.3a can be represented as three distinct equations (2.7) - (2.9). By rearranging these equations to eliminate u_Δ and y_Δ and expressing the output y_s in terms of the input u_s , the transfer function of the system is obtained as (2.10), if the feedback is well posed. The uncertainty matrix Δ is clearly distinguishable in (2.10) and is said to have been “pulled out” of the original uncertain system. Equation (2.10) is known as the upper linear fractional transformation $F_u(N, \Delta)$. It is interesting to note that with the disturbance Δ , in (2.10), being zero, the system is equivalent to $N_{22}(s)$, which is exactly the nominal transfer function of the uncertain system.

$$y_\Delta = N_{11} u_\Delta + N_{12} u_s \quad (2.7)$$

$$y_s = N_{21} u_\Delta + N_{22} u_s \quad (2.8)$$

$$u_\Delta = \Delta y_\Delta \quad (2.9)$$

$$F_u(N, \Delta) = \frac{y_s}{u_s} = N_{22} + N_{21}\Delta(I - N_{11}\Delta)^{-1}N_{12} \quad (2.10)$$

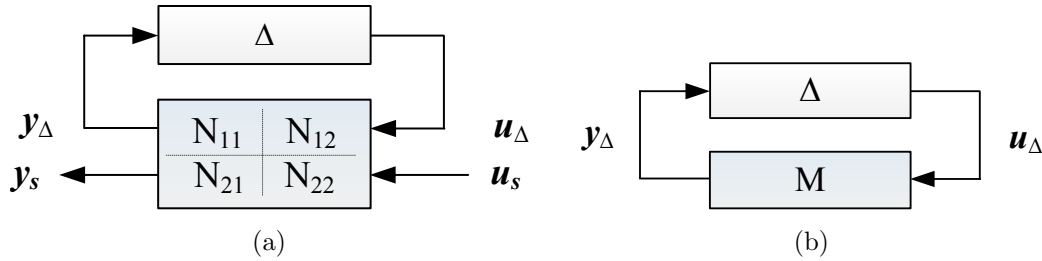


Figure 2.3: Uncertain system (a) in the LFT or $N\Delta$ form (b) stability depends on $M\Delta$ loop where $M = N_{11}$

2.4 Structural singular value (μ)

2.4.1 The μ framework

Referring to the general LFT expression (2.10), it can be seen that the only source that can cause the system $N\Delta$ to become unstable is the feedback term $(I - M\Delta)^{-1}$ where $M = N_{11}$ [36]. The stability of the whole system therefore rests on the stability of the subsystem $(I - M\Delta)^{-1}$. This is represented in Fig. 2.3b which can be seen as an extraction of the transfer function matrix in Fig. 2.3a.

The small gain theorem, upon which robust stability theorem is based, states that if the systems M and Δ are open-loop stable, the interconnected loop $M\Delta$ is also stable provided that the loop gain product is less than unity as given by (2.11) [49].

As defined in [49], $\|M\Delta\|_\infty$ describes “the maximum energy gain of the interconnected system and is decided by the peak value of the largest singular value of the frequency response matrix over the whole frequency axis”.

$$\|M\Delta\|_\infty < 1 \quad \text{and} \quad \|\Delta M\|_\infty < 1 \quad (2.11)$$

Generally uncertainty falls in two main categories namely structured parametric uncertainty and unstructured frequency-dependent unmodeled dynamic uncertainty [34],[38],[36]. The stability conditions, as defined in (2.11), are valid for unstructured uncertainties but do not consider the structure of the uncertainty matrix. In order to generalise the small gain theorem to include structured uncertainties, the determinant stability condition, which is based on the generalised Nyquist Theorem, is used. It states that the system $M\Delta$ in Fig. 2.3b is stable for all allowed perturbations if and only if : [29],[54]

$$\begin{aligned} \text{the complex function} \quad \det(I - M\Delta(jw)) \neq 0, \quad \forall w \in R \quad (2.12) \\ \text{or the eigenvalues} \quad \lambda_i(M\Delta) \neq 1 \end{aligned}$$

Based on the small gain theorem and the determinant stability condition, the robust stability condition for structured uncertainties is given by the structured singular value, as defined in (2.13).

$$\mu_\Delta(M) = \frac{1}{\min[\bar{\sigma}(\Delta) : \det(I - M\Delta) = 0, \Delta \text{ structured}]} \quad (2.13)$$

The structured singular value, commonly denoted as μ , identifies the smallest perturbation matrix (Δ) that destabilises the system by causing the location of system poles on to the imaginary axis [29],[35]. In fact, the robust stability margin, which

corresponds to the size of the critical perturbation matrix, is equal to $1/\mu$. SSV is a frequency-dependent matrix function which depends on both the system matrix $M(s)$ and the structure of Δ [29],[35]. The SSV theory gives necessary and sufficient conditions for stability robustness [27]. If μ is less than 1, the system is guaranteed to be stable for the entire uncertainty set.

2.4.2 μ bounds

There exists an arbitrarily large number of solutions to the robust stabilisation condition (2.13) [38],[49]. The computational burden of calculating μ increases exponentially with the size of the problem [27],[34],[37]. It is not computationally feasible to compute μ , particularly for large size problems [34]. The solution is thus to compute a lower bound $\underline{\mu}$ and an upper bound $\bar{\mu}$ instead of the exact value of μ . The μ bounds are defined in (2.14) [49]. The lower bound corresponds to the spectral radius of M , ($\rho(M)$), which refers to the largest value of all the eigenvalues of $M(s)$ [35]. The upper bound corresponds to the largest singular value of M i.e. $\bar{\sigma}(M)$ [35]. However the gap between the bounds in (2.14) can be very large. The transformation matrices U and V are introduced to provide tighter bounds on μ , as given in (2.15) [49].

$$\rho(M) \leq \mu_{\Delta}(M) \leq \bar{\sigma}(M) \quad (2.14)$$

$$\max_{U \in \mathcal{U}} \rho(UM) \leq \mu_{\Delta}(M) \leq \inf_{V \in \mathcal{V}} \bar{\sigma}(VMV^{-1}) \quad (2.15)$$

$$\text{where the lower bound } \underline{\mu} = \max_{U \in \mathcal{U}} \rho(UM) \quad (2.16)$$

$$\text{and the upper bound } \bar{\mu} = \inf_{V \in \mathcal{V}} \bar{\sigma}(VMV^{-1}) \quad (2.17)$$

The condition (2.16) is a non-convex problem. It can be solved as a non-convex optimisation problem, which may be computationally demanding. A non-convex problem may have multiple feasible regions, and each feasible region may contain multiple optimal solutions [55]. To identify whether the problem has a global solution when the objective function is unbounded, or to determine whether a local solution is

the global solution across all feasible regions is a hard problem, i.e. the computational time may increase exponentially with the size of the problem. The lower bound $\underline{\mu}$ is obtained as a local maximum to condition (2.16). This is depicted in Fig. 2.4, which has a purely illustrative significance. If the local maximum coincides with the global maximum, $\underline{\mu}$ is always equal to μ . However, this cannot be guaranteed. On the other hand, the upper bound $\bar{\mu}$ can be obtained as a solution to the condition (2.17). This is a convex problem with a unique maximum, as depicted in Fig. 2.4 [34]. It can be solved efficiently up to very large size, as a convex optimization problem. However, except for a few cases, $\bar{\mu}$ is generally higher than μ , and tends to be conservative [38],[49]. Yet, $\bar{\mu}$ can be used as a measure of the maximum possible error in the lower bound. This can be estimated by the gap $[\underline{\mu}, \bar{\mu}]$ [34]. It is to be added that the computational burden for determining $\underline{\mu}$ is relatively low since it is generally based on the iterative process. In contrast, generating the optimal value of $\bar{\mu}$ tends to have high computational requirements, especially for large problems [40],[42].

The concept of the μ bounds is illustrated in Fig. 2.4. A lower bound $\underline{\mu}$ (which is also the upper bound of the robust stability margin) provides a sufficient condition of the instability of the system $(I - M\Delta)$ for the model perturbation $\Delta = 1/\underline{\mu}$ [34]. On the other hand, the upper bound $\bar{\mu}$ (which is also the lower bound of the robust stability margin) provides a sufficient condition that guarantees stability of the system $(I - M\Delta)$ for all perturbations that are smaller than $1/\bar{\mu}$ [34].

Although, $\underline{\mu}$ is not guaranteed to be equal to μ , it is always computed at the boundary of stability. Further, it yields the worse case perturbation model for a system. The destabilising values of the uncertainty matrices, corresponding to $\underline{\mu}$, can be obtained through computational algorithms. This is not the case with $\bar{\mu}$ upper bound. It is worth noting that much work has been devoted to increasing the accuracy of the bounds and reducing the gap between the bounds [33]. This includes the development of ad-hoc algorithms [34],[38],[40]. The worse ratio of $\mu/\bar{\mu}$ has been reported to be equal to 0.85 while in most cases the ratio is close to unity [35]. The lower bound $\underline{\mu}$ is therefore generally close to μ . For the aforementioned reasons, the lower bound $\underline{\mu}$ is used as a good estimate of μ in this study.

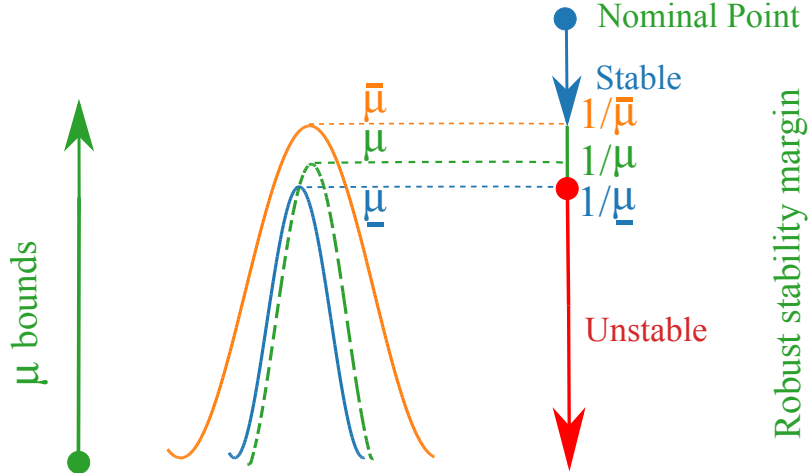


Figure 2.4: Representative figure to illustrate μ bounds and robust stability margin

2.4.3 Robust stability margin ($1/\mu$)

The robust stability margin is defined as $\min(\bar{\sigma}(\Delta(j\omega)))$ and is given by the inverse of μ in accordance with (2.13). It provides a measure of the smallest permissible deviation of uncertain elements from their nominal values, relative to their maximum uncertainty range. For the sake of illustration, a system with uncertainty in a single parameter P , as defined in (2.1), is considered. μ analysis identifies the smallest normalised perturbation $\delta_{P_{cr}}$ or the smallest critical parameter P_{cr} that causes instability, as depicted in (2.18). Equation (2.18) can be rearranged to give (2.19). The robust stability margin is given by $1/\mu$ or $|\delta_{P_{cr}}|$, as shown in (2.20). Fig. 2.5, which is an illustration of (2.19), clearly depicts the robust stability margin as being the ratio of the permissible uncertainty range for system stability, to the maximum uncertainty range; both being with respect to the nominal point. Further, robust stability margin can be interpreted as the magnitude by which the maximum uncertainty range must be scaled in order to guarantee stability [36]. In other words, the system is ensured stable within the range $(\pm P_{var} \times 1/\mu)$ or $(\pm P_{var} \times |\delta_{P_{cr}}|)$.

$$\text{At boundary of stability } P_{cr} = P_o + P_o P_{var} \delta_{P_{cr}} \quad (2.18)$$

$$\text{where } \delta_{P_{cr}} = \frac{P_{cr} - P_o}{P_o P_{var}} = \frac{(P_{cr} - P_o)}{(P_{max} - P_{min})/2} \quad (2.19)$$

$$\text{Robust stability margin } \bar{\sigma}(\Delta) = \frac{1}{\mu} = |\delta_{P_{cr}}| \quad (2.20)$$

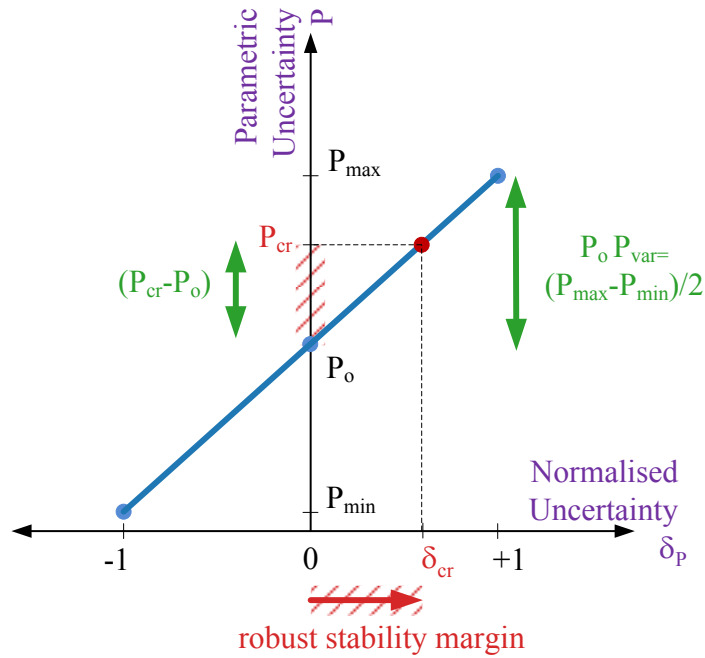
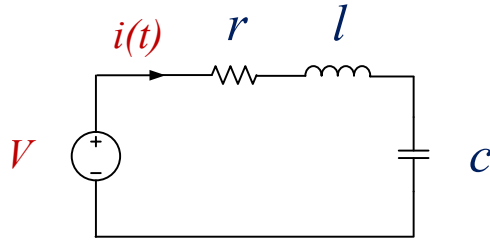


Figure 2.5: Robust stability margin for a system with a single parametric uncertainty

2.5 Applicative example

In this section, the modelling technique of LFT and the principle of SSV are illustrated by applying them to a basic *RLC* circuit, with possible uncertainties in its system parameters resistance r , inductor l and capacitor c . The system is shown in Fig. 2.6, where i and v denote the current in the circuit, and source voltage respectively.

Figure 2.6: *RLC* circuit

2.5.1 LFT modelling

There are several methods to represent uncertain system models in LFT forms. Two of these methods are analysed in the subsequent sections, by applying them to the *RLC* circuit shown in Fig.2.6. The first approach is based on interconnections of LFT models of system uncertain parameters and the second approach is based on Morton's method. The LFT modelling is generally performed by using developed software such as MATLAB[®] Robust stability toolbox and the ONERA[®] Skew mu toolbox [39],[42].

2.5.1.1 Interconnections of LFT models

This approach consists of first deriving LFT models for each uncertain parameter of the system and, then interconnecting them based on the dynamic system equation, in order to form an LFT model of the whole system. The modelling steps for converting the example *RLC* circuit, with uncertainties in its parameters r , l , c , are given below [49],[35].

- i. Identify system states and describe behaviour of the system by a set of differential equations, and state space matrix. The dynamic equation of the system in Fig. 2.6 is given by (2.21), where q denotes the charge of the capacitor. The corresponding state space matrix is given by (2.22), where $[q, i]$ denote the system states, v is the system input and i is the system output. The *RLC* system in (2.22) is equivalent to the original uncertain system depicted in Fig. 2.2a.

The subsequent steps describe how the RLC system with uncertainties in r , l and c , as given by (2.22), is converted in the LFT form.

$$l \frac{di}{dt} + r \frac{dq}{dt} + \frac{1}{c}q = v \quad (2.21)$$

$$\text{or } l \dot{i} + r \dot{q} + \frac{1}{c}q = v$$

$$\begin{bmatrix} \dot{q} \\ \dot{i} \\ y \end{bmatrix} = \left[\begin{array}{cc|c} 0 & 1 & 0 \\ -1/cl & -r/l & 1/l \\ 0 & 1 & 0 \end{array} \right] \begin{bmatrix} q \\ i \\ v \end{bmatrix} \quad (2.22)$$

- ii. Draw an equivalent block diagram of the system based on the system dynamic equations. The block diagram representing (2.21) is shown in Fig.2.7.

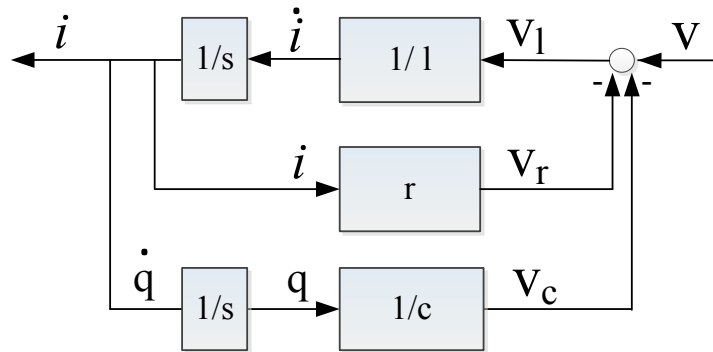


Figure 2.7: Basic block diagram of the example RLC circuit

- iii. Express each uncertain parameter of the system in its LFT form as explained in the examples in section 2.3. The LFT expressions for r , $1/l$ and $1/c$ are given in (2.23), (2.24) and (2.25) respectively.

$$r = r_o \pm r_o r_{var} \delta_r \quad (2.23)$$

$$1/l = 1/l_o - l_{var} \delta_l (1 + l_{var} \delta_l)^{-1} (1/l_o) \quad (2.24)$$

$$1/c = 1/c_o - c_{var} \delta_c (1 + c_{var} \delta_c)^{-1} (1/c_o) \quad (2.25)$$

- iv. Redraw the block diagram of the nominal system model by replacing each uncertain parameter by its corresponding LFT form. The uncertain *RLC* system under study is shown with uncertainties embedded in *r*, *l* and *c* in the block diagram in Fig. 2.8.

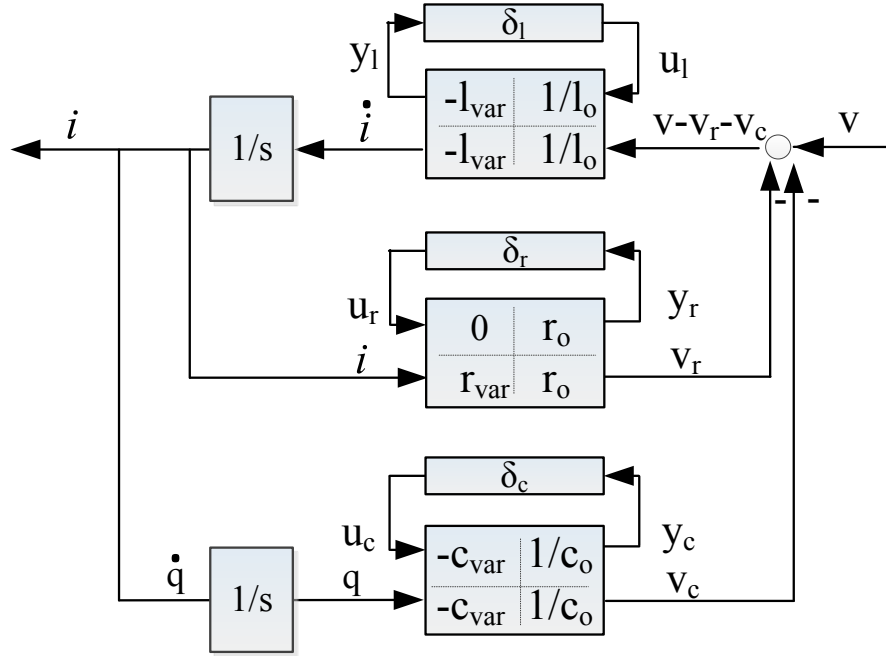


Figure 2.8: Block diagram of the example *RLC* circuit with uncertainties in *r*, *l*, *c*

- v. Derive a set of equations relating the output to the input of each uncertain parameter matrix and of each delta block based on the block diagram of the uncertain system. The set of equations describing the uncertain system in Fig. 2.8 are given by (2.26) - (2.34).

$$y_l = -l_{var}u_l + (v - v_r - v_c)/l_o \quad (2.26)$$

$$\dot{i} = -l_{var}u_l + (v - v_r - v_c)/l_o \quad (2.27)$$

$$y_r = r_o \dot{i} \quad (2.28)$$

$$v_r = r_{var}u_r + r_o \dot{i} \quad (2.29)$$

$$y_c = -c_{var}u_c + q/c_o \quad (2.30)$$

$$v_c = -c_{var}u_c + q/c_o \quad (2.31)$$

$$u_l = \delta_l y_l \quad (2.32)$$

$$u_r = \delta_r y_r \quad (2.33)$$

$$u_c = \delta_c y_c \quad (2.34)$$

vi. Construct the uncertain system matrix in the LFT form in (2.35) and (2.36), by rearranging equations (2.26) - (2.34). The matrices can be built by using the function “sysic” of MATLAB [42]. It is interesting to note that (2.35) - (2.36) are in the LFT form, as shown in Fig. 2.2b in subsection 2.3, with the parametric uncertainties “pulled out” from the system.

$$\begin{bmatrix} u_l \\ u_r \\ u_c \end{bmatrix} = \begin{bmatrix} \delta_l & 0 & 0 \\ 0 & \delta_r & 0 \\ 0 & 0 & \delta_c \end{bmatrix} \begin{bmatrix} y_l \\ y_r \\ y_c \end{bmatrix} \quad (2.35)$$

$$\begin{bmatrix} \dot{q} \\ \dot{i} \\ y_l \\ y_r \\ y_c \\ y \end{bmatrix} = \begin{bmatrix} 0 & 1 & 0 & 0 & 0 & 0 \\ -1/l_o c_o & -r_o/l_o & -l_{var} & -r_{var}/l_o & c_{var}/l_o & 1/l_o \\ -1/l_o c_o & -r_o/l_o & -l_{var} & -r_{var}/l_o & c_{var}/l_o & 1/l_o \\ 0 & r_o & 0 & 0 & 0 & 0 \\ 1/c_o & 0 & 0 & 0 & -c_{var} & 0 \\ 0 & 1 & 0 & 0 & 0 & 0 \end{bmatrix} \begin{bmatrix} q \\ i \\ u_l \\ u_r \\ u_c \\ v \end{bmatrix} \quad (2.36)$$

2.5.1.2 Morton's Method

Morton's method, which is another modelling technique to LFT, is described in this section. It is applied to the *RLC* circuit in Fig. 2.6, when the system is subject to uncertainties in r and c . The general steps of the method are outlined below [56].

First, the state space elements of an uncertain system (2.37), which is in the form shown in Fig. 2.2a, are separated into their nominal matrix and a series of uncertain matrices, each corresponding to one particular parametric uncertainty δ_i as represented in (2.38). By means of the Singular Value Decomposition (SVD) technique, each of the uncertain matrices is then decomposed into a set of their equivalent row and column matrices as shown in (2.39) - (2.41). These terms are then used to make up the final system matrix which is shown in (2.42). It can be noted that (2.42) is comparable to the elements of the general state space form in (2.43). This is the LFT form of the uncertain system, as shown in Fig. 2.2b.

$$S(\Delta) = \begin{bmatrix} A & B \\ C & D \end{bmatrix} \quad (2.37)$$

$$= \begin{bmatrix} A_0 & B_0 \\ C_0 & D_0 \end{bmatrix} + \sum_{i=1}^n \delta_i \begin{bmatrix} A_i & B_i \\ C_i & D_i \end{bmatrix} \quad (2.38)$$

Every term ($i : 1 - n$) is decomposed using SVD as follows:

$$\begin{bmatrix} A_i & B_i \\ C_i & D_i \end{bmatrix} = \begin{bmatrix} U_{i11} & U_{i12} \\ U_{i21} & U_{i22} \end{bmatrix} \begin{bmatrix} S_i & 0 \\ 0 & 0 \end{bmatrix} \begin{bmatrix} V_{i11} & V_{i12} \\ V_{i21} & V_{i22} \end{bmatrix} \quad (2.39)$$

The non-negligible singular values are retained in S_i leading to:

$$\begin{bmatrix} A_i & B_i \\ C_i & D_i \end{bmatrix} = \begin{bmatrix} U_{i1} \\ U_{i2} \end{bmatrix} \begin{bmatrix} V_{i1} & V_{i2} \end{bmatrix} \quad (2.40)$$

Therefore,

$$S(\Delta) = \begin{bmatrix} A_0 & B_0 \\ C_0 & D_0 \end{bmatrix} + \sum_{i=1}^n \delta_i \begin{bmatrix} U_{i1} \\ U_{i2} \end{bmatrix} \begin{bmatrix} V_{i1} & V_{i2} \end{bmatrix} \quad (2.41)$$

The final representation is:

$$S(\Delta) = \left[\begin{array}{c|ccc|c} A_0 & U_{11} & \cdot & \cdot & U_{n1} & B_0 \\ \hline V_{11} & 0 & \cdot & \cdot & 0 & V_{12} \\ \cdot & \cdot & & & \cdot & \cdot \\ \cdot & \cdot & & & \cdot & \cdot \\ \hline V_{n1} & 0 & \cdot & \cdot & 0 & V_{n2} \\ \hline C_0 & U_{12} & \cdot & \cdot & U_{n2} & D_0 \end{array} \right] \quad (2.42)$$

The general state space representation is:

$$\begin{bmatrix} \dot{x} \\ y_\Delta \\ y_s \end{bmatrix} = \left[\begin{array}{c|c|c} A_0 & B_1 & B_0 \\ \hline C_1 & D_{11} & D_{12} \\ \hline C_0 & D_{21} & D_0 \end{array} \right] \begin{bmatrix} x \\ u_\Delta \\ u_s \end{bmatrix} \quad (2.43)$$

Morton's method, which has been described in general terms earlier, is applied to the *RLC* circuit. The elements $1/l$ and $1/c$ are denoted respectively by m and k to simplify the notation. Only variations in r and c are considered in the following.

However if uncertainties in l are also taken into account this will lead to additional nonlinear uncertainties $\delta_k\delta_m$ and $\delta_r\delta_m$ and an additional mathematical effort is needed to represent the uncertain system model in form (2.42) as discussed in [36]. These non-linearities introduce additional terms in the D_{11} submatrix, as shown in (2.43), that is normally zero if the state-space model contains only linear uncertainties.

The steps to model the example *RLC* circuit in an LFT form using Morton's method are described below.

- i. Write down the state space representation of the *RLC* circuit as (2.47). This is comparable to the state space matrix as given in (2.22).
- ii. Replace the parameters in the state space matrix (2.47) by their uncertain models defined in (2.44) and (2.45) to obtain system uncertain matrix (2.48). It is to be noted that m_o is used for inverse of the nominal value of the inductance.

$$r = r_o + r_{var}r_o\delta_r \quad (2.44)$$

$$k = k_o + k_{var}k_o\delta_k \quad (2.45)$$

$$m = m_o \quad (2.46)$$

- iii. Identify uncertain sub-matrices relating to each uncertain parameter as in (2.49), and rewrite them in the form of product of their equivalent row and column matrices as in (2.50). In (2.50), the uncertain system is clearly seen with uncertainties embedded in r and k .
- iv. Replace the general sub-matrices in (2.42) with the corresponding elements in (2.50) to form the final system matrix (2.52) and the corresponding Δ matrix (2.51). The matrices (2.51) - (2.52) are now in the LFT form as shown in Fig 2.2b in subsection 2.3.

$$S(\Delta) = \left[\begin{array}{cc|c} 0 & 1 & 0 \\ -km & -rm & m \\ \hline 0 & 1 & 0 \end{array} \right] \quad (2.47)$$

$$= \left[\begin{array}{cc|c} 0 & 1 & 0 \\ (-k_o m_o - \delta_k p_k k_o m_o) & (-r_o m_o - \delta_r p_r r_o m_o) & m_o \\ \hline 0 & 1 & 0 \end{array} \right] \quad (2.48)$$

$$= \left[\begin{array}{cc|c} 0 & 1 & 0 \\ -k_o m_o & -r_o m_o & m_o \\ \hline 0 & 1 & 0 \end{array} \right] + \delta_k \left[\begin{array}{cc|c} 0 & 0 & 0 \\ -p_k k_o m_o & 0 & 0 \\ \hline 0 & 0 & 0 \end{array} \right] \\ + \delta_r \left[\begin{array}{cc|c} 0 & 0 & 0 \\ 0 & -p_r r_o m_o & 0 \\ \hline 0 & 0 & 0 \end{array} \right] \quad (2.49)$$

$$= \left[\begin{array}{cc|c} 0 & 1 & 0 \\ -k_o m_o & -r_o m_o & m_o \\ \hline 0 & 1 & 0 \end{array} \right] + \delta_k \left[\begin{array}{c} 0 \\ 1 \\ 0 \end{array} \right] \left[\begin{array}{cc|c} -p_k k_o m_o & 0 & 0 \end{array} \right] \\ + \delta_r \left[\begin{array}{c} 0 \\ 1 \\ 0 \end{array} \right] \left[\begin{array}{cc|c} 0 & -p_r r_o m_o & 0 \end{array} \right] \quad (2.50)$$

$$\begin{bmatrix} u_k \\ u_r \end{bmatrix} = \begin{bmatrix} \delta_k & 0 \\ 0 & \delta_r \end{bmatrix} \begin{bmatrix} y_k \\ y_r \end{bmatrix} \quad (2.51)$$

$$\begin{bmatrix} \dot{q} \\ \dot{i} \\ y_k \\ y_r \\ y \end{bmatrix} = \left[\begin{array}{cc|cc|c} 0 & 1 & 0 & 0 & 0 \\ -k_o m_o & -r_o m_o & 1 & 1 & m_o \\ \hline -k_{var} k_o m_o & 0 & 0 & 0 & 0 \\ 0 & -r_{var} r_o m_o & 0 & 0 & 0 \\ \hline 0 & 1 & 0 & 0 & 0 \end{array} \right] \begin{bmatrix} q \\ i \\ u_k \\ u_r \\ v \end{bmatrix} \quad (2.52)$$

2.5.2 μ analysis

In this section, the robust stability of the RLC circuit in Fig. 2.6 is assessed by using the μ approach. MATLAB[®] Robust stability toolbox is used to perform both the LFT operation and μ analysis [42]. It is expected that the RLC circuit will become resonant and reach borderline stability when the resistance r reaches zero. The nominal values, the range of parameter variations and the system transfer function or state space matrix are the only inputs required by the software, which first allows automatic conversion of the uncertain system models into the normalised $N\Delta$ structure before calculating lower and upper bounds of μ . Two cases are analysed in this section. In the first case, the uncertain RLC system has uncertainty in only one parameter namely r . In the second case, the system has uncertainties in all three parameters r , l and c .

2.5.2.1 Case Study I

In this case, the resistance r is considered to be the only uncertain parameter in the system, with an average nominal value of 6Ω and with possible variations between 0 and 12Ω as given in Table 2.1. The inductance and capacitance have fixed values, as depicted in Table 2.1.

Table 2.1: Uncertain parameter for Case I

Parameter	Nominal Value	Range of variation with respect to nominal value
Resistance r	$r_o : 6 \Omega$	$r_{var} : \pm 100 \%$
Inductance l	$l_o : 25 mH$	-
Capacitance c	$c_o : 100 \mu F$	-

Prior to μ analysis, the uncertain RLC system is converted to the $N\Delta$ form as described in section 2.3. For this case study, the resulting Δ matrix contains the unity norm bounded parameter δ_r as shown in (2.53).

$$\Delta(j2\pi f) = [\delta_r] \quad (2.53)$$

During μ analysis, the smallest disturbance that will cause the system pole to reach the imaginary axis, i.e. $\det(I - M\Delta(jw)) = 0$, is detected at each frequency w over a frequency grid defined between 50 Hz to 150 Hz . Fig. 2.9a and 2.9b show the plot of the μ bounds.

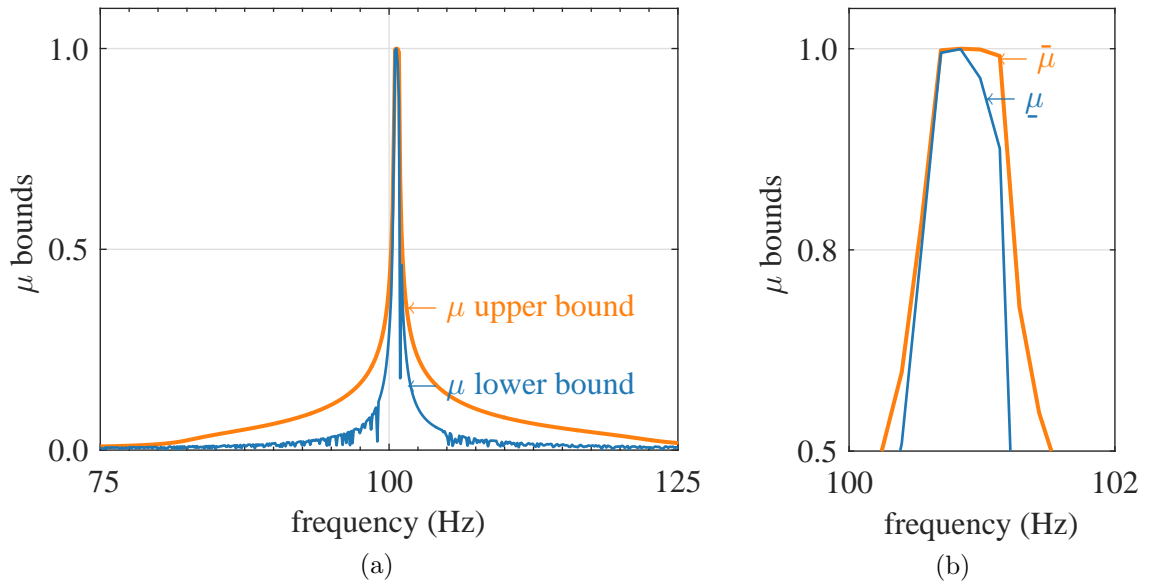


Figure 2.9: *RLC* system (a) μ chart to predict critical r (b) zoomed area near peak of μ chart

It is seen that the μ upper bound matches closely the μ lower bound for this case and the maximum SSV or μ is equal to 1 at the resonant frequency of 100.7 Hz . At this point the robust stability margin $\min(\bar{\sigma}(\Delta)) = 1/\mu = 1$. This is confirmed from the critical disturbance matrix given in (2.54), which is obtained from μ analysis.

$$\Delta(j2\pi 100.7) = [\delta_r] = [-1] \quad (2.54)$$

Hence, the smallest destabilising disturbance is $\delta_r = -1$ which corresponds to $r = 0$ Ω , in accordance with (2.44). At this point the *RLC* circuit becomes resonant as expected. μ is also a measure of robustness of the system stability. In this case $\mu = 1$ indicates that the system is at the robust stability margin. The system can withstand

all perturbations within the defined range of $r \pm 6\Omega$ without becoming unstable. For the case when $\delta_r = -1$ or $r = 0 \Omega$ the system will be at the boundary of stability.

2.5.2.2 Case Study II

In case II, all three parameters r , l and c are also allowed to vary within the intervals defined in Table 2.2. This causes the RLC circuit to become resonant over a range of frequency points as shown in Fig. 2.10a and 2.10b. This is correctly reflected in the μ bounds which remain at 1 over the resonant interval.

Table 2.2: Uncertain parameters for Case II

Uncertain Parameter	Nominal Value	Range of variation wrt nominal value
Resistance r	$r_o : 6 \Omega$	$r_{var} : \pm 100 \%$
Inductance l	$l_o : 25 mH$	$l_{var} : \pm 10 \%$
Capacitance c	$c_o : 100 \mu F$	$c_{var} : \pm 5 \%$

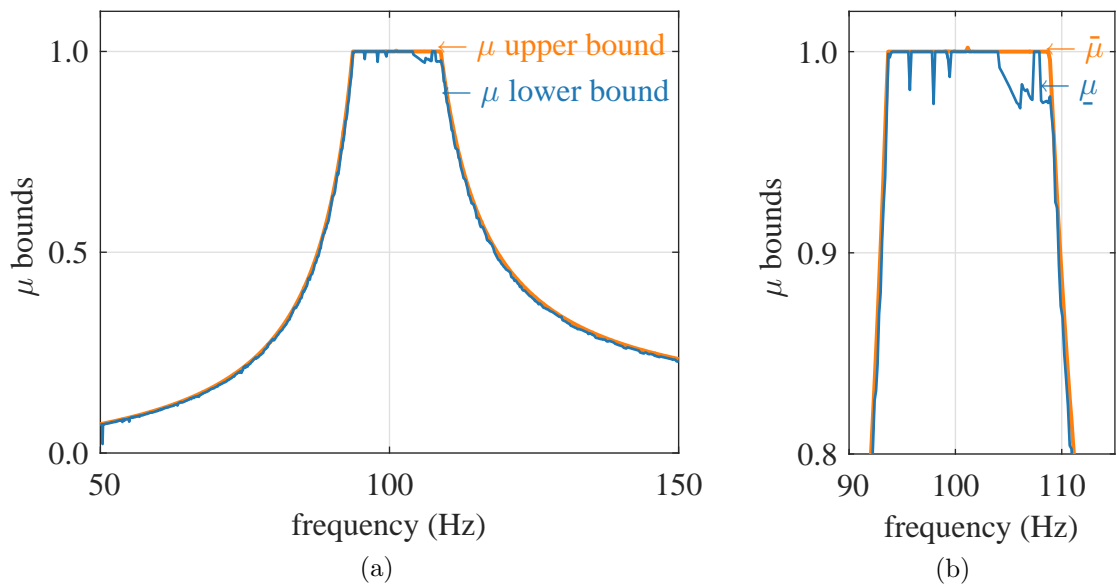


Figure 2.10: RLC system (a) μ chart to predict critical r , l , c (b) zoomed area near peak of μ chart

It is worth noting that when all three parameters vary, the uncertainty matrix is of the form (2.55).

$$\Delta(2\pi f) = \begin{bmatrix} \delta_c & 0 & 0 \\ 0 & \delta_l & 0 \\ 0 & 0 & \delta_r \end{bmatrix} \quad (2.55)$$

2.6 Limitations of the μ approach

2.6.1 Problem of convergence of the μ lower bound

In certain cases where all the uncertain parameters are purely real, it has been reported in the mathematical and engineering literature that the function μ lower bound can be discontinuous [36],[37],[38],[42]. The μ lower bound is computed at every frequency point within a grid of defined frequencies. If the lower bound μ falls between two frequency points, the analysis may fail to identify it. This thus leads to a problem of convergence in the computation of a μ lower bound. Increasing the density of the frequency grid may not always solve the problem. It is also probable that, due to the discontinuous nature of the problem, the analysis may identify a lower bound, which is not necessarily the closest to the actual μ . It has been found that one way to solve the convergence problem is to add a small complex value (α) to the real parameters, as described in appendix A. This approach can significantly improve continuity and convergence of the lower bound.

For the purpose of illustration, a parameter P , lying within the interval $[P_{min}, P_{max}]$, is considered. Parametric uncertainties are generally real in nature. A small complex value may be added to P , using the function *complexify* in MATLAB[®] Robust Control toolbox. The modified uncertain P now has a frequency response with a predominantly real value but with a small complex part added to it [38]. Instead of representing a certain interval of values, P is equivalent to a disc of complex

values centred around the nominal value [38]. This mixed μ problem, instead of a purely real μ problem, has better continuity properties, and hence better convergence behaviour [38]. It is to be added that the lower bound μ may be slightly more conservative, with the addition of the complex value. However, a certain function in the Toolbox allows extraction of the actual critical value of the parameter, while excluding the complex part. This is described in appendix A.

In the above two case studies pertaining to the *RLC* example circuit, the lower bound matched closely the upper bound indicating that μ is accurate. However, in case I where the uncertain parameter r is purely real, there was a problem of convergence in the computation of the μ bounds. This problem is illustrated Fig. 2.11. It can be seen from the μ chart in Fig. 2.11 that μ analysis failed to identify a critical uncertainty matrix at the resonant frequency of the system.

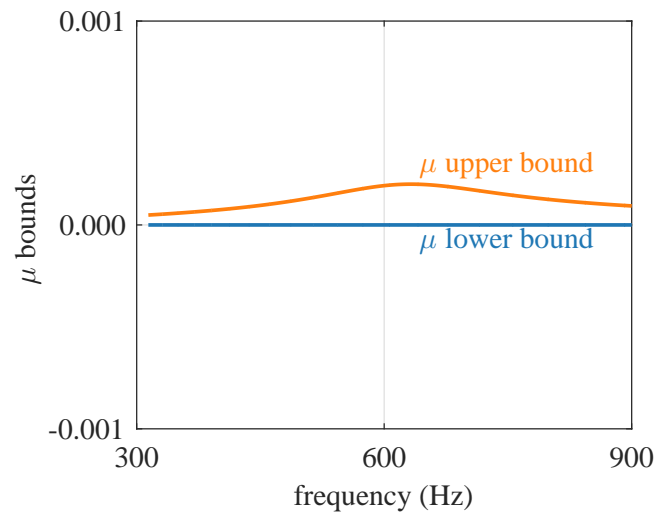


Figure 2.11: *RLC* system - μ bounds to predict critical r , with no added complexity

The problem has been solved by adding a small complex value (1%) to the real parameter r . The results have been reported in subsection 2.5.2.1. It is to be added that in case II, where all three parameters are uncertain, the μ chart, as shown in Fig. 2.10a, is continuous. The analysis has not required the addition of a complex value to the parameters. This indicates that the problem of convergence of the lower bound does not occur for all cases with real parameters. Further, the addition of

the complex value to the real parameter has proven to be an effective solution to the problem.

2.6.2 Size of the uncertainty matrix

In robust stability studies, it is desirable to keep the size of the uncertainty matrix as small as possible to reduce the computation burden. Hence it is important to note that the form of the system transfer function, when handled by the above mentioned software toolboxes, has a direct impact on the size of the resulting system and uncertainty matrices. More specifically the number of times one parameter appears in the transfer function description impacts the order of the final uncertain matrix. In the case of the *RLC* circuit, when the transfer function is written as $1/(ls^2 + rs + 1/c)$ the resulting uncertainty matrix is of the order 3x3. If the transfer function is written as $(1/l)/(s^2 + r/l s + 1/lc)$ the uncertainty matrix increases to the order of 5x5.

The uncertainty matrix in the example *RLC* circuit used to illustrate Morton's method was of the order of 2x2 as shown in (2.51). It is worth noting that if variations in the inductance are also included in the uncertain state-space model, the resulting uncertainty matrix is of the order 5x5 as shown in (2.56). This is due to the fact that the element m appears 3 times in the uncertain state-space matrix (2.47) and is treated, by Morton's method, as a new uncertain parameter each time it appears in the matrix. The system is thus regarded to have 5 uncertain elements. However there exist some order reduction methods that can be used to minimise the size of these matrices [3]. Further, optimising the transfer functions or state space matrices of a system may result in smaller uncertainty matrices and reduce computational burden [57].

$$\begin{bmatrix} \delta_k & 0 & 0 & 0 & 0 \\ 0 & \delta_{m1} & 0 & 0 & 0 \\ 0 & 0 & \delta_{m2} & 0 & 0 \\ 0 & 0 & 0 & \delta_{m3} & 0 \\ 0 & 0 & 0 & 0 & \delta_r \end{bmatrix} \quad (2.56)$$

2.7 Conclusion

This chapter has provided a comprehensive and clear explanation of the basic theoretical concepts underlying the μ approach, through illustrations and applications.

- The study has clearly demonstrated how the LFT technique “pulls out” uncertainties from an uncertain system model. Two well known modelling approaches to LFT, namely the interconnection of LFT models and Morton’s method, have been examined by applying them to the well established *RLC* system.
- The chapter has provided a clearer insight into the complex concept of μ . The state space matrix of a general system has been converted to its LFT or $N\Delta$ form. It has then been shown how the μ approach determines the stability of the whole system, by identifying the smallest perturbation matrix Δ that destabilises the feedback loop $M\Delta$, where M is a subsystem of N . The concept of μ has been illustrated by applying it to the *RLC* example system.
- This study has clearly demonstrated the meaning and limitations of the μ bounds, through illustrations, and application to the *RLC* example system. The lower and upper bounds, being the estimates of the actual value of μ , are generally not clearly described in the literature. Justification has been provided as to the use for the μ lower bound in this work.
- Through clear illustrations, it has been shown how the robust stability margin ($1/\mu$) determines by how much the maximum uncertainty range must be scaled in order to guarantee robust stability of an uncertain system.

- Computational limitations of the μ bounds have been discussed, and possible solutions have been presented.

Through the thorough and clear examination of the key concepts of the μ theorem, this chapter has provided a first stepping stone for making the μ approach more applicable.

Chapter 3

μ approach to robust stability domains

3.1 Introduction

As discussed earlier in this work, power electronic systems are the foundation of the electrification of land, air and sea vehicles [4]. Unfortunately, power electronic controlled loads, due to their common constant power load behaviour, are seen in the network as negative impedances and thus can cause severe stability issues within the power system [12],[14]. Moreover, in practice, these EPS are subject to multiple simultaneous parameter uncertainties, such as variations in system load, source impedance or operating temperature. These uncertainties may further compromise system stability, as will be demonstrated in later chapters. It naturally follows that the stability domains within which such systems may operate safely in the face of multiple uncertainties need to be identified, as an aid to designing stable systems especially for safety critical applications. The μ approach, presented in this work, can prove to be an effective analysis tool in determining the robust stability domains for electrical power systems with multiple parametric uncertainties [34].

In order to effectively apply the μ method to obtain a robust stability measure for the aforementioned EPS, the significance of the single-valued μ in the analysis of multiple parameter uncertainties need to be understood. This subject does not seem to have been adequately treated in the literature, which does not alleviate the complexity of the μ framework [33]. Nevertheless, the authors in [34] have discussed the concept of the hypercube in order to explain μ for systems with multiple uncertainties. The hypercube has been treated at a purely conceptual level in [34]. Yet, the study has provided an opportunity to further explore and apply the hypercube concept, in view of bringing deeper understanding of μ in the space of multiple parametric uncertainties. Moreover, μ results generated in the frequency domain may not be easily understood. Translating the μ results from the frequency domain to the more perceivable parametric domain may help bring more clarity to the robust stability measure μ .

While the meaning of μ with respect to a single parameter variation has been examined to some extent in the earlier chapter, this study aims to provide new insights into the meaning and usefulness of μ , with respect to multiple parametric uncertainties. In light of the aforementioned discussion, the concept of the hypercube is to be explored and extended by applying it to a basic electrical power system connected to an ideal constant power load. The ideal CPL is an important representation of tightly controlled power electronic driven loads, as was reviewed in the introduction part of this work. It is widely used in the stability studies of PE systems [16]. It is to be noted that a few figures used in Chapter 1 are reproduced in this study for convenience.

The objective of this chapter is to show how μ can provide information on the stability domains within which a system with multiple uncertainties can be guaranteed stable, while shedding light on μ theory in parametric space. The predictions from μ analysis are to be evaluated and verified against analytical results.

3.2 Modelling of an EPS with an ideal CPL

The electrical network of the MET may consist of a multitude of loads interfaced through power converters. Such a power converter may behave as constant power load under fast controller actions [7],[12]. These types of power electronic driven loads can mathematically be represented as ideal CPLs. An example of a CPL is the DC/DC buck converter. With converter efficiency considered as constant, the input power drawn from the source is also constant.

3.2.1 Non-linear model of the ideal CPL

Fig. 3.1 depicts the example EPS that is used to support this study. It is an ideal CPL connected to the dc power supply through an input LC filter. The system parameters are defined in Table 3.1. The power electronic controlled load displays constant power load characteristic, which is depicted in the non-linear equation (3.1) and in Fig. 3.2.

$$i_{in}(t) = \frac{P_{in}}{v_{in}(t)} \quad (3.1)$$

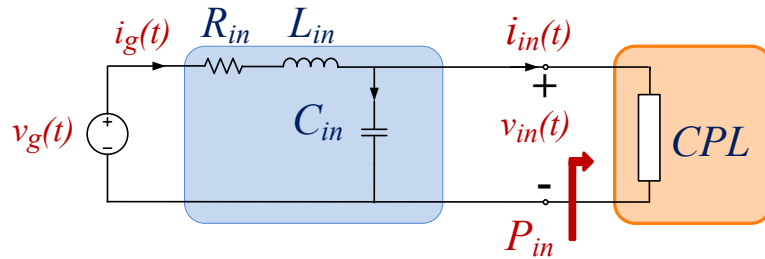


Figure 3.1: Non-linear model of the ideal CPL

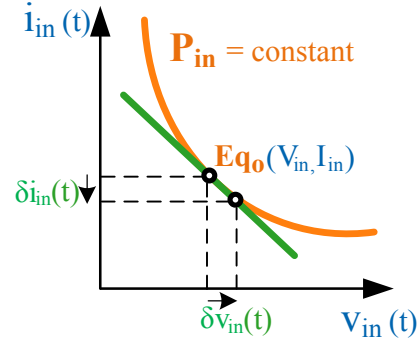


Figure 3.2: Characteristic curve of the ideal CPL

Table 3.1: Nominal values for system parameters

Symbol	Units	Nominal Values	Description
v_g	V	19.8	DC source voltage
R_{in}	$m\Omega$	160	Input Resistance
L_{in}	μH	511.8	Input filter inductance
C_{in}	μF	95	Input filter capacitance
P_{in}	W	10.4	Input power

3.2.2 Small-signal ac model of the ideal CPL

Most control design and stability analysis methods work on linear systems. Hence, it is important to study the linear model of the CPL. At any given operating point, the system currents and voltages may be represented by dc values with some superimposed small-signal ac components as shown in (3.2).

$$i_{in}(t) = I_{in} + \hat{i}_{in}(t), \quad v_{in}(t) = V_{in} + \hat{v}_{in}(t) \quad (3.2)$$

In view of linearising the CPL at the dc quiescent point (V_{in}, I_{in}) denoted as Eq_o in Fig. 3.2, the gradient at that point is obtained from the partial derivative of

(3.1), as shown in (3.3) - (3.4). This gradient represents the small-signal incremental impedance at the dc point, as also depicted in (3.5).

$$\delta i_{in}(t) = -\frac{P_{in}}{V_{in}^2} \delta v_{in}(t) + \frac{1}{V_{in}} \delta P_{in}(t) \quad (3.3)$$

$$\frac{\delta i_{in}(t)}{\delta v_{in}(t)} = -\frac{P_{in}}{V_{in}^2}, \quad \text{since } \delta P_{in}(t) = 0 \quad (3.4)$$

$$\frac{\delta i_{in}(t)}{\delta v_{in}(t)} = \frac{i_{in}(t) - I_{in}}{v_{in}(t) - V_{in}} = \frac{\hat{i}_{in}(t)}{\hat{v}_{in}(t)} = -\frac{P_{in}}{V_{in}^2} = \frac{1}{(-R_{cpl})} \quad (3.5)$$

It is worth noting that while the steady state impedance V_{in}/I_{in} is positive, the small-signal incremental impedance, as given by (3.5) and shown in Fig. 3.2, is negative. It is the negative impedance characteristics of the CPLs that account for their propensity to become unstable [16]. Based on this analysis, the small-signal model of the CPL system can be represented in Fig. 3.3.

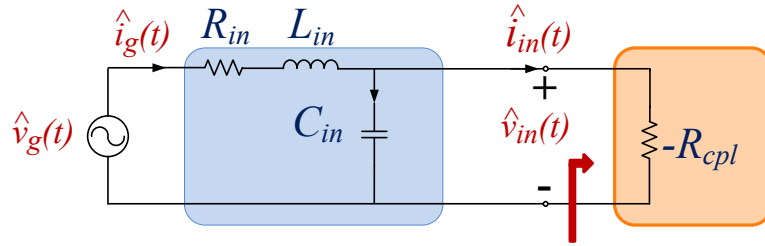


Figure 3.3: Small-signal model of the ideal CPL

3.2.3 Linear model of the ideal CPL

Furthermore, by using tangent line approximation of the non-linear equation (3.1) together with the small-signal incremental impedance (3.5), the linear model of the CPL can be obtained as (3.8). The steps are shown in (3.6) - (3.8).

$$\frac{i_{in}(t) - I_{in}}{v_{in}(t) - V_{in}} = -\frac{P_{in}}{V_{in}^2} \quad (3.6)$$

$$i_{in}(t) = -\frac{P_{in}}{V_{in}^2} v_{in}(t) + \frac{P_{in}}{V_{in}} + I_{in} \quad (3.7)$$

$$i_{in}(t) = \frac{1}{(-R_{cpl})} v_{in}(t) + I_{cpl} \quad (3.8)$$

$$\text{where } -R_{cpl} = -\frac{V_{in}^2}{P_{in}}, \quad I_{cpl} = \frac{2P_{in}}{V_{in}} = 2I_{in}$$

Based on the function (3.8), the circuit diagram of the linear model of the ideal CPL can be constructed by connecting a negative resistance $-R_{cpl}$ in parallel with a constant current source I_{cpl} as shown in Fig. 3.4.

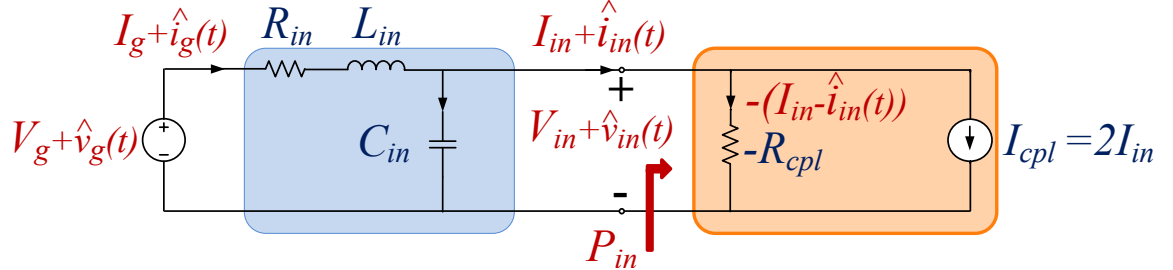


Figure 3.4: Linear model of the ideal CPL

The expression (3.8) can be rearranged and represented as (3.9), which is interesting in that it clearly shows the voltage across the negative resistance and the current that flows through it, as illustrated in Fig. 3.4. In accordance with Kirchoff's current law, the current flowing to the current source is $2I_{in}$. Additionally, since the current source carries only dc current, the small-signal ac current $\hat{i}_{in}(t)$ only flows through the negative resistance.

$$-R_{cpl} = \frac{V_{in} + \hat{v}_{in}(t)}{-(I_{in} - \hat{i}_{in}(t))} \quad (3.9)$$

3.2.4 The EPS with the ideal CPL

This chapter applies μ analysis to the EPS connected to the ideal CPL, as shown in Fig. 3.1, over a range of operating points and parameter variations. Hence, a modelling methodology is employed to represent the non-linear EPS as an equivalent linear model that contains all system variations, in addition to being suitable for μ analysis [58]. The method is based on symbolic linearisation around an arbitrary equilibrium point, as described below. Of note is that the methodology will be covered in greater depth in Chapter 5, by applying it to the PM machine drive system.

The first step involves writing the differential equations which describe the dynamic behaviour of the non-linear system in Fig. 3.1. These are given as (3.10) - (3.11).

$$\frac{di_g(t)}{dt} = -\frac{R_{in}}{L_{in}}i_g(t) - \frac{1}{L_{in}}v_{in}(t) + \frac{1}{L_{in}}v_g(t) \quad (3.10)$$

$$\frac{dv_{in}(t)}{dt} = \frac{1}{C_{in}}i_g(t) - \frac{P_{in}}{C_{in}}\frac{1}{v_{in}(t)} \quad (3.11)$$

The next step is to linearise the non-linear system model in symbolic form. The equations (3.10) - (3.11) are firstly represented in the state space form (3.12) with the states $x(t)=[i_g(t), v_{in}(t)]$, input $u(t)=v_g(t)$ and output $y(t)=v_{in}(t)$. For the purpose of linearisation, the system variables are expanded in terms of their dc and ac components as shown in (3.12). Linearisation is then performed based on (3.13) where the dc quiescent point and the small-signal ac model are extracted as (3.14) and (3.15) respectively.

$$\dot{x}(t) = f(x, u), \text{ where } x(t) = X + \hat{x}(t), \quad u(t) = U + \hat{u}(t) \quad (3.12)$$

$$\dot{X} + \hat{\dot{x}}(t) \cong f(X, U) + \left[\frac{\delta f}{\delta x} \right]_{X,U} \hat{x}(t) + \left[\frac{\delta f}{\delta u} \right]_{X,U} \hat{u}(t) \quad (3.13)$$

$$0 = f(X, U) \quad \text{dc terms} \quad (3.14)$$

$$\begin{aligned} \hat{x}(t) &= \left[\frac{\delta f}{\delta x} \right]_{X,U} \hat{x}(t) + \left[\frac{\delta f}{\delta u} \right]_{X,U} \hat{u}(t) \\ &= A\hat{x}(t) + B\hat{u}(t) \quad \text{ac terms} \end{aligned} \quad (3.15)$$

Based on (3.14) and $U = V_g$, the dc equilibrium states $X = [I_g, V_{in}]$ can be computed by equating (3.10) - (3.11) to zero and are given as (3.16) and (3.17) respectively.

$$I_g = I_n = \frac{P_{in}}{V_{in}} \quad (3.16)$$

$$V_{in} = \frac{V_g}{2} \left[1 + \sqrt{1 - 4R_{in} \frac{P_{in}}{V_g^2}} \right] \quad (3.17)$$

It is to be noted that all the elements in the system model should be in their rational form in order to allow conversion of the system model in its corresponding LFT configuration [41]. Hence the voltage V_{in} in (3.17) is expressed in its rational form V_{in-est} as shown in (3.18) by employing the first order approximation of the binomial series expansion.

$$V_{in-est} = V_g - \frac{R_{in}P_{in}}{V_g} \quad (3.18)$$

Based on the general equation (3.15), the small-signal ac model of the considered system can be obtained as (3.19). Besides, the small-signal output can be written as (3.20) from $\hat{y}(t) = \hat{v}_{in}(t)$.

$$\begin{bmatrix} \frac{d\hat{i}_g(t)}{dt} \\ \frac{d\hat{v}_{in}(t)}{dt} \end{bmatrix} = \begin{bmatrix} -\frac{R_{in}}{L_{in}} & -\frac{1}{L_{in}} \\ \frac{1}{C_{in}} & \frac{P_{in}}{C_{in}V_{in-est}^2} \end{bmatrix} \begin{bmatrix} \hat{i}_g(t) \\ \hat{v}_{in}(t) \end{bmatrix} + \begin{bmatrix} \frac{1}{L_{in}} \\ 0 \end{bmatrix} \hat{v}_g(t) \quad (3.19)$$

$$\hat{y}(t) = \begin{bmatrix} 0 & 1 \end{bmatrix} \begin{bmatrix} \hat{i}_g(t) \\ \hat{v}_{in}(t) \end{bmatrix} \quad (3.20)$$

The developed small-signal model, (3.19) - (3.20), operating about the dc equilibrium point (3.16) - (3.17), represents the non-linear system shown in Fig. 3.1 over a range of operating points and parameter variations, in addition of being suitable for μ analysis [58]. It is referred to as the *equivalent linear model* of the power system in Fig. 3.1.

μ analysis is applied to the equivalent linear model (3.19) - (3.20) to evaluate the stability robustness and stability domains of the power system in Fig. 3.1, in the remaining part of the chapter. The μ predictions are verified against results obtained analytically. To that end, the stability boundary conditions based on the characteristic equations of the power system under study are developed in the next section.

3.3 Analytical assessment of system stability

The transfer function of the small-signal model of the power system, as shown in Fig. 3.3, is given by (3.21) [59].

$$\frac{\hat{v}_{in}(t)}{\hat{v}_g(t)} = \frac{1}{[C_{in}L_{in}s^2 + (C_{in}R_{in} - \frac{L_{in}P_{in}}{V_{in-est}^2})s + (1 - \frac{R_{in}P_{in}}{V_{in-est}^2})]} \quad (3.21)$$

The stability of the system can be examined by verifying the location of the roots of its characteristic equation, as given by (3.22) [59].

$$C_{in}L_{in}s^2 + (C_{in}R_{in} - \frac{L_{in}P_{in}}{V_{in-est}^2})s + (1 - \frac{R_{in}P_{in}}{V_{in-est}^2}) = 0 \quad (3.22)$$

Based on Routh-Hurwitz criterion, the terms in the characteristic equation as given by (3.23) and (3.24) must be positive for the system to be stable [59].

$$C_{in}R_{in} - \frac{L_{in}P_{in}}{V_{in-est}^2} > 0 \quad (3.23)$$

$$1 - \frac{R_{in}P_{in}}{V_{in-est}^2} > 0 \quad (3.24)$$

However, since the input resistance R_{in} has a relatively low value, condition (3.24) can be neglected and the main condition for system stability becomes (3.23). Hence at boundary stability, the critical power P_{in} is obtained as (3.25) from the main condition (3.23).

$$\text{At boundary stability } P_{in} = \frac{C_{in}R_{in}V_{in-est}^2}{L_{in}} \quad (3.25)$$

Replacing V_{in-est} in (3.25) by (3.18) produces the expression (3.26) from which the critical value of P_{in} can be computed analytically.

$$\frac{R_{in}^2}{V_g^2}P_{in}^2 - (\frac{L_{in}}{C_{in}R_{in}} + 2R_{in})P_{in} + V_g^2 = 0 \quad (3.26)$$

Further, at the boundary condition of stability, the critical frequency of oscillation is given as (3.27). The expression is derived by substituting (3.25) in the system characteristic equation in (3.22) and solving for s or jw . The critical conditions (3.26) and (3.27) are used to verify the results from μ analysis.

$$\text{At boundary stability } s = jw = j2\pi f = \sqrt{\left(\frac{L_{in} - C_{in}R_{in}^2}{C_{in}L_{in}^2}\right)} \quad (3.27)$$

3.4 System with single parametric uncertainty

This section demonstrates how μ analysis is employed to determine stability robustness and stability domains of the power system in Fig. 3.1, when it is subject to variation in a single parameter. The nominal values of the system parameters are given in Table 3.1. Considering that the input power P_{in} may vary within $\pm 33\%$ of its nominal value of 10.4 W , as defined in Table 3.2, μ analysis is applied to the equivalent linear model of the power system, as given by (3.19) - (3.20), to determine the critical or smallest input power that can destabilise the system.

Table 3.2: Single uncertain parameter system (case I) - the uncertain parameter

Parameters	Nominal Value	Range of Variation
P_{in}	$P_{ino} = 10.4\text{ W}$	$P_{invar} = \pm 33\%$

3.4.1 μ analysis

The application of μ analysis requires that the considered equivalent linear model be first converted in the $M\Delta$ or LFT form. This can be performed by using MATLAB[®] Robust Stability Toolbox. The only inputs that are required by the software are firstly the state space model, which is (3.19) - (3.20) in our case, and then the values of the fixed and uncertain parameters which are defined in Tables 3.1 and 3.2 respectively for the case under study.

The operation of LFT entails expressing all uncertain parameters in the system model as LFTs. Thus, the parameter P_{in} in the system model is written in its normalised form $\delta_{P_{in}}$ in (3.28), based on equation (2.1) and the information in Table 3.2.

$$P_{in} = P_{ino} + P_{ino}P_{invar}\delta_{P_{in}} \quad (3.28)$$

The normalised parameters $\delta_{P_{in}}$ are then extracted from the system model (3.19)-(3.20) and grouped in a diagonal matrix in a feedback form by employing the LFT technique. This results in the system model being converted in its $M\Delta$ form with the disturbance matrix given by (3.29), where I_3 is a 3×3 identity matrix; $\delta_{P_{in}}$ appears 3 times in the uncertainty matrix since P_{in} appears that number of times in the uncertain system model.

$$\Delta(j2\pi f) = \text{diag}(\delta_{P_{in}} I_3) \quad (3.29)$$

The system stability can now be examined by applying μ analysis to the system model in its LFT form. Based on the principle of SSV, which was described in chapter 2, μ analysis identifies the smallest uncertainty matrix that destabilises the system. The results are depicted in Fig. 3.5a and 3.5b.

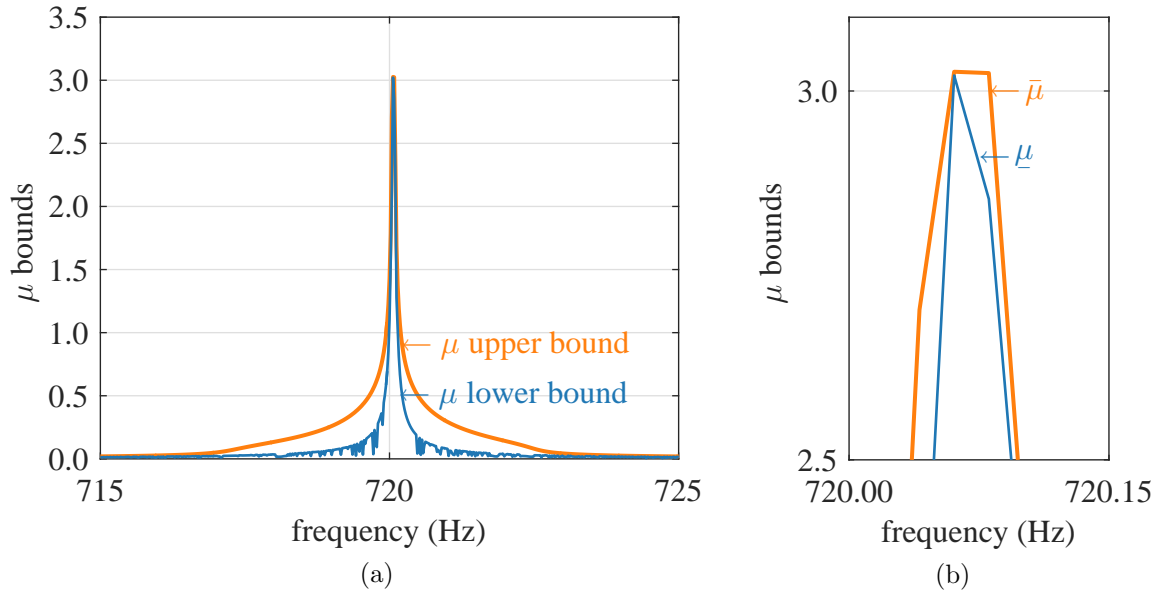


Figure 3.5: Single uncertain parameter system (a) μ chart to determine critical P_{in} (b) zoomed area near peak of μ chart

From the μ charts, it can be seen that the peak values of both the lower bound $\underline{\mu}$ and the upper bound $\bar{\mu}$ are equal to 3.02. The μ bounds occur at the critical frequency of 720.1 Hz, which corresponds to the resonant frequency of the LC filter, estimated as $1/2\pi\sqrt{L_{in}C_{in}}$. By using appropriate function in MATLAB[®] Robust Stability Toolbox, the smallest destabilising disturbance matrix is extracted as $\Delta(j2\pi720.1)$ as shown in (3.30) and in Table 3.3 [42].

$$\Delta(j2\pi720.1) = \text{diag}(+0.331 I_3) \quad (3.30)$$

The critical value of δ_{Pin} is equal to 0.331 as can be deduced by comparing $\Delta(j2\pi720.1)$ in (3.30) with the structure of the uncertainty matrix in (3.29). The robust stability margin can be calculated as $1/\underline{\mu} = 0.331$. The smallest input power that can destabilise the power system is computed as 11.53 W, as shown in equation (3.31) and given in Table 3.3.

$$P_{in} = P_{ino} + P_{ino}P_{invar}\delta_{Pin} = 10.4 + 10.4 \times 0.33 \times 0.331 = 11.53 W \quad (3.31)$$

Table 3.3: Single uncertain parameter system - μ analysis results

Perturbation matrix	$\bar{\sigma}(\Delta(jw))$	$\underline{\mu} = 1/\bar{\sigma}(\Delta(jw))$	Critical P_{in}
$\Delta(j2\pi720)$	0.331	3.02	11.53 W

3.4.2 Analytical verification

Further, the critical power and frequency have been calculated according to the analytical stability conditions (3.26) and (3.27) respectively. The analytical results agree exactly with the μ analysis results as shown in Table 3.4. This finding supports the results from μ analysis.

Table 3.4: Single uncertain parameter system - μ analysis and analytical results

	μ analysis results	Analytical results
Critical input power (P_{in})	11.53 W	11.53 W
Critical frequency (f)	720 Hz	720 Hz

In addition, the eigenvalues are first computed under nominal conditions, and then from the critical input power provided by the μ lower bound, as given in Table 3.4. From the eigenvalue plot in Fig. 3.6, it is seen that the application of the destabilising uncertainty matrix to the nominal model causes both system poles to move to the imaginary axis. This further validates the results from μ analysis.

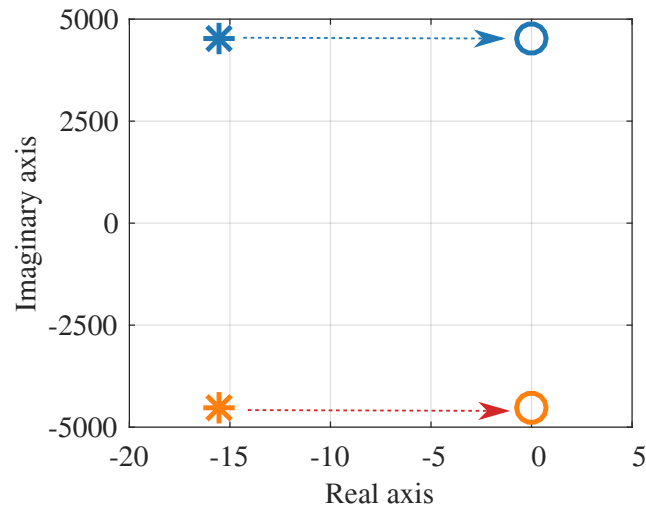


Figure 3.6: Single uncertain parameter system - Plot of eigenvalues based μ lower bound predictions, (*) eigenvalues with nominal $P_{in} = 10.4 W$, (o) eigenvalues with critical $P_{in} = 11.53 W$

3.4.3 Robust stability domains

The μ tool identifies the smallest destabilising perturbation matrix as given by (3.30). From the critical uncertainty matrix, the robust stability margin $|\delta_{P_{in}}|$ or $1/\underline{\mu}$ is 0.331, as shown in Table 3.3. This implies that for any value of $|\delta_{P_{in}}| < 0.331$, the system is guaranteed stable; in contrast for any value of $\delta_{P_{in}} > +0.331$, the system is unstable, as depicted in Fig. 3.7.

In parametric space, for an EPS with a single parametric uncertainty, μ analysis provides the largest normalised line segment of coordinate size $1/\underline{\mu}$ with respect to the nominal point, within which the system is guaranteed robustly stable. This line segment is represented in Fig. 3.7 for the case study.

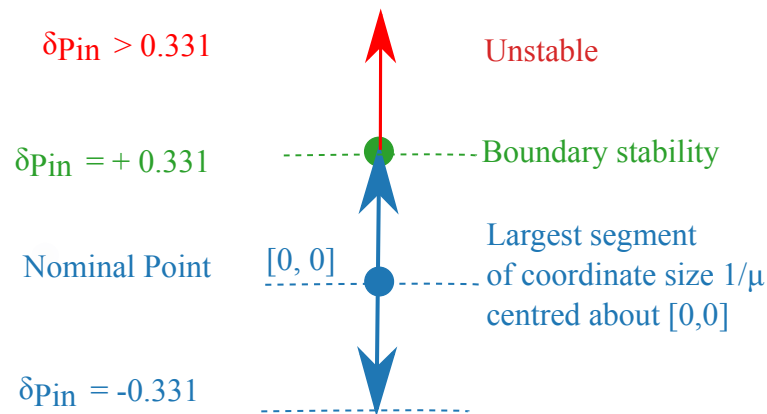


Figure 3.7: Single uncertain parameter system - Largest linear segment of coordinate size $(1/\underline{\mu})$ centred about nominal point within which system is robustly stable

Based on the explanation of robust stability margin provided in section 2.4.3 in chapter 2, it is interesting to add that, in order to guarantee robust stability, the maximum variation in P_{in} , which is 33% as defined in Table 3.2, must be scaled by $(1/\underline{\mu} = 0.331)$. In other words, robust stability is ensured if P_{in} is allowed to vary only within $0.331 \times 33\% = 11\%$ of its nominal value of $10.4 W$, i.e. within $[9.53 W, 11.53 W]$. This supports the findings provided by the hypercube, and the results obtained from the eigenvalue method, as shown in Fig. 3.7 and Fig 3.6 respectively.

3.5 System with two parametric uncertainties

In this case study, the power system in Fig. 3.1 is subject to variation in two parameters namely C_{in} and P_{in} , as depicted in Table 3.5. The other parameters are fixed as defined in Table 3.1. This subsection examines both the stability robustness and the stability domain of the system.

Table 3.5: Two uncertain parameters system (case II) - the uncertain parameters

Parameters	Nominal Value	Range of Variation
P_{in}	$P_{ino} = 10.4 W$	$P_{invar} = \pm 33 \%$
C_{in}	$C_{ino} = 95 \mu F$	$C_{invar} = \pm 10 \%$

3.5.1 μ analysis

μ analysis is performed on the equivalent linear model (3.19) - (3.20) based on the nominal values and the range of variation of the two uncertain parameters, as defined in Table 3.5. The structure of the uncertainty matrix is obtained as (3.32) from the LFT operation.

$$\Delta(j2\pi f) = \text{diag}(\delta_{C_{in}} I_2, \delta_{P_{in}} I_3) \quad (3.32)$$

The resulting μ chart is depicted in Fig. 3.8a and 3.8b, from which it can be noted that $\mu = \underline{\mu} = \bar{\mu} = 4.03$. The results are given in Table 3.6.

Table 3.6: Two uncertain parameters system - μ analysis results

Critical $\Delta(jw)$	$\bar{\sigma}(\Delta(jw))=1/\underline{\mu}$	$\underline{\mu}$
$\Delta(j2\pi 729.2)$	0.248	4.03

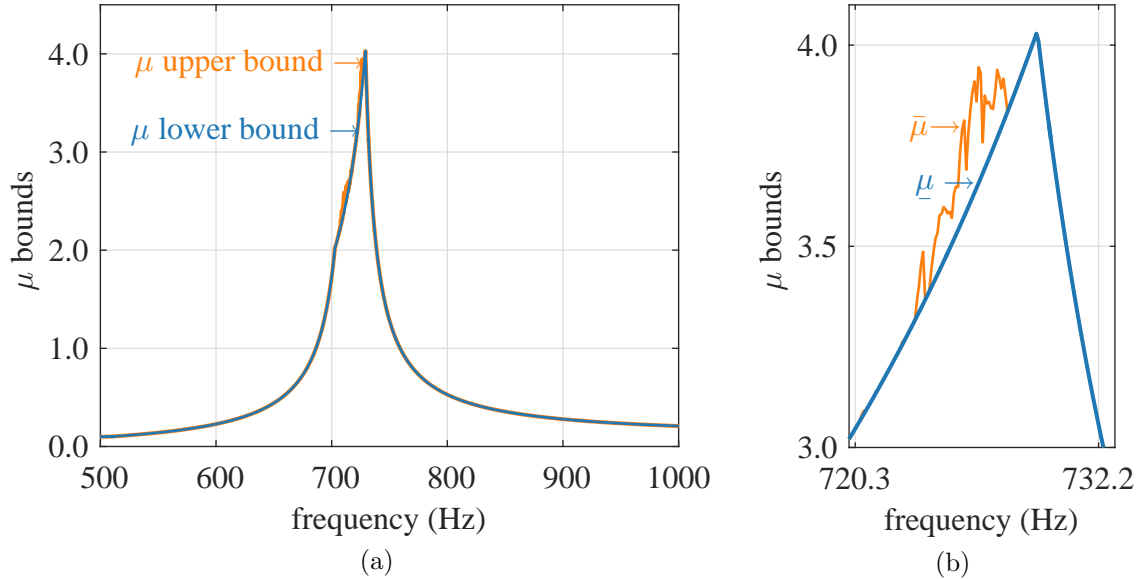


Figure 3.8: Two uncertain parameters system (a) μ chart to determine critical C_{in} and P_{in} (b) zoomed area near peak of μ chart

The smallest perturbation matrix, which is provided by the μ lower bound at the critical frequency of 729.2 Hz , is given in (3.33).

$$\Delta(j2\pi 729.2) = \text{diag}(-0.248 I_2, +0.248 I_3) \quad (3.33)$$

By comparing the perturbation matrix (3.33) with the structure of the uncertainty matrix (3.32), the critical values of $\delta_{C_{in}}$ and $\delta_{P_{in}}$ can be derived, as shown in Table 3.7. Based on these critical values, the smallest destabilising input capacitance and input power are computed as $92.65 \mu\text{F}$ and 11.25 W respectively, from the (3.28), as shown in Table 3.7.

It is to be noted that the critical frequency has increased from 720 Hz , for the single uncertain parameter system analysed in the earlier section, to 729.2 Hz for the current case study. This is due to the fact that the system reaches boundary stability at a lower critical capacitance of $92.65 \mu\text{F}$ for case II, as compared to $95 \mu\text{F}$ for case I.

Table 3.7: Two uncertain parameters system - Critical values of C_{in} , P_{in} from μ analysis

Critical $\Delta(jw)$	$\delta_{C_{in}}$	$\delta_{P_{in}}$	C_{in} (μF)	P_{in} (W)
$\Delta(j2\pi 729.2)$	-0.248	+0.248	92.65	11.25

3.5.2 Analytical verification

For verifying the μ results, the input power and frequency are computed from the analytical stability boundary conditions (3.26) and (3.27) respectively, with C_{in} set to its critical value of 92.65 μF . The analytically obtained results are found to match exactly the μ analysis results as shown in Table 3.8.

Table 3.8: Two uncertain parameters system - μ analysis and analytical results

	μ analysis results	Analytical results
Critical input power (P_{in})	11.25 W	11.25 W
Critical frequency (f)	729.2 Hz	729.2 Hz

3.5.3 Stability domains

This section demonstrates how μ analysis can be used to determine stability domains of the power system under study. As discussed earlier, the peak value of the μ lower bound corresponds to a perturbation matrix at the critical frequency of 729.2 Hz. Similarly, each point along the μ chart corresponds to a particular perturbation matrix at a specific frequency. These perturbation matrices can be extracted from the μ chart and employed to construct stability domains of the power system [42].

For this case study, perturbation matrices are extracted at a number of frequency points on the μ lower bound chart as shown in Fig. 3.9. For the purpose of illustration, three uncertainty matrices corresponding to points A , B and C in Fig. 3.9, and given by (3.34), (3.35) and (3.36) respectively, are analysed. The corresponding μ values are given in Table 3.9.

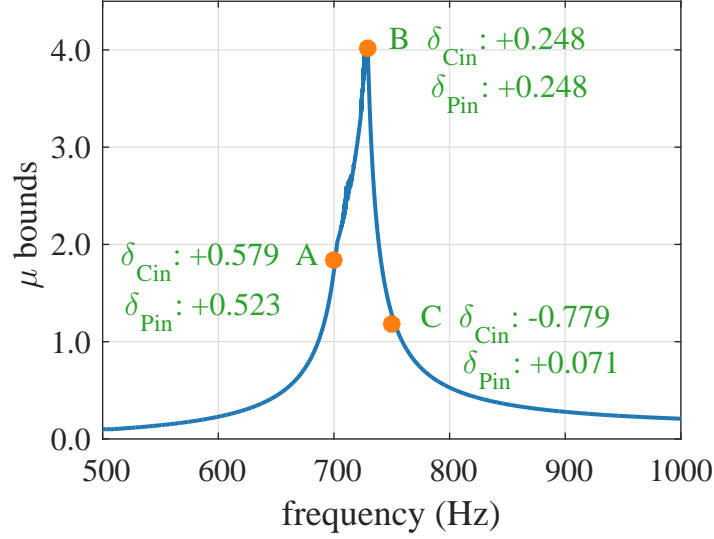


Figure 3.9: Two uncertain parameters system - Points A, B, C chosen to illustrate construction of stability domain

$$\Delta(j2\pi 700) = \text{diag}(+0.579 I_2, +0.523 I_3) \quad (3.34)$$

$$\Delta(j2\pi 729.2) = \text{diag}(-0.248 I_2, +0.248 I_3) \quad (3.35)$$

$$\Delta(j2\pi 750) = \text{diag}(-0.779 I_2, +0.071 I_3) \quad (3.36)$$

Table 3.9: Two uncertain parameters system - μ lower bound for points A, B, C

Points	Perturbation Matrix $\Delta(jw)$	$\bar{\sigma}(\Delta(jw))$	$\underline{\mu} = 1/\bar{\sigma}(\Delta(jw))$
A	$\Delta(j2\pi 700.0)$	0.579	1.73
B	$\Delta(j2\pi 729.2)$	0.248	4.03
C	$\Delta(j2\pi 750.0)$	0.779	1.28

The next step involves identifying the values of δ_{Cin} and δ_{Pin} from the extracted perturbation matrices, based on the structure of the uncertainty matrix (3.32). The normalised parameters are then converted into their actual values C_{in} and P_{in} , based on the (3.28). The corresponding values for matrices A, B and C are depicted in Table 3.10.

Table 3.10: Two uncertain parameters system - critical parameter values for points A, B, C

Perturbation Matrix	$\delta_{C_{in}}$	$\delta_{P_{in}}$	C_{in} (μF)	P_{in} (W)
A $\Delta(j2\pi700.0)$	+0.579	+0.523	100.5	12.2
B $\Delta(j2\pi729.2)$	-0.248	+0.248	92.6	11.3
C $\Delta(j2\pi750.0)$	-0.779	+0.071	87.6	10.6

Finally, the critical values of P_{in} are plotted against the critical values of C_{in} . Fig. 3.10 shows the resulting stability line. The points A, B and C shown in Fig. 3.10 serve to demonstrate how the μ chart has been ‘translated’ into a stability line.

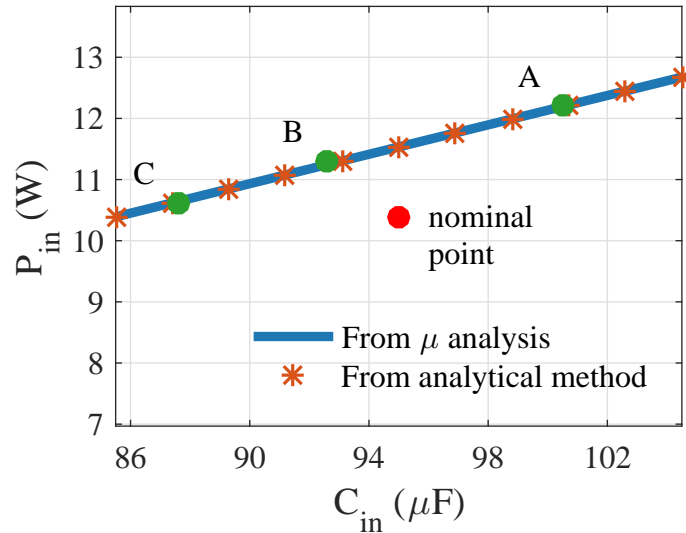


Figure 3.10: Two uncertain parameters system - stability domain from μ analysis and analytical method

In order to verify the validity of the stability line obtained from μ analysis, the input power P_{in} is computed for a number of values of C_{in} in the range $[85.5 \mu F, 104.5 \mu F]$ based on the analytical equation (3.26). The resulting plot of C_{in} against P_{in} is shown in Fig. 3.10. The boundary stability curve obtained from the analytical method matches the curve generated from μ analysis, as can be noted from Fig. 3.10. These findings validate the μ analysis results.

3.5.4 Robust stability domains

μ analysis identifies the smallest uncertainty matrix that can cause system instability, as given in (3.33) for the case under study. The robust stability margin, which is also the size of the critical matrix, is equal to $1/\mu=0.248$ as shown in Table 3.6. In parametric space and for a system subject to two parametric uncertainties, the μ approach identifies the largest square of coordinate size $1/\mu$ within which the system can be guaranteed robustly stable [34]. In order to illustrate this point, the squares connecting points A , B , C are drawn centred about the nominal point $(0,0)$, as shown in Fig. 3.11, 3.13 and 3.12 respectively.

The rectangle encompassing point A falls in both the stable and unstable regions, as depicted in Fig. 3.11. Although the rectangle connecting point 'C' falls entirely in the stable region, as shown in Fig. 3.12, it does not give the largest uncertainty size within all uncertain parameters, for which robust stability is guaranteed. The 'square' connecting point 'B' is completely in the stable region, and gives the largest parametric space inside of which the system is robustly stable, as shown in Fig. 3.13. Point B corresponds to the peak value of μ .

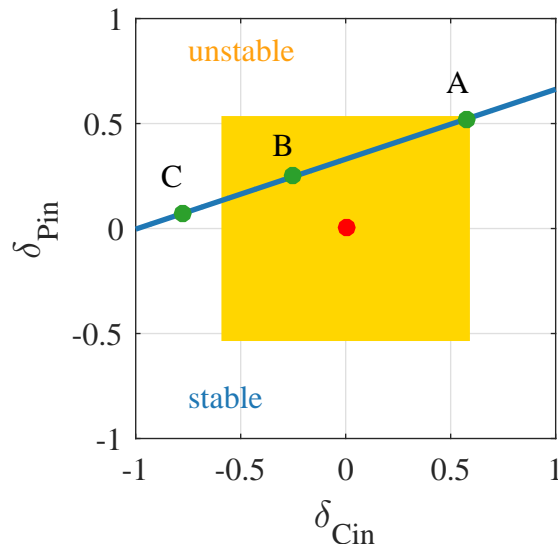


Figure 3.11: Two uncertain parameters system - rectangle centred about nominal point and connecting point A

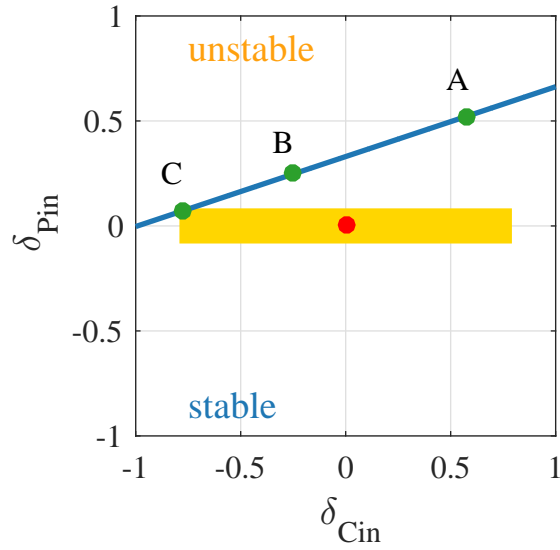


Figure 3.12: Two uncertain parameters system - rectangle centred about nominal point and connecting point C

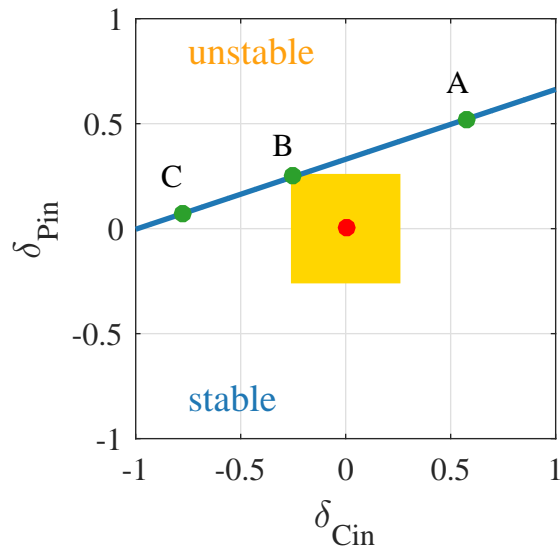


Figure 3.13: Two uncertain parameters system - largest square of coordinate size $(1/\mu)$ centred about nominal point and connecting point B, within which system is robustly stable

Hence, in order to ensure robust stability of the system, uncertainties have to stay within the ‘square’ region of size $1/\mu$ identified in Fig. 3.13. As discussed in chapter 2, the robust stability margin $1/\mu$, which is 0.248 in this case study, is also a measure of how much the maximum uncertainty range should be scaled to ensure robust stability of the EPS.

This subsection has shown how the μ approach provides the largest square of co-ordinate size $1/\mu$, centred about the nominal point, within which a system with two parametric uncertainties, can be guaranteed stable.

3.6 System with three parametric uncertainties

This subsection assesses stability robustness of the power system in Fig. 3.1 when it is subject to three parametric uncertainties P_{in} , C_{in} and L_{in} , as defined in Table 3.11. It also provides an insight into the meaning of μ by exploring the robust stability domains.

Table 3.11: Three uncertain parameters system (case III) - the uncertain parameters

Parameters	Nominal Value	Range of Variation
P_{in}	$P_{ino} = 10.4 \text{ W}$	$P_{invar} = \pm 33 \%$
C_{in}	$C_{ino} = 95 \mu\text{F}$	$C_{invar} = \pm 10 \%$
L_{in}	$L_{ino} = 511.8 \mu\text{H}$	$L_{invar} = \pm 10 \%$

3.6.1 μ analysis

After defining the uncertain system parameters C_{in} , L_{in} and P_{in} , as given in Table 3.11, robust stability is analysed using the μ tool. The μ chart is shown in Fig. 3.14a and 3.14b. The structure of the uncertainty matrix, as extracted from μ analysis, is shown in (3.37).

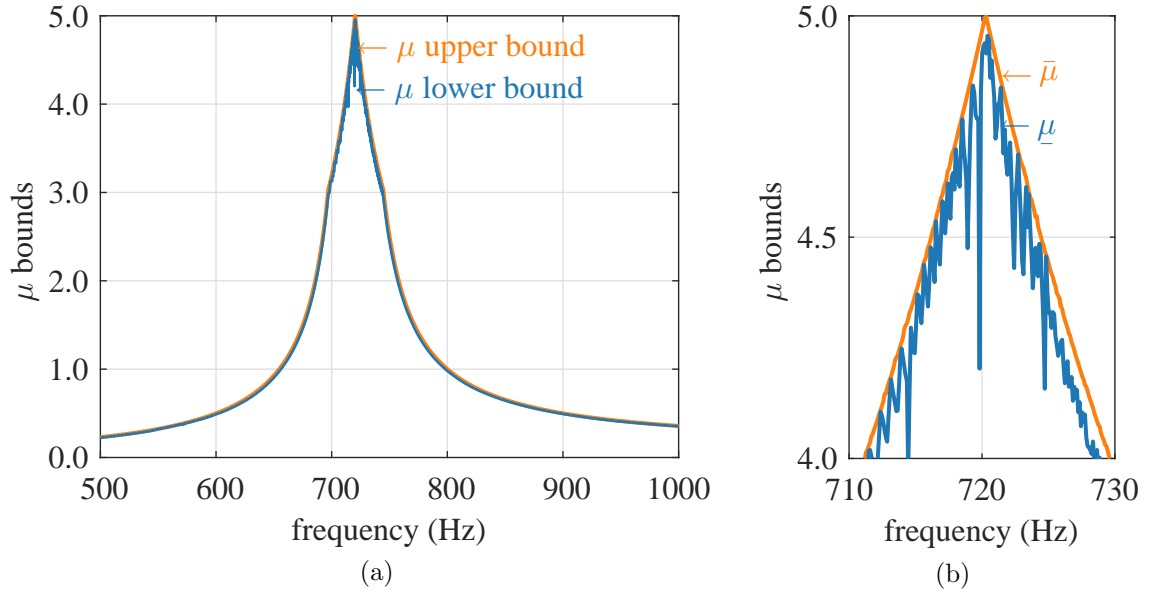


Figure 3.14: Two uncertain parameters system (a) μ chart to determine critical C_{in} , L_{in} , P_{in} (b) zoomed area near peak of μ chart

$$\Delta(j2\pi f) = \text{diag}(\delta_{C_{in}} I_2, \delta_{L_{in}} I_1, \delta_{P_{in}} I_3) \quad (3.37)$$

The maximum value of the μ lower bound is 4.974 and is nearly equal to that of the upper bound. The critical uncertainty matrix at the critical frequency of 720.5 Hz is shown in (3.38). The results are shown in Table 3.12.

$$\Delta(j2\pi 720.5) = \text{diag}(-0.201 I_2, -0.196 I_1, +0.201 I_3) \quad (3.38)$$

Table 3.12: Three uncertain parameters system - μ analysis results

Perturbation matrix $\Delta(jw)$	$\bar{\sigma}(\Delta(jw))$	$\underline{\mu}$
$\Delta(j2\pi 720.5)$	0.201	4.974

The values of $\delta_{C_{in}}$, $\delta_{L_{in}}$, $\delta_{P_{in}}$ pertaining to the critical uncertainty matrix can be obtained by comparing the elements of $\Delta(j2\pi 720.5)$ in (3.38) with the elements in (3.37), and are shown in Table 3.13. Further, the smallest parameter values that can destabilise the power system can be computed from these normalised values and the general LFT expression (3.28), as depicted in Table 3.13.

Table 3.13: Three uncertain parameters system - critical values of C_{in} , L_{in} , P_{in} from μ analysis

$\delta_{C_{in}}$	$\delta_{L_{in}}$	$\delta_{P_{in}}$	C_{in} (μF)	L_{in} (mH)	P_{in} (W)
-0.201	+0.196	+0.201	93.1	521.8	11.1

Of note is that the critical frequency is 720.5 Hz for this case study, as compared to 729.2 Hz in case study II, and 720.0 Hz is case I. This is owing to the fact that despite the critical capacitance decreasing to 93 μF from its initial value of 95 μF , the critical inductance has increased to 521.8 mH from its initial value of 511.8 mH , as shown in Table 3.13.

3.6.2 Analytical verification

In order to verify the μ analysis results in Table 3.13, the input power P_{in} and frequency f are computed from the analytical equations (3.26) - (3.27), with C_{in} and L_{in} set to the critical values of 93.1 μF and 521.8 mH respectively. The analytical results match μ analysis predictions as shown in Table 3.14. This confirms that μ analysis has identified critical parameters at the boundary of stability for the case under study.

Table 3.14: Three uncertain parameters system - μ analysis and analytical results of critical P_{in} and f

	μ analysis results	Analytical results
Critical input power (P_{in})	11.1 W	11.1 W
Critical frequency (f)	720.5 Hz	720.5 Hz

3.6.3 Stability domains

This subsection translates frequency-based μ results into parametric space. It provides insights into the usefulness of μ in the identification of the parametric space within which a system is guaranteed stable.

3.6.3.1 μ in parametric space

In order to generate the stability domain of the power system under consideration, perturbation matrices are firstly extracted at a number of frequency points on the chart of the μ lower bound shown in Fig. 3.15. For the purpose of illustration, three uncertainty matrices corresponding to the points A , B and C in Fig. 3.15, and given in (3.39), (3.40) and (3.41) respectively, are analysed.

$$\Delta(j2\pi700) = \text{diag}(+0.241 I_2, +0.333 I_1, +0.301 I_3) \quad (3.39)$$

$$\Delta(j2\pi720.5) = \text{diag}(-0.201 I_2, -0.196 I_1, +0.201 I_3) \quad (3.40)$$

$$\Delta(j2\pi750) = \text{diag}(-0.399 I_2, -0.399 I_1, +0.330 I_3) \quad (3.41)$$

The next step involves identifying the values of $\delta_{C_{in}}$, $\delta_{L_{in}}$ and $\delta_{P_{in}}$ for each of the perturbation matrices. This is done by comparing the elements of the matrices with the elements of the general uncertainty matrix (3.37). The normalised parameter values for points A , B and C are given in Table 3.15 along with the corresponding computed values of C_{in} , L_{in} and P_{in} , which are computed from (3.28).

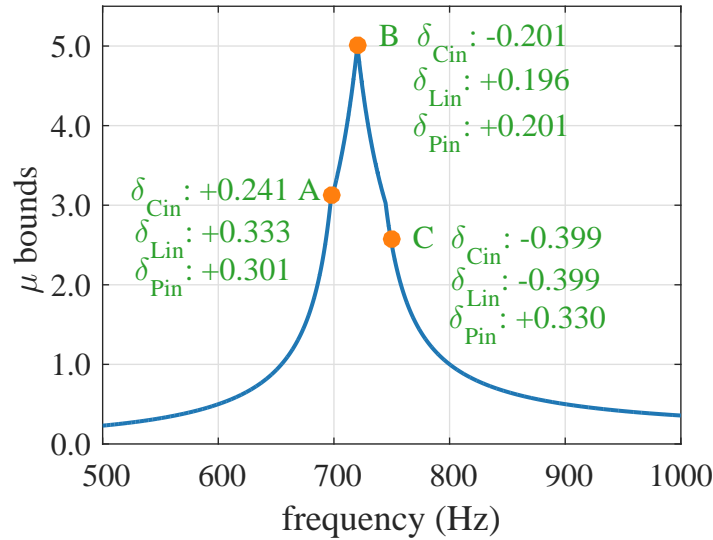


Figure 3.15: Three uncertain parameters system - points A, B, C chosen to illustrate construction of stability domains

Table 3.15: Three uncertain parameters system - critical parameter values for points A, B and C

	δ_{Cin}	δ_{Lin}	δ_{Pin}	C_{in} (μF)	L_{in} (mH)	P_{in} (W)
A	+0.241	+0.333	+0.301	97.3	528.9	11.4
B	-0.201	+0.196	+0.201	93.1	521.8	11.1
C	-0.399	-0.399	+0.330	91.2	491.4	11.5

The coordinates $(\delta_{Cin}, \delta_{Lin}, \delta_{Pin})$, extracted from the μ chart, are then plotted in three dimensional space. The resulting chart is depicted in Fig. 3.16. The points A, B and C shown in Fig. 3.16 serve to demonstrate how the μ chart in Fig. 3.15 has been ‘translated’ from frequency domain to parametric space.

3.6.3.2 Stability plane from analytical method

In order to gain more insight into the μ approach, in this subsection the stability domains for the system under study are firstly determined through the analytical method and then correlated with the μ lower bound chart.

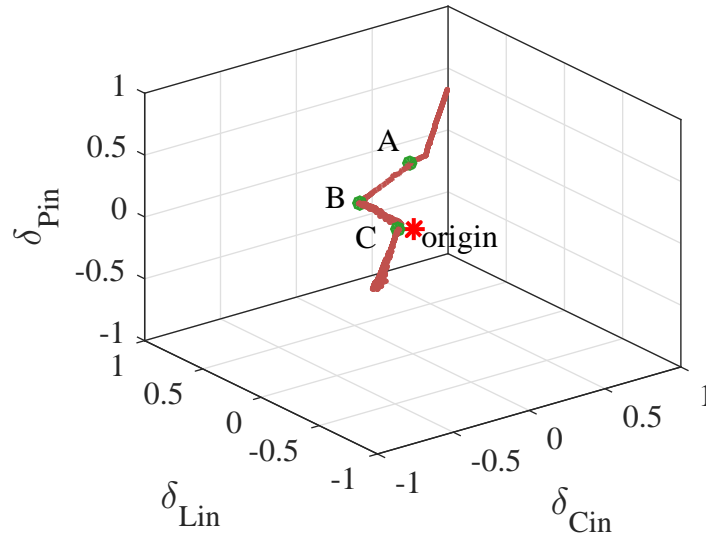


Figure 3.16: Three uncertain parameter system - μ lower bound chart translated into parametric space

A series of points (C_{in}, L_{in}) are chosen in the range of $C_{in} = 95 \mu F \pm 10\%$ and $L_{in} = 511.8 mH \pm 10\%$; then P_{in} is calculated iteratively for each coordinate point according to (3.25). The resulting coordinates (C_{in}, L_{in}, P_{in}) are then converted into their normalised form $(\delta_{cin}, \delta_{Lin}, \delta_{Pin})$ using the generic equation (3.28) and the parameter values in Table 3.1. The three-dimensional plot of the coordinates, as shown in Fig. 3.17, is the boundary stability plane for the system under study. The system is stable for all sets of parameters chosen in the region below the stability plane and is unstable for all sets of parameters chosen in the region above the stability plane.

When the μ lower bound chart in Fig. 3.16 is superimposed on the analytically obtained stability plane, it is found to lie exactly on the plane as shown in Fig. 3.17. This proves that the critical parameters determined by the μ lower bound for this case study lie at the boundary of stability.

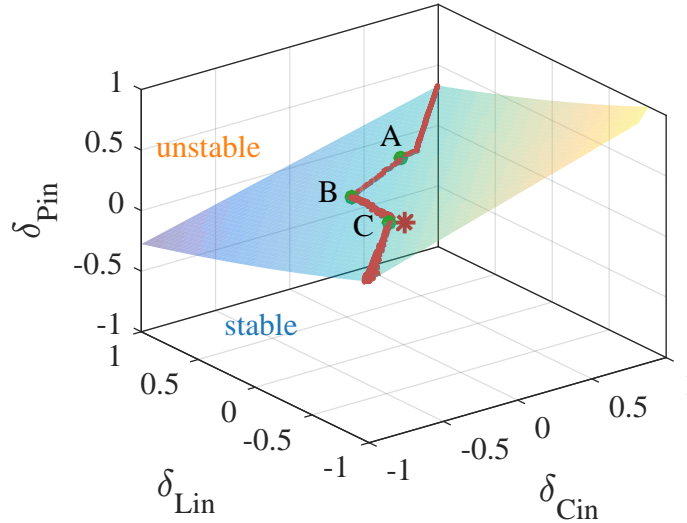


Figure 3.17: Three uncertain parameters system - stability boundary plane from analytical method and μ chart translated into parametric space

3.6.3.3 Significance of μ in frequency domain

As can be seen in Fig. 3.17, the μ chart connects only a few of the parameter coordinates within the wide stability plane. This is because the employed algorithm does not verify all the points of the stability plane. Instead, it monitors the boundary stability for migration of those poles, which correspond to the smallest destabilising uncertainty matrices, at every frequency point within the grid. The smallest of all the destabilising perturbation matrices over the entire frequency grid gives $1/\mu$, in accordance with (2.13). In order to demonstrate this point, this subsection computes μ from the parameter coordinates in the analytical plane in Fig. 3.17. The procedure employed is based on the definition of μ in (2.13), which states that $\mu_{\Delta}(M(j\omega)) = 1/\min[\bar{\sigma}(\Delta(j\omega))]$. The steps are outlined in Fig. 3.18 and illustrated below:

1. A frequency grid is chosen as a set of 100 points spaced between 500 Hz and 1000 Hz. (Suggestions for the selection of the grid for μ analysis are given in the appendix A.)

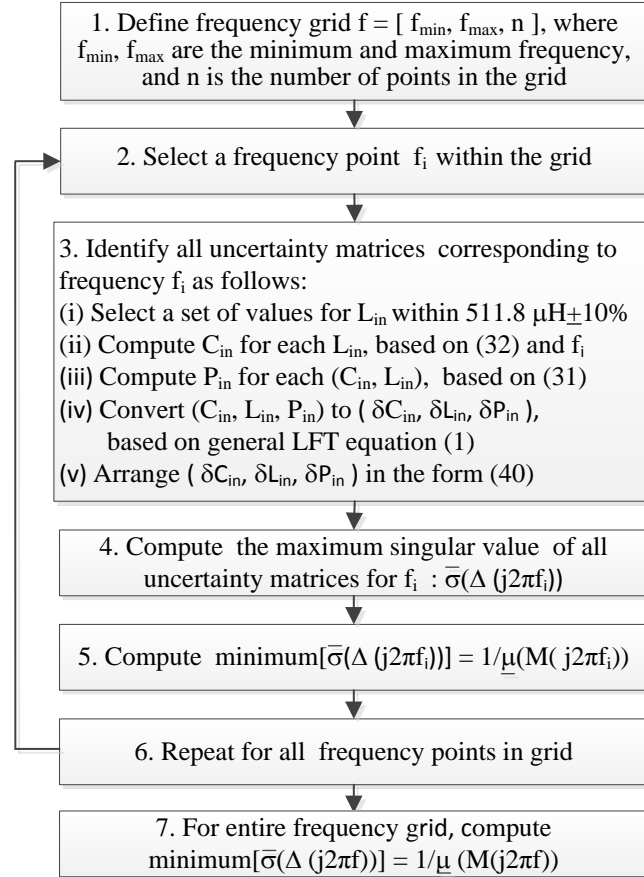


Figure 3.18: Flow chart for computing the smallest critical uncertainty matrix for a given system frequency

2. A frequency of 700 Hz is selected for analysis.
3. A number of uncertainty matrices corresponding to coordinates $(\delta C_{in}, \delta L_{in}, \delta P_{in})$ and pertaining to 700 Hz are computed. These coordinates, plotted in Fig. 3.19, are shown to lie exactly on the stability plane.
4. The maximum singular value of each of the uncertainty matrices, lying on the frequency line of 700 Hz, is computed. For illustration, the maximum singular value is computed for three points, denoted as 1, 2 and 3 in Fig. 3.19, as shown in Table 3.16.

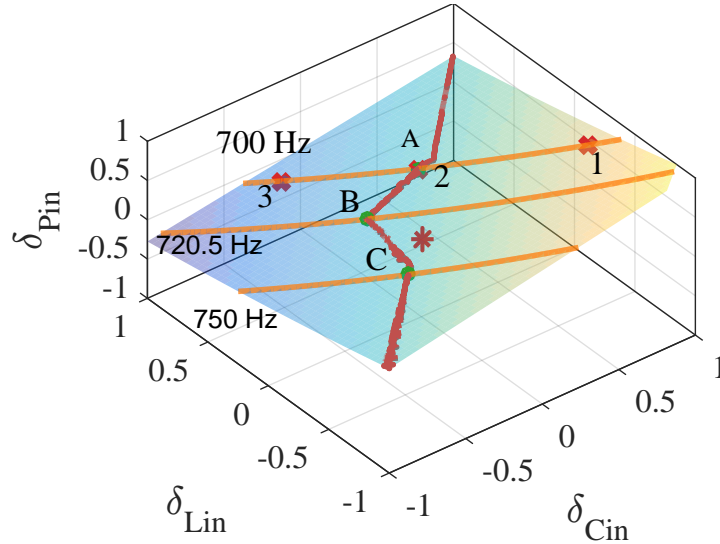


Figure 3.19: Three uncertain parameters system - frequency curves for 700 Hz, 720.5 Hz and 750 Hz on stability boundary plane, obtained from analytical method

Table 3.16: Three uncertain parameters system -maximum singular value of matrices 1, 2 and 3 on frequency curve 700 Hz

Pts	δ_{Cin}	δ_{Lin}	δ_{Pin}	$\bar{\sigma}(\Delta(j2\pi 700))$	$\min[\bar{\sigma}(\Delta(j2\pi 700))]$
1	+0.869	-0.270	+0.720	0.869	-
2	+0.244	+0.330	+0.303	0.330	0.330
3	-0.243	+0.850	-0.005	0.850	-

- The smallest uncertainty matrix on the frequency curve 700 Hz is then identified. This corresponds to point 2 which matches point A on the $\underline{\mu}$ chart in Fig. 3.16, as shown in Table 3.16. Hence, the critical perturbation matrix at a given frequency point on the $\underline{\mu}$ chart is found to be the smallest uncertainty matrix that can destabilise the system at that frequency.
- The above exercise is repeated for all frequency points within the grid. The smallest matrix on the frequency lines 720.5 Hz and 750 Hz correspond to points B and C respectively as shown in Fig. 3.19 and in Table 3.17.

Table 3.17: Three uncertain parameters system - smallest matrices on frequency lines 700 Hz, 720.5 Hz and 750 Hz

frequency	$(\delta_{Cin}, \delta_{Lin}, \delta_{Pin})$	$\bar{\sigma}(\Delta(jw))$ $= 1/\bar{\mu}(\Delta(jw))$	$\mu_{\Delta}(M(jw))$
700 Hz	A (+0.241, +0.333, +0.301)	0.333	3.00
720.5 Hz	B (-0.201, +0.196, +0.201)	0.201	4.97
750 Hz	C (-0.399, +0.399, +0.330)	0.399	2.51

7. When all the computed uncertainty matrices on the μ chart are analysed, it is found that the smallest matrix over the entire frequency grid corresponds to point B or the peak of the μ chart. This is shown in Table 3.18.

Table 3.18: Three uncertain parameters system - μ computed from coordinate points on stability plane

Frequency (f)	$\min[\bar{\sigma}(\Delta(j2\pi f))]$	$\mu_{\Delta}(M(j2\pi f))=1/\min[\bar{\sigma}(\Delta(j2\pi f))]$
500 Hz - 1000 Hz	0.201	4.974

3.6.4 Robust stability domains

Following the analysis in the earlier subsection, the smallest destabilising perturbation matrix on the boundary stability plane corresponds to point B on the μ chart. This can be noted by comparing the sizes of the uncertainty matrices A, B and C in Table 3.17. The peak value of the μ plot thus provides the largest perturbation matrix that the system is robustly stable against over the entire frequency grid. With respect to parametric space, $\bar{\sigma}(\Delta(jw)) = 1/\bar{\mu}$ can be interpreted as the coordinate size of the largest cube centred around the nominal point (0, 0, 0) inside of which the system is guaranteed robustly stable. The robust stability margin ($1/\bar{\mu}$) also denotes the ratio by which the maximum range of the uncertain parameters must be adjusted for the system to be robustly stable, as discussed in Chapter 2.

For the purpose of illustration, a set of rectangular cuboids centred about the nominal point $(0,0,0)$ are drawn to connect points A , B and C respectively. From Fig. 3.20, it can be noted that the cuboid connecting point A falls in both the stable and the unstable regions. This is also the case for point C .

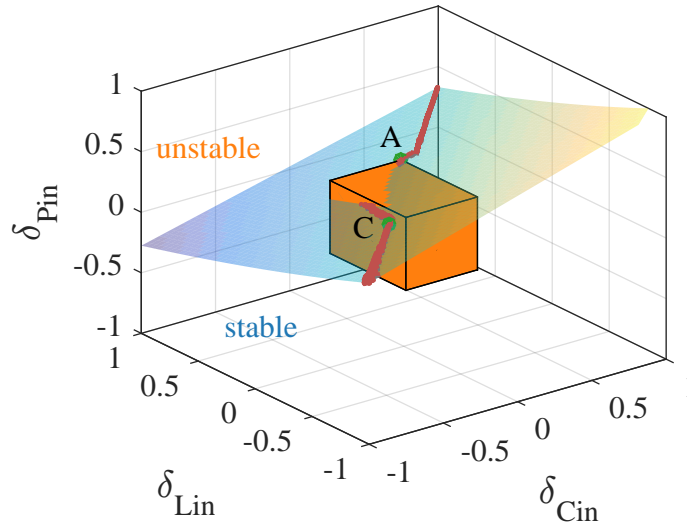


Figure 3.20: Three uncertain parameters system - part of the cuboid centred about the origin and connecting point A falls in the unstable region

In contrast, the cube of coordinate size $1/\mu = 0.201$ connecting point B lies totally in the stable region below the stability plane as depicted in Figs. 3.21 and 3.22. It is to be pointed out that the small yet noticeable discrepancies in the normalised values in the uncertainty matrix (3.38) of point B have been neglected and attributed to numerical inaccuracies. The system is robustly stable for all variations in uncertainties that may occur within that ‘cube’.

This subsection has shown that the μ approach identifies the largest ‘cube’ in dimensional parametric space inside which an EPS, with three parametric uncertainties, is guaranteed to be robustly stable.

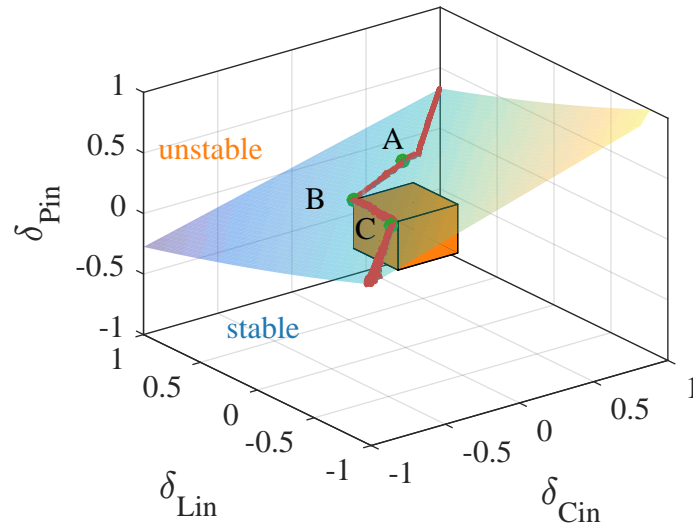


Figure 3.21: Three uncertain parameters system - largest cube of coordinate size $(1/\mu)$ centred about nominal point and connecting point B, within which system is stable

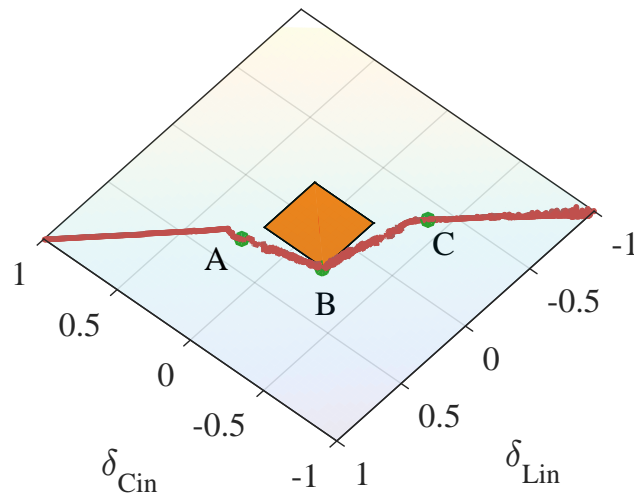


Figure 3.22: Three uncertain parameters system - top view of Fig. 3.21

3.7 System with multiple parametric uncertainties

By extrapolating on the ideas presented in the earlier subsections, for a system subject to N parametric uncertainties, μ analysis provides the largest hypercube of dimension N centred about the nominal point and of coordinate size $1/\mu$, within which system robust stability can be guaranteed [34]. For a single parametric uncertainty, the hypercube becomes the largest line segment within which the system is guaranteed robustly stable. The line segment is of coordinate size $1/\mu = 0.331$ for case study I. Similarly, when two parametric uncertainties are considered, the hypercube becomes the largest square in the unit bound normalised parameter space within which system robust stability is guaranteed; in case study II this is a square of coordinate size $1/\mu = 0.248$. When considering a system subject to three parametric uncertainties, μ analysis identifies the largest cube within which system robust stability is guaranteed, which in case study III is of coordinate size $1/\mu = 0.201$. Of note is that the initial selection of the nominal values as well as the interval of parameter variations will influence the outcome of the robust stability assessment of a system.

It is interesting to note that the coordinate size of the ‘hypercube’ or $1/\mu$ tends to decrease with increasing number of uncertainties, as depicted in Table 3.19. This clearly shows that stability assessment, if performed without duly incorporating potential system uncertainties, can lead to optimistic and possibly erroneous stability margins.

Table 3.19: Variation of robust stability margin with number of uncertain parameters

Number of parametric uncertainties	Robust stability margin ($1/\mu$)	Critical power (P_{in})
1	0.331	11.53 W
2	0.248	11.25 W
3	0.201	11.10 W

3.8 Conclusion

This chapter has brought deeper insight into the meaning of μ with respect to multiple parametric uncertainties.

- The novelty of this study is that it has exploited and applied the concept of the hypercube, in view of bringing more clarity to the concept of μ . Although the hypercube has been discussed in the literature, it has been defined at a purely conceptual level. This chapter has constructed the hypercube of a basic EPS connected to an ideal CPL when it is subject to multiple parametric uncertainties. This has been made possible through the extraction of data from perturbation matrices generated during μ analysis of the system.
- Through the constructed hypercube, this study has demonstrated how, for a system subject to N parametric uncertainties, the μ approach provides the largest hypercube of dimension N , centred about the nominal point and of coordinate size $1/\mu$, within which the system can be guaranteed to be robustly stable. $1/\mu$ is the robust stability margin of the system. For the EPS under study, it has been shown how robust stability can be ensured within a line segment of coordinate size $1/\mu = 0.331$ when the system has a single parametric uncertainty in its power P ; a square of coordinate size $1/\mu = 0.248$ when the system has two parametric uncertainties in P and its capacitance C_{in} ; and a cube of coordinate size $1/\mu = 0.201$ when the system has three parametric uncertainties in P , C_{in} and its inductance L_{in} .
- This chapter has translated the μ results from the frequency domain into the more perceivable parametric space, thus bringing better understanding to the μ method. Further it has shown the correlation between μ and the critical perturbation matrices on the μ chart.

The findings in this study have several practical implications. The design engineer is offered the possibility of working with the μ results in the more perceivable para-

metric domain, and better interpret the robust stability measure μ . The hypercube, illustrated in this work, offers the design engineer a space within which to choose optimum parameters for design while ensuring stability robustness. The chapter has been presented in a manner comprehensible enough to make the μ approach more applicable to a wide range of uncertain systems subject to multiple simultaneous parametric uncertainties.

Chapter 4

A practical approach to μ analysis

4.1 Introduction

Power electronics is becoming an integral part of MET applications. Yet, the susceptibility of power electronic systems to instability remains an important issue that needs attention. Finding an answer to this problem is crucial, particularly for the safety critical applications. Power electronic technology is fast evolving. Yet, the methods that are widely employed to assess the stability of these systems are still based on classical techniques. These include the eigenvalue approach and impedance methods based on Nyquist stability criterion. Despite their numerous benefits, the classical methods treat the physical system as a fixed model, where all the system components have unique values. However, the physical systems are complex and dynamic. The properties of their system components are continuously varying due to changes in both their operating and environmental conditions. Classical methods may attempt to include these uncertainties in the analysis through the extensive iteration process. However, they are designed for SISO systems, and may not produce reliable results when applied to MIMO systems [31],[33]. In order to keep pace with evolving technology in power electronics, there is a need to adopt new analysis techniques, that duly account for uncertainties that are present in physical systems.

Considering the case where the stability of a physical system is assessed based on its nominal model, the outcome of the analysis is necessarily dependent on the quality of that model. In an attempt to increase the accuracy of the analysis, the nominal model may be greatly refined to match the physical system. However, in practice, excessive model refinement is unlikely to be viable. In addition, certain system components, such as system parasitics and non-linear elements, are hard to quantify. It can be inferred that a nominal system model is bound to contain model uncertainties. From another viewpoint, even though the nominal model may be very accurate, it may not truly represent the physical system. In practice, these systems are subject to multiple sources of uncertainties, which may arise due to variations in operating or environmental conditions. In face of all the uncertainties, that may be present in the nominal model and in the physical system, the need for a robust tool to assess system stability can only be reinforced.

The μ method is a robust approach that can be employed to incorporate uncertainties in stability analysis. In order to effectively apply the method, in addition to a sound understanding of its theoretical framework, sufficient knowledge is required as regards its application through the use of associated software. Practical approaches to applying the μ method so as to cater for the aforementioned uncertainties in the power electronic area needs to be explored. Further, it seems important to identify to what extent uncertainties can affect the outcome of stability assessments and, consequently determine the importance of including them in the analysis, through the adoption of tools such as the μ approach.

While chapters 2 and 3 have treated the μ theoretical framework in great depth, this chapter aims to present practical approaches to applying the μ tool in the robust stability assessment of PE systems. This is to be achieved by demonstrating how few key system uncertainties can be incorporated in the examination of the robust stability margin of the widely used DC/DC buck converter system. The sources of uncertainties to be considered include variations in system load, source impedance, operating temperature as well as uncertainties in the nominal model including some non-linearities. The μ predictions are to be evaluated against experimental results

both in the time domain and in the frequency domain. In addition, the case studies, presented in this chapter, are to be used as a basis to assess the impact of uncertainties on system stability, and to gauge the need for robust analysis tools.

4.2 Modelling of the buck converter for μ analysis

The electrical network of the MET will consist of a large number of power electronic converters. The regulated DC/DC converter is known to be a critical and very important component of the on-board electrical system of the aircraft [31]. It is used to interface sections of the EPS having different voltage levels, for instance 270 V to 28 V. These applications include battery charging and energy storage interfacing. This study is based on the buck converter system, being widely used for the DC/DC power conversion for such applications.

In this section, the small-signal ac models of the power stage and the controller are built separately and then combined to yield the complete linear time invariant (LTI) model of the closed loop converter [13],[51],[60],[61]. Further, it applies a general modelling method to convert the non-linear buck converter system in an equivalent linear model, which is valid for μ analysis over a range of operating points and parameter variations [58],[62]. The method is based on symbolic linearisation around an arbitrary equilibrium point. All elements in the system model are explicitly expressed in terms of definable system parameters and input only, and for instance not in terms of indeterminate equilibrium states. The method, not being the focus in this study, is not emphasised in this chapter. It will be examined in more detail in chapter 5.

4.2.1 The experimental buck converter

The experimental closed loop buck converter, that is used in this study, is depicted in the circuit model in Fig. 4.1, and shown in Fig. 4.2 [63]. The converter consists of a

U3825 PWM controller, a Type III analogue compensator and an LC input filter. The switching frequency has been measured as 51.2 kHz [64]. The sawtooth generator of the modulator generates a sawtooth waveform of peak voltage (V_{pp}) measured as 3.52 V . The modulation gain f_m is given by $1/V_{pp}$ and is equal to 0.284 . It is the transfer function of the modulator and refers to the change in duty cycle d as a result of changing input control voltage V'_{com} , as shown in Fig. 4.1 [65]. The comparator compares the control voltage to the ramp voltage and in so doing generates the gate drive signal as a rectangular waveform signal to the MOSFET. This switched output voltage v_d is averaged by the output filter and applied to the load as the output voltage v_o . The controller has been designed with a phase margin of 55° and a bandwidth of 4.2 kHz . The small-signal ac model of the closed loop controlled buck converter, which is illustrated in Fig. 4.1, is developed in the subsequent subsections. The system parameters are defined in Table 4.1.

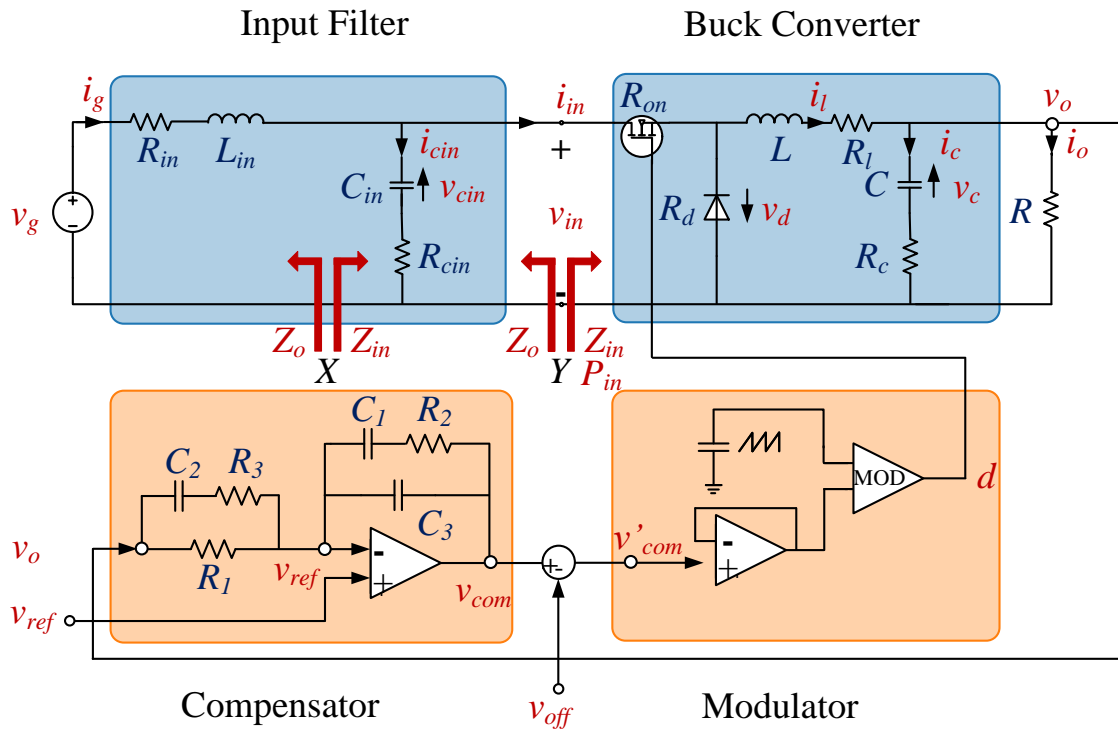


Figure 4.1: Circuit representation of the closed loop controlled buck converter with input filter

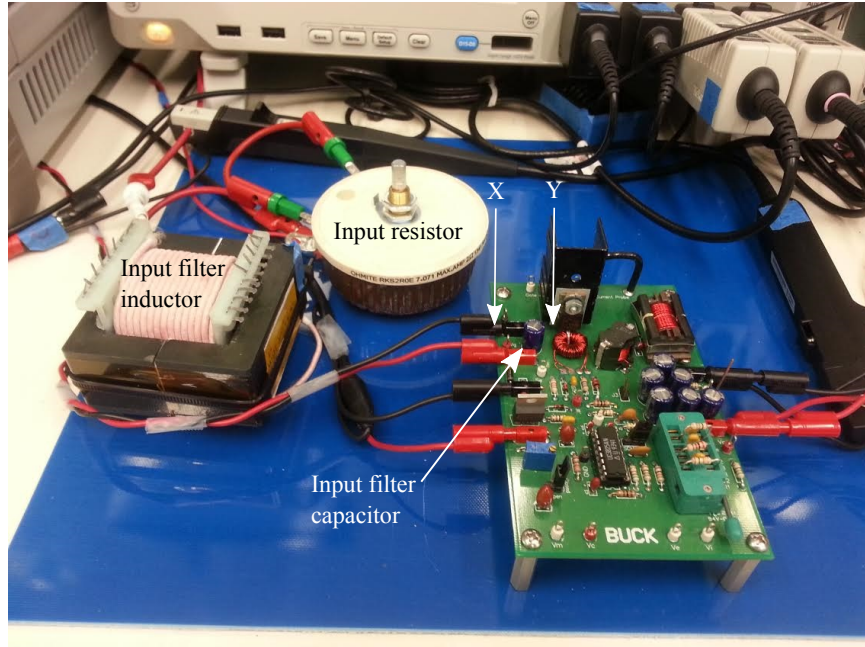


Figure 4.2: The experimental closed loop controlled buck converter with input filter

4.2.2 Power stage model

The buck converter has two operating modes over one switching period. The equations (4.1) and (4.2) describe the dynamics of the power stage when the switch is on and off respectively. The parameters in (4.1) - (4.2) are shown in Fig. 4.1, and Table 4.1.

$$\begin{aligned}
 \text{On-state period: } \quad \frac{di_g}{dt} &= ((v_g - i_g R_{in}) - (v_{cin} + (i_g - i_l) R_{cin}))/L_{in} \\
 \frac{dv_{cin}}{dt} &= (i_g - i_l)/C_{in} \\
 \frac{di_l}{dt} &= ((v_{cin} + (i_g - i_l) R_{cin}) - (v_o + i_l R_{lon}))/L \\
 \frac{dv_c}{dt} &= (i_l - (v_o/R))/C
 \end{aligned} \tag{4.1}$$

$$v_o(t) = (R_c i_l + v_c)(R/(R_c + R))$$

$$\begin{aligned}
\text{Off-state period: } \quad \frac{di_g}{dt} &= ((v_g - i_g R_{in}) - (v_{cin} + (i_g)R_{cin}))/L_{in} \\
\frac{dv_{cin}}{dt} &= i_g/C_{in} \\
\frac{di_l}{dt} &= (-v_d - (v_o + i_l R_{ld}))/L \\
\frac{dv_c}{dt} &= (i_l - (v_o/R))/C
\end{aligned} \tag{4.2}$$

$$v_o(t) = (R_c i_l + v_c)(R/(R_c + R))$$

$$\text{where } R_{lon} = R_l + R_{on}, \quad R_{ld} = R_l + R_d,$$

Table 4.1: Nominal values for system parameters

Symbol	Units	Nominal values	Description
v_g	V	19.8	DC source voltage
v_{ref}	V	5.1	Reference Voltage
v_d	V	0.22	Diode Voltage
v_{off}	V	2.352	Offset Voltage
f_s	kHz	51.0	Switching frequency
f_m	-	0.284	Modulator gain
R	Ω	2.50	Load resistance
R_{on}	m Ω	160	Switch on resistance
R_d	m Ω	12	Diode on resistance
R_{in}	m Ω	100	Input Resistance
L_{in}	μH	500	Input filter inductance
C_{in}	μF	100	Input filter capacitance
R_{cin}	m Ω	47	ESR of input filter capacitor
L	μH	42	Output filter inductance
R_l	m Ω	45	ESR of output filter inductor
C	μF	590	Output filter capacitance
R_c	m Ω	10	ESR of output filter capacitor
R_1	k Ω	20.0	Resistance in compensator
R_2	k Ω	20.0	Resistance in compensator
R_3	k Ω	2.0	Resistance in compensator
C_1	nF	8.22	Capacitance in compensator
C_2	nF	4.72	Capacitance in compensator
C_3	nF	0.331	Capacitance in compensator

In order to convert the time variant system into a time invariant system, the averaging modelling method is applied. Equations (4.1) and (4.2) are firstly represented as the state equations (4.3) and (4.4) respectively, with state vectors $x(t)$: $[i_g(t), v_{cin}(t), i_l(t), v_c(t)]$, input vector $u(t)$: $[v_g(t), v_d(t)]$ and output vector $y(t)$: $[v_o(t)]$.

$$\frac{dx(t)}{dt} = A_1x(t) + B_1u(t), \quad y(t) = E_1x(t) + F_1u(t) \quad (4.3)$$

$$\frac{dx(t)}{dt} = A_2x(t) + B_2u(t), \quad y(t) = E_2x(t) + F_2u(t) \quad (4.4)$$

Then, averaging (4.3) and (4.4) over a switching period produces the averaged time invariant system model as given by (4.5). This is based on the duty cycle $d(t)$ during the on-state period and $d'(t) = 1 - d(t)$ during the off-state period.

$$\begin{aligned} \frac{d\overline{x(t)}}{dt} &= [d(t)A_1 + d'(t)A_2]\overline{x(t)} + [d(t)B_1 + d'(t)B_2]\overline{u(t)} \\ \overline{y(t)} &= [d(t)E_1 + d'(t)E_2]\overline{x(t)} + [d(t)F_1 + d'(t)F_2]\overline{u(t)} \end{aligned} \quad (4.5)$$

The averaged model (4.5) is non-linear as it involves the multiplication of time varying quantities. In order to obtain the linear small-signal ac model of the system, the averaged model must be linearised about a dc steady state operating point. To that end, the variables in (4.5) are firstly expanded in terms of their dc and ac components. The averaged state vector $\overline{x(t)}$, input vector $\overline{u(t)}$, output vector $\overline{y(t)}$ and duty cycle $d(t)$ are expressed in terms of their dc steady state values X , U , Y and D with superimposed small ac variations $\hat{x}(t)$, $\hat{u}(t)$, $\hat{y}(t)$ and $\hat{d}(t)$ respectively as shown in (4.6). It can be shown that $\hat{d}(t) = -\hat{d}'(t)$.

$$\begin{aligned} \overline{x(t)} &= X + \hat{x}(t), & \overline{u(t)} &= U + \hat{u}(t) \\ \overline{y(t)} &= Y + \hat{y}(t), & d(t) &= D + \hat{d}(t) \end{aligned} \quad (4.6)$$

After substituting (4.6) in (4.5) and collecting common terms, the averaged state space model can be written as (4.7) and (4.8).

$$\begin{aligned}
\frac{d(\hat{x}(t))}{dt} &= AX + BU \\
&+ A\hat{x}(t) + B\hat{u}(t) + ((A_1 - A_2)X + (B_1 - B_2)U)\hat{d}(t) \\
&+ (A_1 - A_2)\hat{x}(t)\hat{d}(t) + (B_1 - B_2)\hat{u}(t)\hat{d}(t)
\end{aligned} \tag{4.7}$$

$$\begin{aligned}
Y + \hat{y}(t) &= EX + FU \\
&+ E\hat{x}(t) + F\hat{u}(t) + ((E_1 - E_2)X + (F_1 - F_2)U)\hat{d}(t) \\
&+ (E_1 - E_2)\hat{x}(t)\hat{d}(t) + (F_1 - F_2)\hat{u}(t)\hat{d}(t)
\end{aligned} \tag{4.8}$$

The averaged model in steady state corresponds to the dc terms in (4.7) and (4.8) and is given as (4.9).

$$0 = AX + BU, \quad Y = EX + FU \tag{4.9}$$

$$\begin{aligned}
\text{where } A &= A_1D + A_2D', \quad B = B_1D + B_2D' \\
E &= E_1D + E_2D', \quad F = F_1D + F_2D' \\
D' &= 1 - D
\end{aligned} \tag{4.10}$$

The equilibrium state can be computed as ($X = -BUA^{-1}$) with $U = [V_g, V_d]^T$ based on (4.9). Besides, the duty cycle D in (4.10) can be obtained from (4.11) which is based on the equivalent steady-state model of the buck converter in Fig.4.3.

$$\begin{aligned}
D^2V_o\frac{R_{in}}{R} + D[-V_g - V_d + V_o\frac{(R_{on} - R_d)}{R}] \\
+ [V_d + V_o\frac{(R + R_d + R_l)}{R}] = 0
\end{aligned} \tag{4.11}$$

Symbolic linearisation of the averaged model about the quiescent dc point, given by (4.9), then involves neglecting the second order non-linear terms in (4.7) - (4.8) as

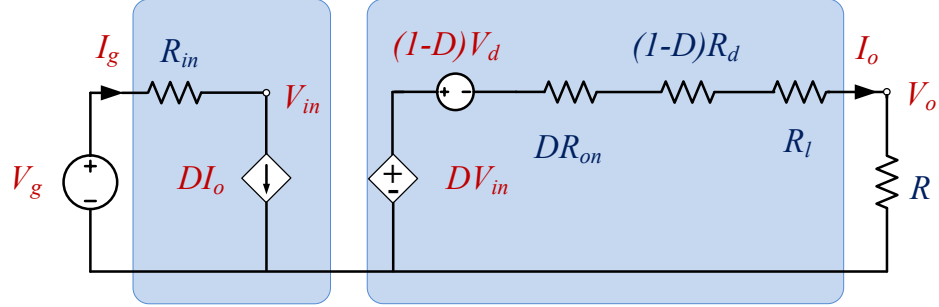


Figure 4.3: Model of the buck converter in steady state

they are very small in magnitude when compared to the linear terms. The resulting linearised small-signal ac model, in symbolic form, is obtained as (4.12) in its generalised form and as (4.13) - (4.14) in its full form. Of note is that the elements in (4.13) - (4.14) are explicitly in terms of system parameters and inputs only.

$$\begin{aligned} \frac{d(\hat{x}(t))}{dt} &= A\hat{x}(t) + B\hat{u}(t) + ((A_1 - A_2)X + (B_1 - B_2)U)\hat{d}(t) \\ \hat{y}(t) &= E\hat{x}(t) + F\hat{u}(t) + ((E_1 - E_2)X + (F_1 - F_2)U)\hat{d}(t) \end{aligned} \quad (4.12)$$

$$\begin{aligned} \frac{d\hat{i}_g(t)}{dt} &= \frac{-(R_{cin} + R_{in})}{L_{in}}\hat{i}_g(t) - \frac{1}{L_{in}}\hat{v}_{cin}(t) \\ &\quad + \frac{DR_{cin}}{L_{in}}\hat{i}_l(t) + \frac{1}{L_{in}}\hat{v}_g(t) + p_1\hat{d}(t) \\ \frac{d\hat{v}_{cin}(t)}{dt} &= \frac{1}{C_{in}}\hat{i}_g(t) - \frac{D}{C_{in}}\hat{i}_l(t) + p_2\hat{d}(t) \\ \frac{d\hat{i}_l(t)}{dt} &= \frac{DR_{cin}}{L}\hat{i}_g(t) + \frac{D}{L}\hat{v}_{cin}(t) + \frac{q}{L}\hat{i}_l(t) \\ &\quad - \frac{R}{L(R + R_c)}\hat{v}_c(t) + \frac{D-1}{L}\hat{v}_d(t) + p_3\hat{d}(t) \\ \frac{d\hat{v}_c(t)}{dt} &= \frac{R}{C(R + R_c)}\hat{i}_l(t) - \frac{1}{C(R + R_c)}\hat{v}_c(t) \end{aligned} \quad (4.13)$$

$$\hat{v}_o(t) = \frac{R_c R}{R_c + R} \hat{i}_l(t) + \frac{R}{R_c + R} \hat{v}_c(t) \quad (4.14)$$

$$\text{where } k_1 = R + R_l + R_d + D^2(R_{in} - R_{cin}) \\ + D(R_{cin} - R_d + R_{on})$$

$$k_2 = \frac{RR_c}{R + RC}, \quad k_3 = DV_g + (D - 1)V_d$$

$$k_4 = (R + R_l + R_d)V_g + DR_{in}V_d + DR_{cin}V_g \\ + D(R_{on} - R_d)V_g - D^2(R_{cin}V_g + R_{in}V_d)$$

$$p_1 = \frac{R_{cin}k_3}{L_{in}k_1}$$

$$p_2 = -\frac{k_3}{C_{in}k_1}$$

$$p_3 = \frac{k_3(R_d - R_{cin} - R_{on})}{Lk_1} + \frac{k_4}{Lk_1} + \frac{DR_{cin}k_3}{Lk_1} + \frac{V_d}{L}$$

It is to be noted that all elements in the developed model must be in their rational forms in order to allow conversion of the system model in its corresponding LFT configuration. The duty cycle D in (4.13) being irrational is therefore approximated by a polynomial expansion. Fig. 4.4 shows the rational 0th, 1st and 2nd order Taylor series expansions of duty cycle D about the nominal operating point.

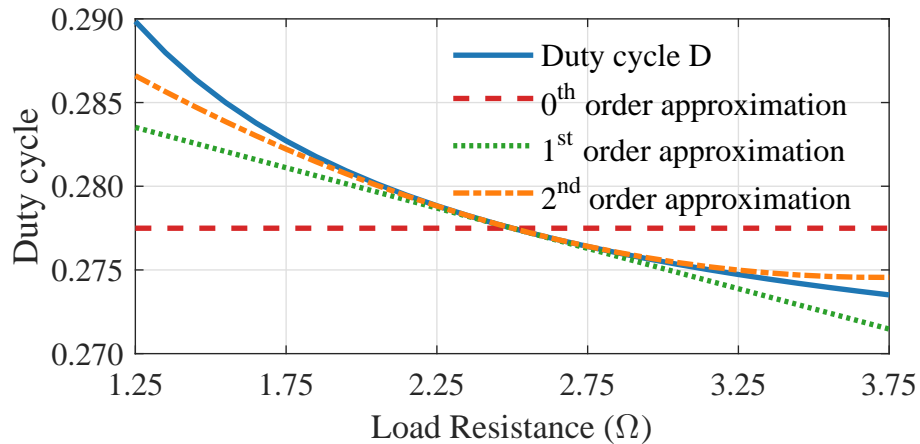


Figure 4.4: Duty cycle D as a function of load R

Although the 2nd order Taylor series provides the best approximation, as can be seen in Fig. 4.4, the 1st order approximation is used in this section of the work, not to unnecessary increase the computational complexity.

4.2.3 Controller model

The transfer functions of the compensator and modulator, shown in Fig. 4.1, can be written as (4.15) and (4.16) respectively.

$$\begin{aligned} G_c(s) &= \frac{v_{com}(s) - v_{ref}(s)}{v_{ref} - v_o(s)} \\ &= \frac{k(s + w_{z1})(s + w_{z2})}{s(s + w_{p2})(s + w_{p3})} \end{aligned} \quad (4.15)$$

$$d(s) = f_m(v_{com}(s) - v_{off}(s)) \quad (4.16)$$

$$\begin{aligned} \text{where } k &= \frac{(R_1 + R_3)}{R_1 R_3 C_3} \\ w_{z1} &= \frac{1}{C_1 R_2}, \quad w_{z2} = \frac{1}{C_2(R_1 + R_3)} \\ w_{p2} &= \frac{1}{C_2 R_3}, \quad w_{p3} = \frac{(C_1 + C_3)}{C_1 C_3 R_2} \end{aligned}$$

Based on the above transfer functions, the state equations of the small-signal ac model of the controller can be obtained as (4.17) and (4.18) respectively with state vector $\hat{x}(t)$: $[\hat{x}_5(t), \hat{x}_6(t), \hat{x}_7(t)]$, input vector $\hat{u}(t)$: $[\hat{v}_{ref}(t), \hat{v}_{off}(t)]$ and output vector $\hat{y}(t)$: $[\hat{d}(t)]$. The corresponding dc quiescent point can be derived as (4.19) and (4.20).

$$\begin{aligned}
\dot{\hat{x}}_5(t) &= -(w_{p2} + w_{p3})\hat{x}_5(t) - w_{p2}w_{p3}\hat{x}_6(t) + \hat{v}_{ref}(t) - \hat{v}_o(t) \\
\dot{\hat{x}}_6(t) &= \hat{x}_5(t) \\
\dot{\hat{x}}_7(t) &= \hat{x}_6(t)
\end{aligned} \tag{4.17}$$

$$\hat{d}(t) = m_1\hat{x}_5(t) + m_2\hat{x}_6(t) + m_3\hat{x}_7(t) + f_m\hat{v}_{ref}(t) - f_m\hat{v}_{off}(t) \tag{4.18}$$

$$\text{where } m_1 = f_mk, \quad m_2 = f_mk(w_{z1} + w_{z2}), \quad m_3 = f_mk w_{z1}w_{z2}$$

$$X_5 = 0, \quad X_6 = 0, \quad X_7 = \frac{(D - f_m V_{ref} + f_m V_{off})}{f_mk w_{z1}w_{z2}} \tag{4.19}$$

$$V_o = V_{ref} \tag{4.20}$$

4.2.4 Closed loop controlled converter model

At this point, the power stage and controller models, derived in the earlier sections, can be combined to yield the small-signal ac model of the closed loop controlled buck converter. The process involves replacing $\hat{v}_o(t)$ in (4.17) with expression (4.14) and $\hat{d}(t)$ in (4.13) with expression (4.18). The resulting state equations have combined state vector $\hat{x}(t) = [\hat{i}_g(t), \hat{v}_{cin}(t), \hat{i}_l(t), \hat{v}_c(t), \hat{x}_5(t), \hat{x}_6(t), \hat{x}_7(t)]$, input vector $\hat{u}(t) = [\hat{v}_g(t), \hat{v}_d(t), \hat{v}_{ref}(t), \hat{v}_{off}(t)]$ and output vector $\hat{y}(t) = \hat{v}_o(t)$. The state equations, when expressed in the state space matrix form $(\begin{smallmatrix} A & B \\ E & F \end{smallmatrix})$, produces the small-signal ac model of the closed-loop controlled buck converter as shown in (4.21).

It is to be added that all the elements of the developed model are rational, in symbolic form and expressed in terms of system parameters and system inputs only. The system model (4.21), referred to the linear equivalent model of the buck converter, is suited for μ analysis over a range of operating points and parameter variations.

$$\begin{array}{cccccccc}
 \frac{-(R_{cin}+R_{in})}{L_{in}} & -\frac{1}{L_{in}} & \frac{DR_{cin}}{L_{in}} & 0 & p_1m_1 & p_1m_2 & p_1m_3 & \frac{1}{L_{in}} & 0 & p_1f_m & -p_1f_m \\
 \frac{1}{C_{in}} & 0 & -\frac{D}{C_{in}} & 0 & p_2m_1 & p_2m_2 & p_2m_3 & 0 & 0 & p_2f_m & -p_2f_m \\
 \frac{DR_{cin}}{L} & \frac{D}{L} & \frac{q}{L} & -\frac{R}{L(R+R_c)} & p_3m_1 & p_3m_2 & p_3m_3 & 0 & \frac{D-1}{L} & p_3f_m & -p_3f_m \\
 0 & 0 & \frac{R}{C(R+R_c)} & -\frac{1}{C(R+R_c)} & 0 & 0 & 0 & 0 & 0 & 0 & 0 \\
 0 & 0 & -\frac{R_cR}{R_c+R} & -\frac{R}{R_c+R} & -(w_{p2}+w_{p3}) & -w_{p2}w_{p3} & 0 & 0 & 0 & 1 & 0 \\
 0 & 0 & 0 & 0 & 1 & 0 & 0 & 0 & 0 & 0 & 0 \\
 0 & 0 & 0 & 0 & 0 & 1 & 0 & 0 & 0 & 0 & 0 \\
 0 & 0 & \frac{R_cR}{R_c+R} & \frac{R}{R_c+R} & 0 & 0 & 0 & 0 & 0 & 0 & 0
 \end{array}$$

(4.21)

4.3 Model refinement

In this section, the small-signal ac circuit of the buck converter in Fig. 4.1, built in Simulink[®] environment, is verified and validated. The objective is to obtain a refined model that can predict the behaviour of the power system such as borderline stability with fairly good accuracy. The procedure for refining the system model is depicted in Fig. 4.5. The process has required the use of a network analyser to experimentally measure certain small-signal transfer functions of the system under study, as described in appendix B [13],[63].

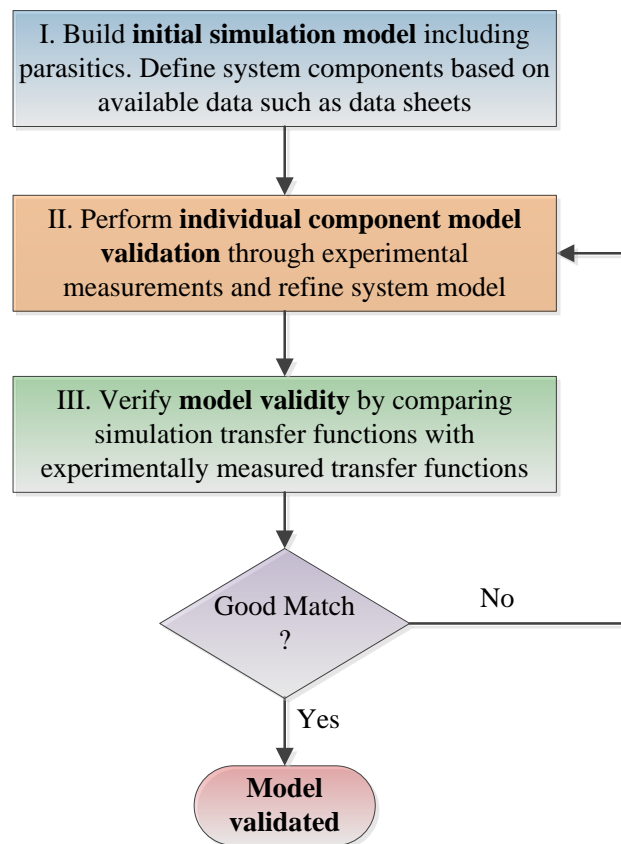


Figure 4.5: System model refinement procedure

4.3.1 Initial simulation model

The first step consists in defining the initial average model of the buck converter under study based on available data and nameplate information, as defined in Table 4.1. Many of these initial parameter values, can be further refined to increase model fidelity, as described in the following subsections.

4.3.2 Individual system components models

Thus, the second step of the process models individual system components through experimental measurements. It has been shown that non-idealities such as parasitic resistances in wiring and power supply, the equivalent series resistance (ESR) of the capacitors and inductors as well as, the voltage drop in the diode and the on-resistance of the switch transistor have significant impact on the accuracy of the model. The experimental measurements for a few system components are described below.

The output impedance of the power supply has been measured when connected to different loads and set to different voltages, as shown in Fig. 4.6. A network analyser has been employed to obtain the dynamic measurements [13],[63]. The best estimate of the experimental measurements of the power supply impedance, through curve fitting, are found to be $47e^{-3} + s1.8^{-6}$. From these measurements, the equivalent series resistance (ESR) and inductance of the power supply are estimated as $47\text{ m}\Omega$ and 1.8 mH respectively.

The input filter inductance and capacitance have been measured by means of an impedance analyser. The measurements are depicted in Figs. 4.7 and 4.8, respectively. After deducting the resistance of the cables used for the measurements, of $70\text{ m}\Omega$, the filter inductance and ESR are estimated as $510\text{ }\mu\text{H}$ and $60\text{ m}\Omega$, respectively. The input filter capacitance and ESR are estimated as $95\text{ }\mu\text{F}$ and $95\text{ m}\Omega$ respectively. It is to be noted that although second order polynomials provide better approximations, especially at high frequencies, the first order approximation has been

selected as it provides sufficient accuracy to the parameter model without unnecessarily complicating the model.

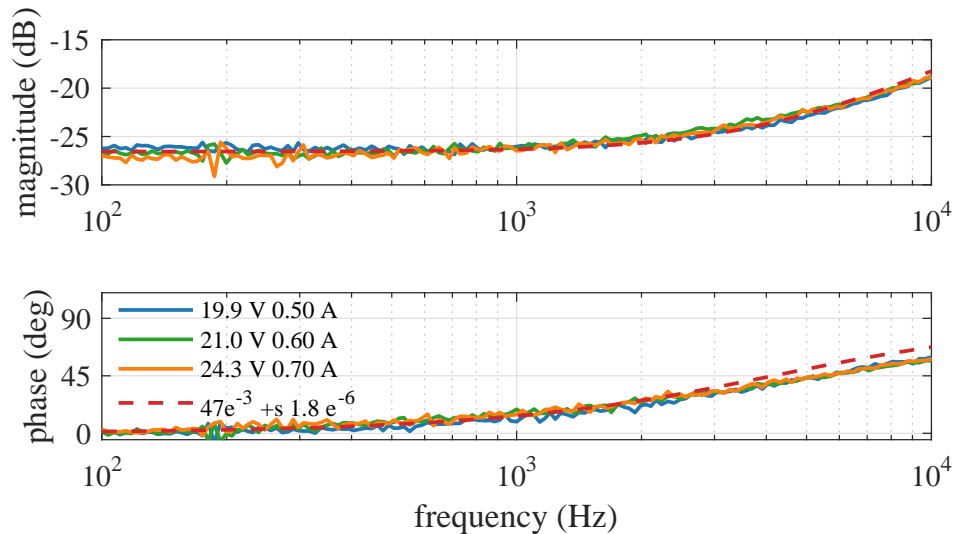


Figure 4.6: Output impedance of power supply estimated through curve fitting of experimental measurements

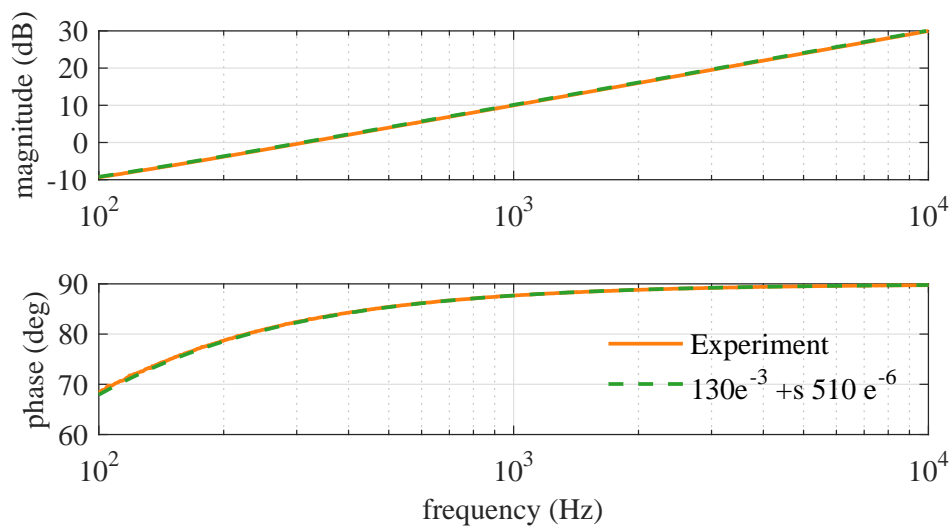


Figure 4.7: Input filter inductance including measuring cable resistance estimated through curve fitting of experimental measurements

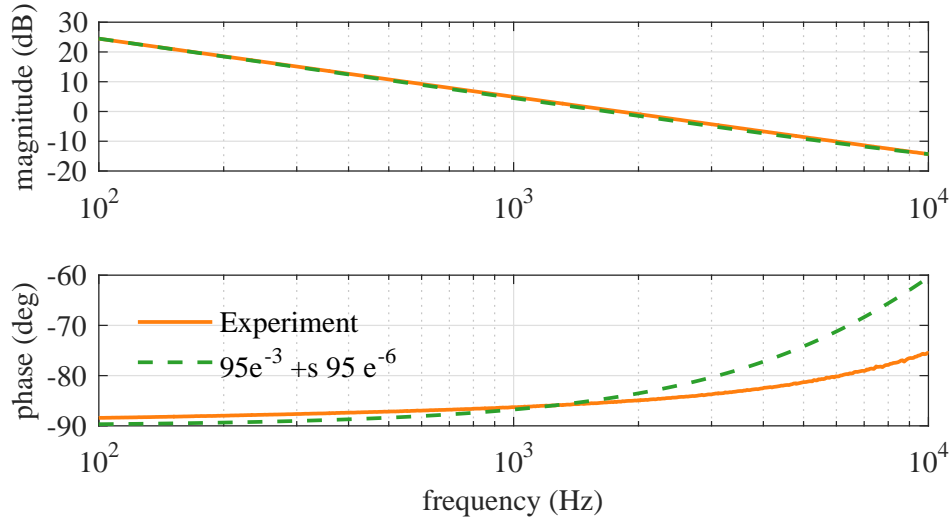


Figure 4.8: Input filter capacitance estimated through curve fitting of experimental measurements

4.3.3 Refined system model

The last step consists first of experimentally measuring the converter transfer functions, such as the loop gain T , the input impedance Z_i and the output impedance Z_o , by means of a network analyser [13],[63]. The experimental measurements are then compared with the corresponding transfer functions obtained from the simulation model. The individual component model and the system model are refined and adjusted iteratively until a good match is obtained.

Fig. 4.9 and 4.10 depict the loop gain and the input impedance of the converter obtained from both experiments and the updated simulation model. These measurements have been made without the input filter inductor and with a load of $R = 1.6 \Omega$. The simulation model transfer functions match the experimentally observed behaviour of the converter to good accuracy.

Through the process of model refinement, the initial values of the system components

have been fine-tuned to their final values, as given in Table 4.2. The refined simulation model is used for μ analysis of the ensuing case studies.

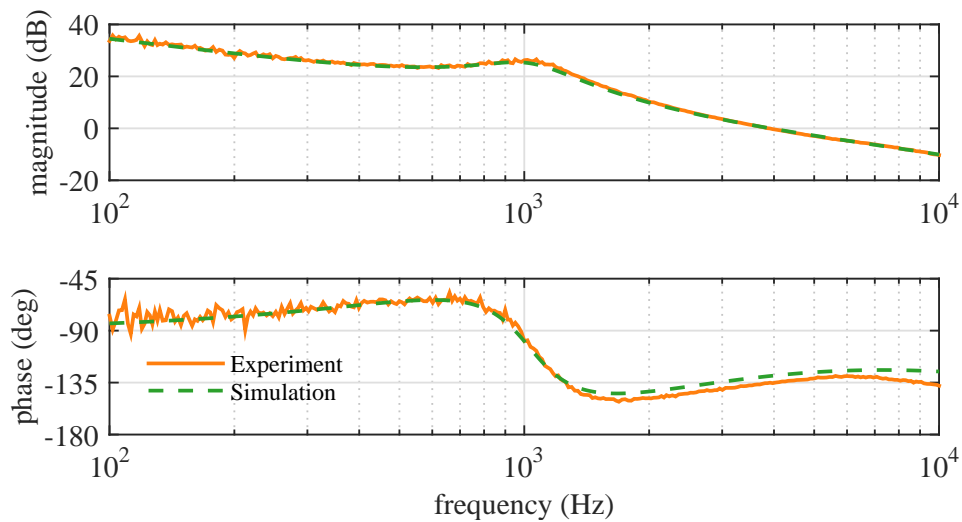


Figure 4.9: Validation of simulation model loop gain against experimental measurements of loop gain

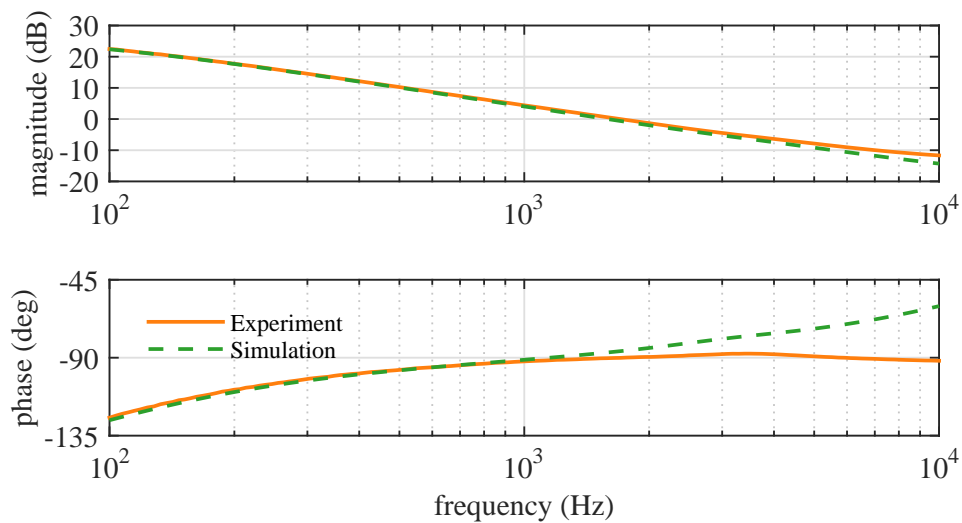


Figure 4.10: Validation of simulation model input impedance against experimental measurements of input impedance

Table 4.2: Initial and measured values for the system parameters

Symbol	Units	Initial Values	Measured Values	Description
v_g	V	19.8	19.8	DC source voltage
v_{ref}	V	5.1	5.1	Reference Voltage
v_d	V	0.22	-	Diode Voltage
v_{off}	V	2.352	2.3252	Offset Voltage
f_s	kHz	51.0	51.2	Switching frequency
f_m	-	0.284	0.284	Modulator gain
R	Ω	2.50	2.50	Load resistance
R_{on}	$m\Omega$	160	-	Switch on resistance
R_d	$m\Omega$	12	-	Diode on resistance
R_{in}	$m\Omega$	100	160	Input Resistance
L_{in}	μH	500	511.8	Input filter inductance
C_{in}	μF	100	95	Input filter capacitance
R_{cin}	$m\Omega$	47	95	ESR of input filter capacitor
L	μH	42	45.5	Output filter inductance
R_l	$m\Omega$	45	50	ESR of output filter inductor
C	μF	590	540	Output filter capacitance
R_c	$m\Omega$	10	17	ESR of output filter capacitor
R_1	$k\Omega$	20.0	19.9	Resistance in compensator
R_2	$k\Omega$	20.0	19.7	Resistance in compensator
R_3	$k\Omega$	2.0	2.0	Resistance in compensator
C_1	nF	8.22	8.22	Capacitance in compensator
C_2	nF	4.72	4.72	Capacitance in compensator
C_3	nF	0.331	0.331	Capacitance in compensator

4.4 Load uncertainty

In this section, μ analysis is applied to determine the critical resistive load R that destabilises the system shown in Fig. 4.1. In this analysis, the only varying parameter is load R that can vary around its nominal value by $\pm 50\%$ (i.e $R_{var} = \pm 50\%$ as defined in (4.22) to (4.24) and Table 4.3. The other system parameters are assumed to be constant with nominal values given in Table 4.1.

Table 4.3: Uncertain resistive load

Parameter	Nominal Value (R_o)	Range of variation (R_{var}) with respect to nominal value
Load Resistance (R)	2.5Ω	± 50 %

4.4.1 μ analysis

Prior to μ analysis, the state space model (4.21) is converted in its LFT form. In this work, Matlab[®] Robust Stability Toolbox has been employed for performing both LFT and SSV analysis. Expressing (4.21) in the $M\Delta$ form requires that all uncertain parameters be firstly converted in their LFT forms. In order to represent uncertain element R in an equivalent LFT form, it has to be expressed as a function of its normalised form δ_R which lies between -1 and 1 as shown in (4.22). R_o and R_{var} can be derived from the minimum value (R_{min}) and the maximum value (R_{max}) of the resistive load as shown in (4.23) and (4.24) [53].

$$R = R_o + R_o R_{var} \delta_R \quad \text{where } \delta_R \in [-1, 1] \quad (4.22)$$

$$R_o = (R_{max} + R_{min})/2 \quad (4.23)$$

$$R_{var} = (R_{max} - R_{min})/(R_{max} + R_{min}) \quad (4.24)$$

The normalised parameters δ_R are then extracted from the uncertain system model (4.21) and grouped in a diagonal matrix in a feedback form by applying LFT technique. The resulting uncertainty matrix is shown in (4.25). δ_R appears 227 times in the Δ matrix which corresponds to the number of times R appears in the system matrix.

$$\Delta(2\pi f) = \delta_R I_{227 \times 227} \quad (4.25)$$

μ analysis is then applied to the obtained uncertain system model in $M\Delta$ form by using Matlab[®] Robust Stability Toolbox. The results are shown in Fig. 4.11a and 4.11b.

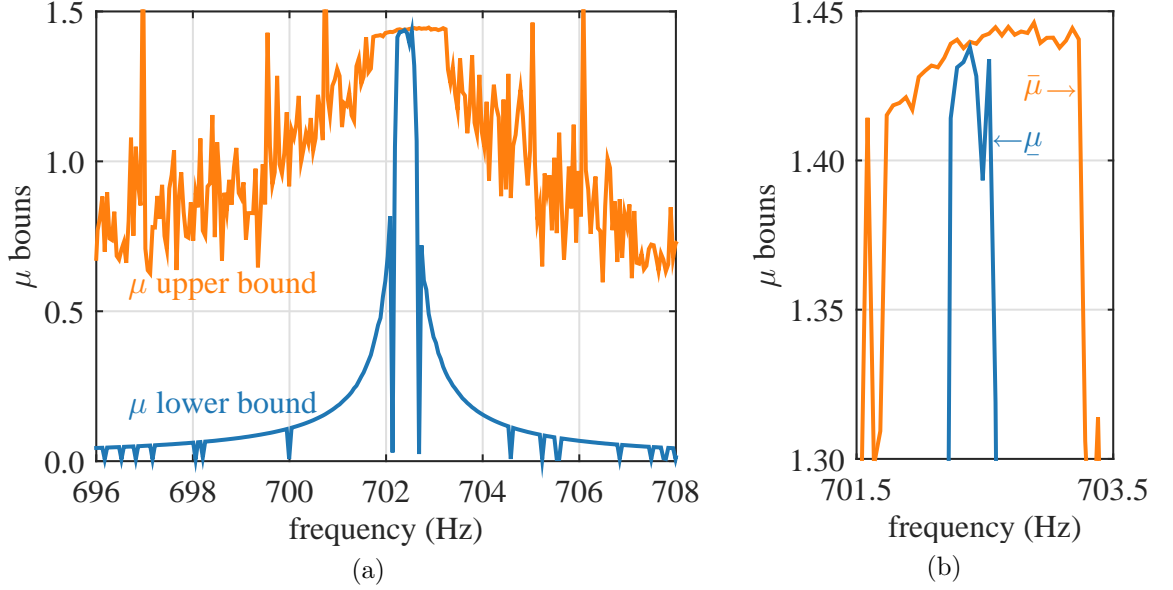


Figure 4.11: System with load uncertainty (a) μ chart to predict critical R (b) zoomed area near peak of μ chart

For this test, $\mu = 1.44$ as given by the peak value of the charts in Fig. 4.11a and 4.11b. The smallest destabilising matrix, of size 227×227 as given by (4.26), gives the robust stability margin ($1/\mu$) as 0.696 [38].

$$\Delta(j2\pi 702.4) = -0.696 I_{227 \times 227} \quad (4.26)$$

By comparing (4.26) with (4.25), it can be noted that $\delta_R = -0.696$. The critical destabilising load can be computed from $\delta_R = -0.696$ and (4.22) and is equal to 1.63Ω or $15.96 W$, as shown in (4.27) and Table 4.4.

$$\begin{aligned} R &= R_o + R_o R_{var} \delta_R \quad \text{where } \delta_R \in [-1, 1] \\ &= 2.5 + 2.5 \times 50\% \times (-0.696) \\ &= 2.5 - 2.5 \times 35\% = 1.63 \end{aligned} \quad (4.27)$$

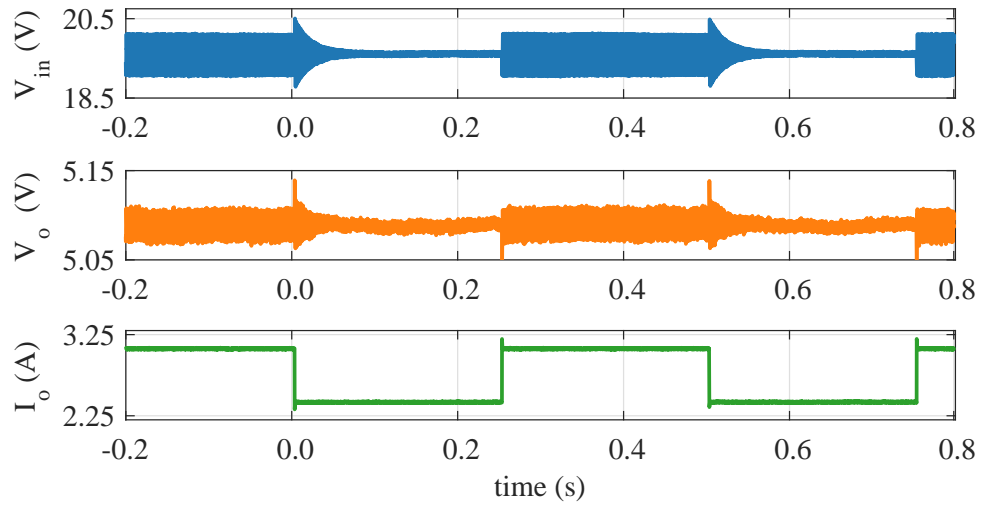
Table 4.4: System with load uncertainty - μ analysis results

Perturbation matrix	Robust stability margin	$\underline{\mu}$	Critical R	Critical P_o
$\Delta(j2\pi702.4)$	0.696	1.44	1.63 Ω	16.0 W

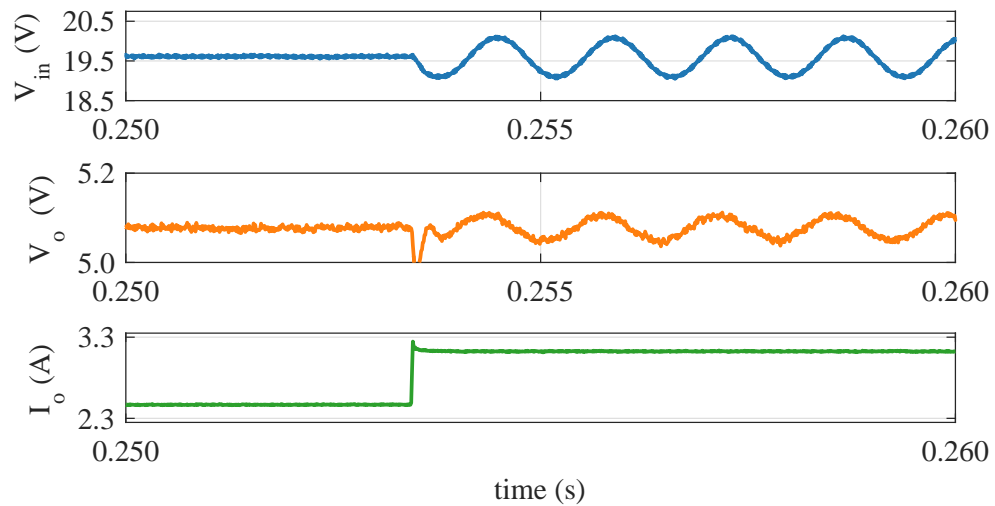
$\mu > 1$ indicates that the system is not robustly stable, i.e. the system does not remain stable over the whole uncertainty range between 1.25 Ω and 3.75 Ω , as defined in Table 4.3. In order to ensure that the system remains robustly stable, μ should be less than 1. This can be achieved by scaling the operating range of the system load by $1/\mu$, the robust stability margin, as discussed in chapter 2. The new uncertainty range of R needs to be reduced by $2.5 \pm 2.5 \times 50\% \times 0.696$ i.e. $2.5 \Omega \pm 35\%$. This is in accordance with the hypercube concept, from which it can be inferred that, the buck converter remains robustly stable within a line segment of coordinate size $1/\mu = 0.696$, as shown in Fig 3.7 in chapter 3. The line segment gives a maximum range in R of [1.63 Ω , 3.37 Ω], as can be computed from (4.27), for a robustly stable system. It is equivalent to a largest uncertainty range in output power P of [7 W, 16 W] based on the output voltage of 5.1 V. Although it can be argued that the system may remain stable below the lower limit of 7 W, it is evident that the upper limit of 16 W gives the critical destabilising value of the output power. This information can be obtained and confirmed from (4.26) and (4.27).

4.4.2 Experimental results in time domain

In this experiment, the electronic resistive load R was decreased in small steps from a peak value of 2 Ω until the system reached boundary stability. When R was decreased to 1.62 Ω at $t = 0.253$ s (i.e. I_o increased to 3.15 A), the system reached the boundary condition of stability, as can be seen in Fig. 4.12a and 4.12b. This is shown by the sustained oscillations in v_{in} and v_o in Fig. 4.12a and 4.12b. When R was increased back to 2 Ω at $t = 0.503$ s (i.e. I_o decreased to 2.55 A), the system stabilised again, as shown in Fig. 4.12a. The critical load resistance of 1.62 Ω closely matches the value of 1.63 Ω predicted by μ analysis, as depicted in Table 4.5.



(a)



(b)

Figure 4.12: Experimental results for system with load uncertainty (a) system is at boundary of stability with $R = 1.63 \Omega$ from $t = 0.253 \text{ s} - 0.503 \text{ s}$ (b) zoomed area near $t = 0.253 \text{ s}$

Table 4.5: System with load uncertainty - μ analysis and experimental results

Parameter	μ analysis	Experimental
Load resistance (Ω)	1.63 Ω	1.62 Ω
Power (P_o)	16.0 W	16.1 W

4.4.3 Experimental results in frequency domain

The aim of this part of the work is two-fold. First, it evaluates the feasibility of applying impedance-based stability analysis to the buck converter in experiment, so as to determine the destabilising system load. Secondly, it verifies the μ predictions, obtained in section 4.4.

Considering two subsystems connected in series, with F_A and F_B being the transfer functions of the source and load subsystems respectively, the transfer function of the whole system can be derived as (4.28) [14],[66].

$$F_{AB} = \frac{F_A F_B}{1 + T}, \quad \text{with} \quad T = \frac{Z_o}{Z_i} = \frac{|Z_o|}{|Z_i|} \angle(\phi_{Z_o} - \phi_{Z_i}) \quad (4.28)$$

The impedance ratio of the source impedance Z_o to the load impedance Z_i is referred to as the minor loop gain T as given by (4.28). For a system to be stable, the minor loop gain must satisfy the Nyquist stability criterion, i.e, $1 + T$ must not have any roots in the right half plane [14].

The sufficient condition of Middlebrook criterion, which is an extension of the aforementioned formal requirement of the Nyquist stability criterion, requires that $|Z_o| \ll |Z_i|$ for all frequencies, to ensure system stability [14],[66]. The Middlebrook criterion, is normally applied at the input filter/converter interface at point Y , as shown in Fig. 4.1 and 4.2. At the interface Y , Z_o has a resonant point since it includes the LC filter. A practical way to verify that the system is stable is to ensure that the peak of $|Z_o|$ is less than $|Z_i|$, as was discussed in the thesis introduction. The application of Middlebrook criterion to the buck converter in Fig. 4.1 required the

experimental measurement of Z_i at point Y . This involves the series connection of an injection circuit from the network analyser at that point, as shown in Fig. B.1 and B.2 in appendix B. However, since the input filter capacitor C_{in} was part of the PC board of the buck converter, as shown in Fig. 4.2, there were no connection points available for signal injection between C_{in} and the mosfet at point Y . Hence, it was not practically possible to apply the sufficient condition of the Middlebrook criterion.

Nevertheless, it was feasible to measure the system impedances at point X of the buck converter, as shown in Fig. 4.1 and 4.2. The point X is the input to the buck converter, which includes the input filter capacitor. The injection circuit could be connected at that point, by disconnecting the input filter inductor from the converter at that interface. Hence, the aim was to apply Nyquist criterion to the minor loop gain T at point X to determine system stability. The methodology involved firstly measuring Z_o at point X . The measurements were made by means of a network analyser, over a frequency range between 100 Hz and 50 kHz [13]. A set of measurements of Z_i was then made with different loads R connected to the converter, ranging from 1 Ω to 6 Ω . In order to measure Z_i , with R set below its critical value, without causing the system to become unstable, the measurements were made with the input filter inductor disconnected from the circuit. The output impedance Z_o was measured separately, with the power supply and inductor connected to a dummy load.

The set of experimentally measured Z_o/Z_i is analysed to identify the critical value of R , which causes the system to reach the boundary of stability. According to the Nyquist stability criterion as applied to T in (4.28), when the gain margin $|Z_o/Z_i| = 1$, the phase difference $(\phi_{Z_o} - \phi_{Z_i})$ must be equal to 180° , for the system to be at the boundary of stability. The experimental measurements of Z_i with R set at 1.02 Ω , 1.62 Ω and 5.37 Ω are depicted in Fig. 4.13 and Fig. 4.14, together with the measurements of Z_o .

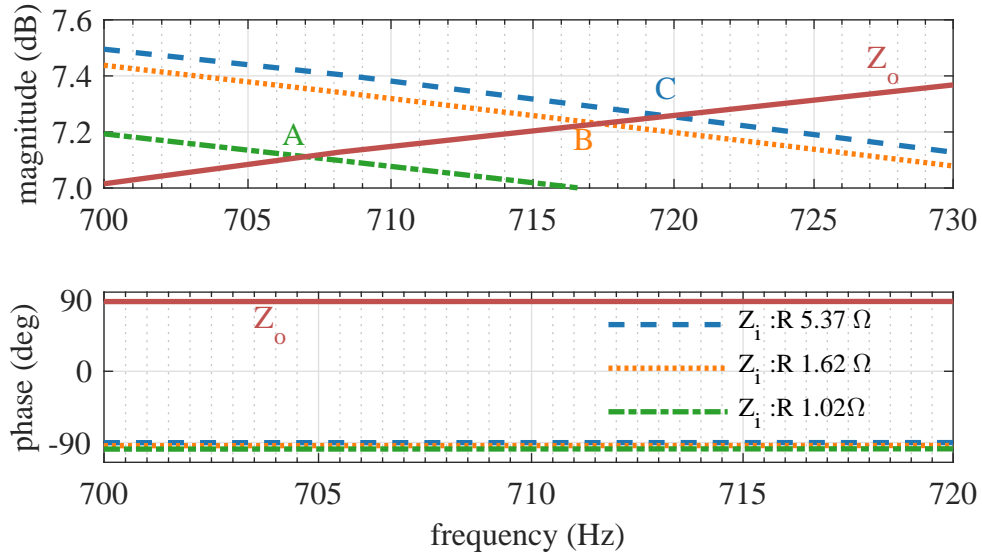


Figure 4.13: Experimental measurements of Z_o and Z_i at point X of buck converter for system with load uncertainty (i) at point C , system is stable with $R = 5.37 \Omega$ (ii) at point B , system is near boundary stability with $R = 1.62 \Omega$ (iii) at point A , system is unstable with $R = 1.02 \Omega$

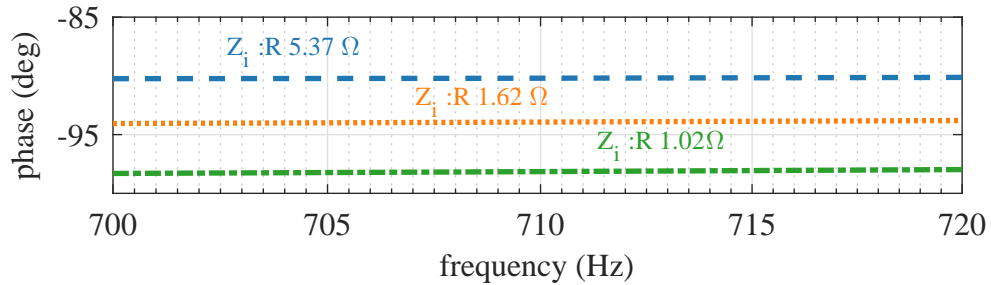


Figure 4.14: Zoomed view of the phase of the input impedance in Fig. 4.13

The phase difference ($\phi_{Z_o} - \phi_{Z_i}$) at points A , B and C where $|Z_o| = |Z_i|$ are given in Table 4.6. It is noted from Table 4.6 that, with R equal to 1.62Ω , the phase difference is close to 180° . This corresponds to the μ prediction of 1.63Ω , obtained in section 4.4. For the stable case, with R equal to 5.37Ω , the phase difference is slightly less than 180° while for the unstable case, with R equal to 1.02Ω , the phase difference exceeds 180° .

Table 4.6: System with load uncertainty - Experimental measurements of Z_o and Z_i

Points	R	Magnitude $ Z_i = Z_o $	Phase Z_i ϕ_i	Phase Z_o ϕ_o	Phase difference $(\phi_o - \phi_i)$
C	5.37 Ω	7.3 dB	-90.13°	88.20°	178.33°
B	1.62 Ω	7.2 dB	-93.84°	88.18°	182.02°
A	1.02 Ω	7.1 dB	-98.20°	88.11°	186.31°

Further, Nyquist charts of the experimentally measured Z_o/Z_i have been plotted for the aforementioned cases. For the stable case, with R equal to 5.37 Ω , the Nyquist plot does not enclose the point (-1,0) as depicted in Fig. 4.15a. For the unstable case, with R equal to 1.02 Ω , the Nyquist plot encloses the point (-1,0) as depicted in Fig. 4.15b. With R equal to 1.62 Ω , the Nyquist plot encloses the point (-1,0) rather than going through it, as shown in Fig. 4.15c and 4.15d. This is expected as the phase difference of the measured impedances is 182° and not 180° at that point, as shown in Table 4.6. Nevertheless, it is to be noted that the point at which the curve crosses the real axis, and which corresponds to the phase difference of 180°, is closer to the critical point (-1,0) for R equal to 1.62 Ω , as compared to when R is 1.02 Ω .

It should be noted that identifying the critical destabilising load experimentally, by using the impedance-based method, posed a few difficulties. First, the phase difference of the impedances are very close to 180°, for a wide range of loads. In addition, there are possible measurement errors that may arise due to the disconnection of the input filter inductor from the circuit, during the experiment. This may further compromise the accuracy of the results.

4.4.4 Simulation time

In order to assess the effect of the duty cycle approximation on robust stability margin and simulation time, μ analysis has also been performed by using the first order approximation of the duty cycle D . The results are given in Table 4.7. The first order approximation introduces an error of 7% in the robust stability margin and an

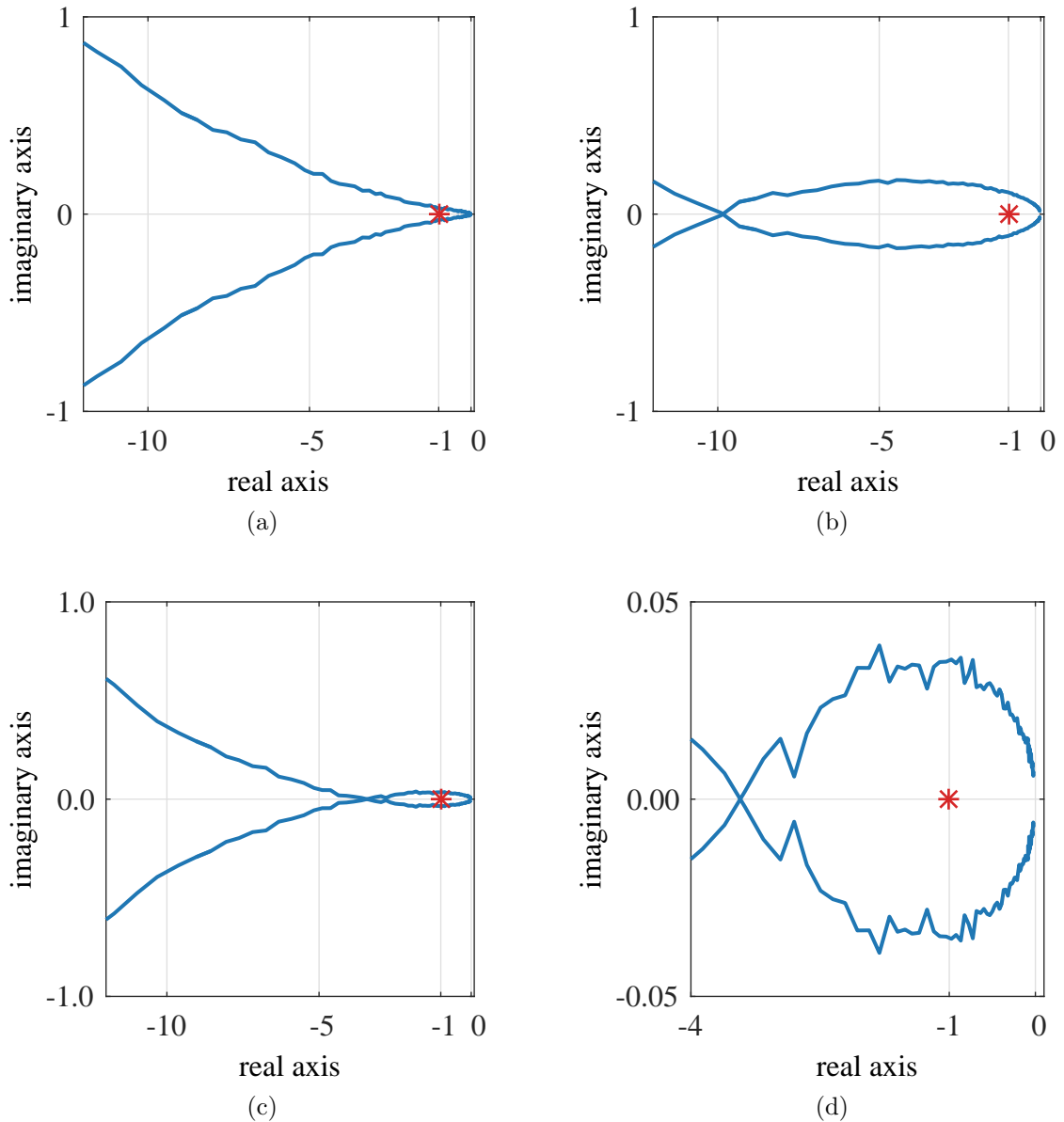


Figure 4.15: Nyquist plots of experimentally measured Z_o/Z_i for system with load uncertainty at point X of buck converter (a) system is stable with $R = 5.37 \Omega$ (b) system is unstable with $R = 1.02 \Omega$ (c) system is near boundary stability with $R = 1.62 \Omega$ (d) zoomed view of Fig. 4.15c

error of 4% in the critical R , with respect to the second order approximation. In spite of the loss in accuracy, the simulation time is seen to reduce considerably, as noted in Table 4.7. This is due to the fact that D appears 189 times in the system model. By setting D as a constant, the size of the uncertainty matrix reduces from 227×227 to 37×37 . It can be inferred that the size of the uncertainty matrix has a key influence on computational cost. Of note is that non-linear terms can be treated as uncertain elements of the system, as will be examined in a later section.

Table 4.7: System with load and model uncertainties - Evaluation of polynomial approximations of D

D approximation	Robust stability margin	Critical R	Size $\Delta(jw)$	Simulation time
2nd order	0.696	1.63 Ω	227×227	2.6 <i>hrs</i>
1st order	0.745	1.57 Ω	37×37	4 <i>mins</i>

4.5 Source impedance uncertainty

At design stage, the power source to which a converter is to be connected, may not be known. Yet, the source impedance may influence the stability of an EPS to a great extent. Hence, this section investigates the impact of source impedance uncertainty on system stability. The robust stability margin of the buck converter is examined, when it is subject to load uncertainty as shown in Table 4.3, for different values of line resistance R_{in} . In the first case (I), R_{in} is set to 185 $m\Omega$ and in the second case (II), R_{in} is set to 278 $m\Omega$. The μ approach is applied to (4.21), based on the methodology described in section 4.4. Experimental validation is provided.

4.5.1 μ analysis

The μ charts for cases I and II are shown in Figs. 4.16a - 4.16b, and 4.17a - 4.17b respectively.

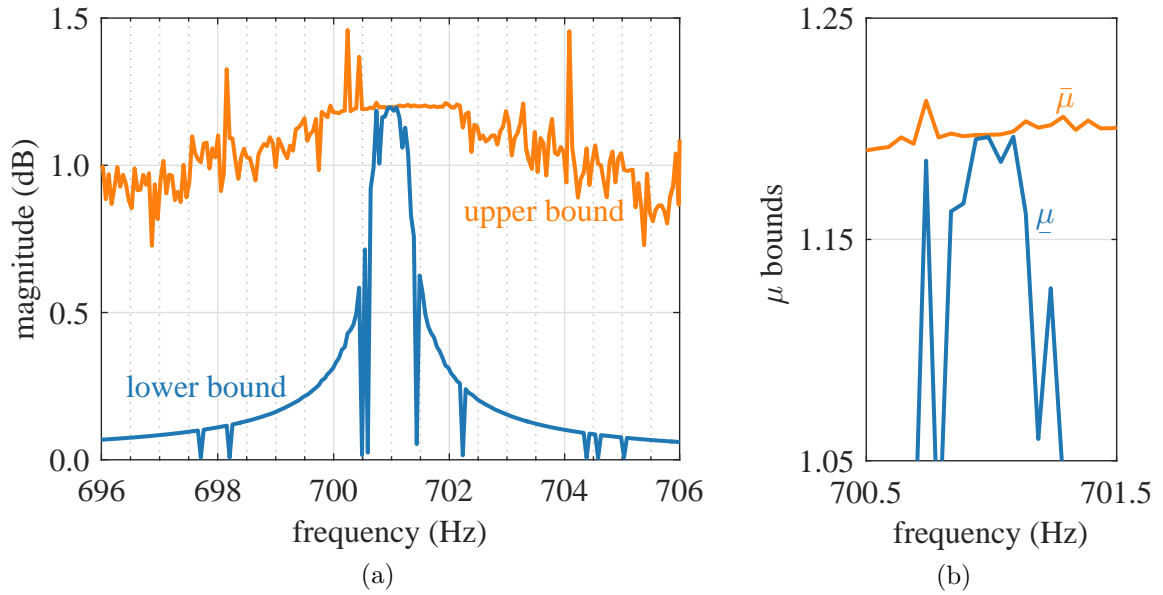


Figure 4.16: System with uncertain load and $R_{in} = 185 \text{ m}\Omega$ (a) μ chart to predict critical R (b) zoomed area near peak of μ chart

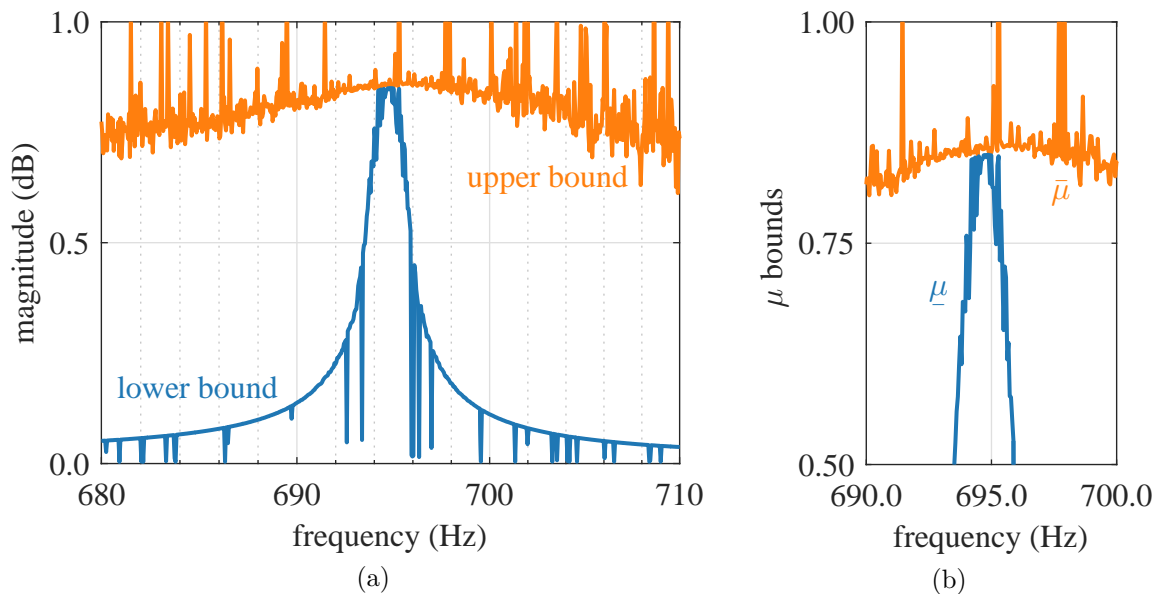


Figure 4.17: System with uncertain load and $R_{in} = 278 \text{ m}\Omega$ (a) μ chart to predict critical R (b) zoomed area near peak of μ chart

The associated robust stability margin, obtained from μ analysis, are given in Table 4.8. In addition, the μ predictions and experimental results, with R_{in} set to $160\text{ m}\Omega$, as determined in section 4.4, are also included in Table 4.8 for completion.

Table 4.8: System with uncertain load and different R_{in} - μ analysis results

R_{in}	μ	Robust stability margin	Critical R μ analysis	Critical P_o μ analysis
160 m Ω	1.44	0.696	1.63 Ω	16.0 W
185 m Ω	1.20	0.835	1.46 Ω	17.8 W
278 m Ω	0.85	1.180	1.03 Ω	25.3 W

4.5.2 Experimental results

During the experiment, the line resistance of the buck converter was adjusted for the two case studies. R_{in} was first set to $185\text{ m}\Omega$ and then to $278\text{ m}\Omega$. The load R was then gradually decreased in both cases until the EPS reached boundary stability. For case I, with R_{in} set to $185\text{ m}\Omega$, the experimental results in Fig. 4.18 show that voltage V_{in} is stable when R is $1.89\text{ }\Omega$. When the load R is reduced to $1.54\text{ }\Omega$, the system reaches boundary stability, as shown by the sustained oscillation of V_{in} . Decreasing R to $1.50\text{ }\Omega$ causes the system to become unstable. For case II, with R_{in} set to $278\text{ m}\Omega$ at time $t = 0.08\text{ s}$, the buck converter reaches boundary stability when the load R is decreased to $1.17\text{ }\Omega$, as depicted in Fig. 4.19a and 4.19b. The μ results are within 12 % of the experimental results, as shown in Table 4.9. The μ predictions are acceptable, considering errors in experimental measurements and in the system model.

Table 4.9: System with uncertain load and different R_{in} - μ analysis and experimental results

R_{in}	μ	Robust stability margin	Critical R μ analysis	Critical R Experimental	Critical P_o μ analysis
160 m Ω	1.44	0.696	1.63 Ω	1.62 Ω	16.0 W
185 m Ω	1.20	0.835	1.46 Ω	1.54 Ω	17.8 W
278 m Ω	0.85	1.180	1.03 Ω	1.17 Ω	25.3 W

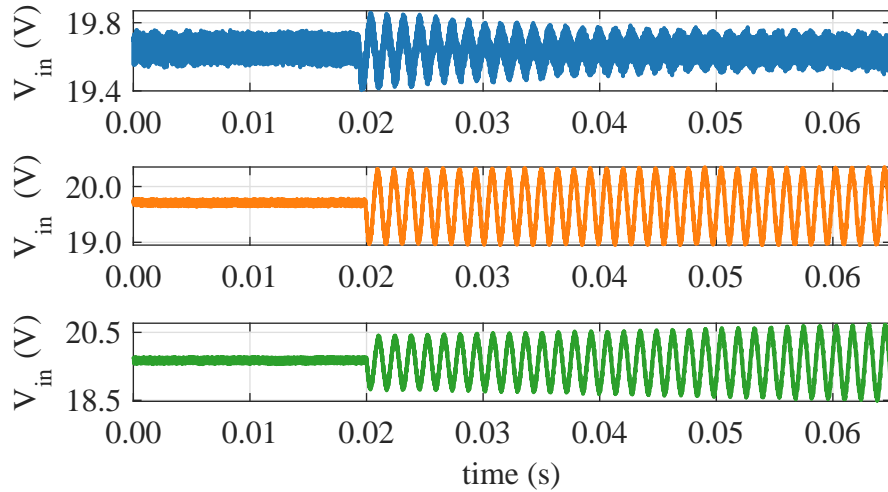


Figure 4.18: Experimental results for system with uncertain load and $R_{in} = 185 \text{ m}\Omega$ (i) top figure: system is stable with $R = 1.89 \Omega$ (ii) middle figure: system is at boundary of stability with $R = 1.54 \Omega$ (iii) bottom figure: system is unstable with $R = 1.50 \Omega$

4.5.3 Results analysis

As can be seen from Table 4.9, the robust stability margin increases as the source resistance increases. Hence, by providing damping to the system, R_{in} has a stabilising effect on the buck converter. Supposing the nominal R_{in} is $278 \text{ m}\Omega$, it will be considered safe to operate the buck converter with an output power up to 25.3 W , as shown in Table 4.9. However, if the actual R_{in} is $160 \text{ m}\Omega$, the system will become unstable when the power is increased up to 16 W only. In fact, the actual robust stability margin is 69.6% , as compared to the optimistic value of 118% based on the nominal value of R_{in} of $278 \text{ m}\Omega$, as given in Table 4.9. This analysis clearly demonstrates that variation in the source impedance has a great impact on robust stability margin and must, therefore, be accounted for in stability assessment of an EPS.

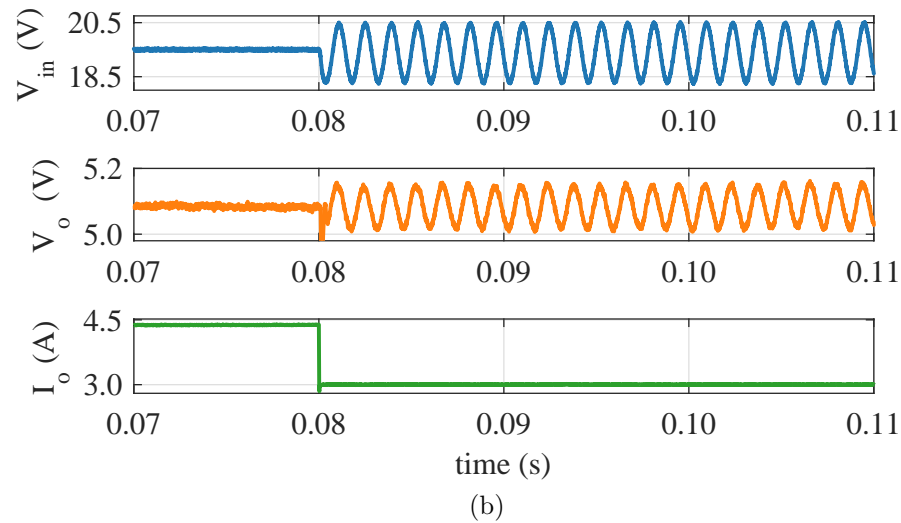
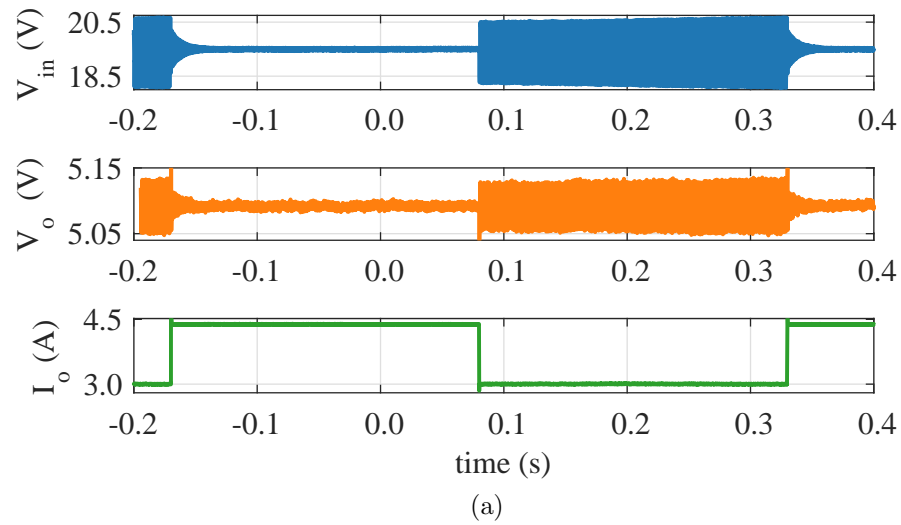


Figure 4.19: Experimental results for system with uncertain load and $R_{in} = 278 \text{ m}\Omega$
(a) system is at boundary of stability with $R = 1.17 \Omega$ at $t = 0.08 \text{ s}$ (b) zoomed area near $t = 0.08 \text{ s}$

4.6 Temperature uncertainty

Although, an EPS can be modelled to good accuracy, however, in practice, the values of its system components are bound to vary during operation. Temperature is one of the main factors that can introduce uncertainties in multiple system parameters. This section investigates the effect of extreme temperature variation on the robust stability margin of the buck converter, shown in Fig. 4.1. The μ approach is applied based on the methodology used in 4.4. The duty cycle D is estimated by its first order approximation.

4.6.1 Uncertain parameters

For this case study, the buck converter is considered to be working in an environment where the temperature may vary between $-40\text{ }^{\circ}\text{C}$ and $80\text{ }^{\circ}\text{C}$ with a reference value of $20\text{ }^{\circ}\text{C}$, as shown in Table 4.10.

Table 4.10: Uncertainties in temperature and resistive components

Parameter	Nominal Value	Range of variation with respect to nominal value
Temperature (T)	$T_o=20^{\circ}\text{C}$	$\Delta T=\pm 60^{\circ}\text{C}$
Resistive components (R_{es})	R_{eso}	$R_{esvar}=\alpha \Delta T =\pm 24\%$

The variations in temperature will influence the characteristics of the resistive components of the buck converter, which include but are not limited to the system parasitics and cable resistances. These components, which are denoted as R_{es} further in the text, comprise R_{in} , R_{cin} , R_l , R_{on} , R_c . It is assumed that a temperature coefficient of resistance (α) is $0.004\text{ }/^{\circ}\text{C}$. From (4.29) and Table 4.10, it can be seen that the variations in temperature of $\pm 60\text{ }^{\circ}\text{C}$ cause variations in the resistive components of $\pm 24\%$ around their nominal values denoted as R_{eso} .

$$R_{esvar} = (R_{es} - R_{eso})/R_{eso} = \alpha \Delta T \quad (4.29)$$

The nominal values of the system components, including R_{es} , are given in Table 4.1. It is assumed that the resistive load varies within $\pm 50\%$ of its nominal value, as shown in Table 4.3 in section 4.4. The μ approach is applied to study the effect of the defined temperature variation on stability robustness of the EPS.

4.6.2 μ analysis

By employing the LFT technique, the system model (4.21) is firstly expressed in the LFT form. The structure of the resulting uncertainty matrix is shown in (4.30).

$$\Delta(j2\pi f) = \text{diag}(\delta_R I_{41}, \delta_{Rc} I_{13}, \delta_{Rcin} I_{38}, \delta_{Rin} I_{25}, \delta_{Rl} I_{23}, \delta_{Ron} I_{27}) \quad (4.30)$$

The μ approach is then applied to the uncertain system model in its LFT form. The μ chart is depicted in Fig. 4.20 where the peak μ lower bound is seen to be equal to 1.98 at the critical frequency of 704 Hz.

The corresponding critical values of the resistive load and resistive components, calculated from the μ bounds, are given in Table 4.12. The critical destabilising load is now 1.87 Ω , based on the μ lower bound. This represents a robust stability margin of 50.5%, as shown in Table 4.11.

Table 4.11: System with temperature uncertainty - μ analysis results

Parameters	Robust stability margin	$\underline{\mu}$	Critical R	Critical P_o
R_{es}	0.505	1.98	1.87 Ω	13.9 W

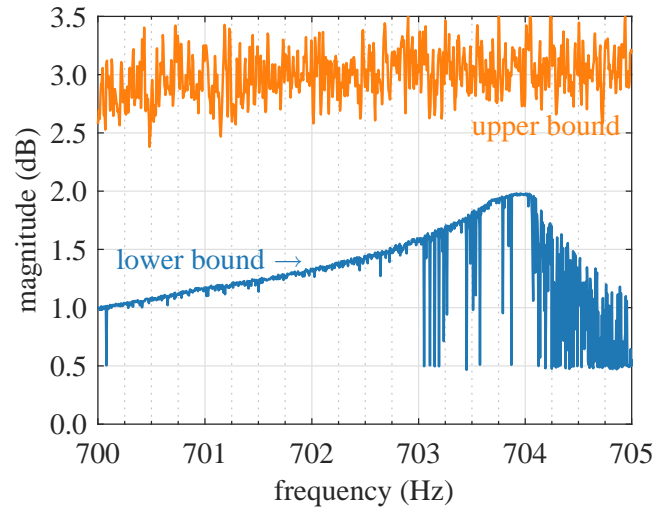


Figure 4.20: System with temperature and load uncertainties - μ chart to predict critical resistive components R_{es} and load R

4.6.3 Simulation verification

When the critical values predicted by μ analysis, as given in Table 4.12, are input in the Simulink[®] model of the buck converter, the system reaches boundary stability. Fig. 4.21a and 4.21b show the results for the case where the load R is varied with the other R_{es} components fixed at their critical values given in Table 4.12.

When R is set to be 10% higher than its critical value of 1.87Ω at $t = 0.1 s$ (I_o is $2.48 A$), the system stabilises as shown in Fig. 4.21a. When R is decreased to the critical value of 1.87Ω at $t = 0.2 s$ (I_o is $2.73 A$), the system reaches boundary stability condition, as can be seen from the sustained oscillations in v_o in Fig. 4.21a and 4.21b. When R is decreased by a further 10% below 1.87Ω at $t = 0.3 s$ (I_o is $3.03 A$), the system becomes unstable. The simulation results closely match the results predicted by μ analysis as shown in Table 4.12.

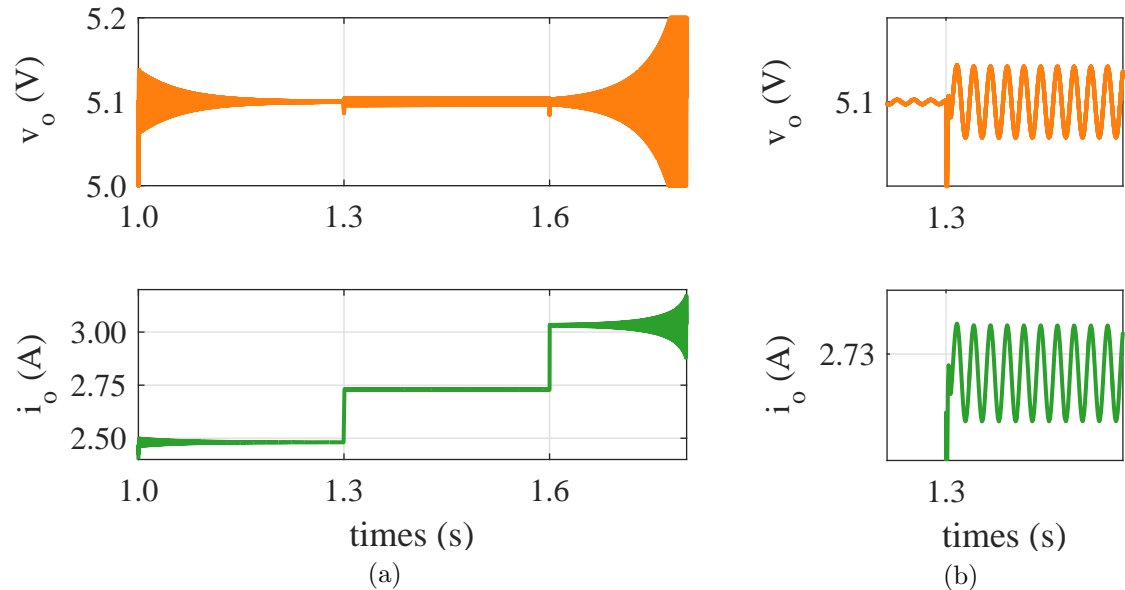


Figure 4.21: System with temperature and load uncertainties (a) top figure - voltage v_o , bottom figure - current i_o (i) at $t = 1.0$ s, $R = 1.1 \times 1.87 \Omega$ (ii) at $t = 1.3$ s, $R = 1.87 \Omega$ (iii) at $t = 1.6$ s, $R = 0.9 \times 1.87 \Omega$, where $R = 1.87 \Omega$ is the critical load predicted by μ analysis (b) zoomed area near $t = 1.3$ s

4.6.4 Results analysis

From robust stability analysis, $\mu > 1$ indicates that the EPS, with 50 % load uncertainty, is not guaranteed to remain stable over the whole range of variation of temperature (i.e. -40 °C to 80 °C). Based on the examination of the hypercube concept in Chapter 3, the buck converter system under study will remain robustly stable within a hypercube of 6^{th} dimension, of coordinate size $1/\mu = 0.505$, and centred about the nominal point. The size of the hypercube in terms of actual parameter values correspond to the μ based predictions given in Table 4.12. Any combination of parameter values chosen within the aforementioned hypercube will ensure the robust stability of the buck converter under study, within the range of temperature variation defined in Table 4.10.

Further, as depicted in Table 4.13, when the uncertainty in temperature is considered, the robust stability margin is 50.5%, as compared to 74.5% when temperature vari-

ation is neglected. This represents a 32% decrease in the robust stability margin, as shown in Table 4.13. This study confirms that the variation in temperature can have a significant influence on robust stability margin and must therefore be incorporated in the stability assessment of an EPS.

Table 4.12: System with temperature uncertainties - μ analysis and time domain simulation results

Parameters	Nominal Value	Critical Value	
		μ lower bound	Simulation
R (Ω)	2.50	1.87	1.87
R_c ($m\Omega$)	17	14.9	14.9
R_{cin} ($m\Omega$)	95	83.5	83.5
R_{in} ($m\Omega$)	160	140.6	140.6
R_l ($m\Omega$)	50	43.9	43.9
R_{on} ($m\Omega$)	160	154.7	154.7

Table 4.13: Effect of temperature on stability margin with D constant

Temperature effect considered	No	Yes
Critical Load Resistance (R)	1.57 Ω	1.87 Ω
Critical Power (P_o)	16.6 W	13.9 W
Robust stability margin	74.5 %	50.5%

4.7 Model uncertainties

In practice, it is neither viable nor time-efficient to create highly refined system models to represent actual systems. Hence, approximate system models, with a good trade-off between accuracy and simplicity, are often used for design. The nominal values of their system components are generally based on known data such as nameplate information. This section investigates how uncertainties in the nominal model may influence robust stability assessment results. It also demonstrates how the μ approach may be employed to take into account possible errors in the nominal model without compromising the reliability of the results.

The approach is illustrated by applying it to the buck converter example power system in Fig 4.1. The initial values of the system components, as given in Table 4.1, are used as the nominal values for the EPS. Three cases are investigated, as defined in Table 4.14. In case I, robust stability margin is evaluated without taking into account any uncertainties in the model. Only uncertainty in the load is considered. In cases II and III, uncertainties in the model are included in the analyses. However, the approximation errors in the model for case II are larger as compared with those for case III. The other system parameters are considered to be fixed as defined in Table 4.1. This investigation aims to demonstrate how model uncertainties, which may be known to different level of accuracy, can be incorporated in robust stability analysis. In addition, it examines the effect of model uncertainties on stability margin.

Table 4.14: Uncertainties in system model

Parameters	Nominal Value	Range of variation		
		case I	case II	case III
R	2.50 Ω	± 50 %	± 50 %	± 50 %
R_{in}	135 $m\Omega$	-	± 50 %	± 30 %
L_{in}	480 μH	-	± 50 %	± 30 %
C_{in}	100 μF	-	± 10 %	± 6 %
R_{cin}	80 $m\Omega$	-	± 10 %	± 6 %
L	42 μH	-	± 50 %	± 30 %
R_l	45 $m\Omega$	-	± 10 %	± 6 %
C	590 μF	-	± 50 %	± 30 %
R_c	10 $m\Omega$	-	± 10 %	± 6 %
D	0.2768	-	± 4.5 %	± 4.5 %

4.7.1 System with no model uncertainties

This subsection evaluates the robust stability margin for case I. μ analysis is applied to the system model (4.21) with the parameters as defined in Table 4.14. The μ chart, as depicted in Fig. 4.22a and 4.22b, shows that the μ lower bound is 1.63. This corresponds to a robust stability margin of 61.4% and a critical R of 1.73 Ω , as shown in Table 4.15. The buck converter is predicted to remain stable for an output power P_o of up to 15 W .

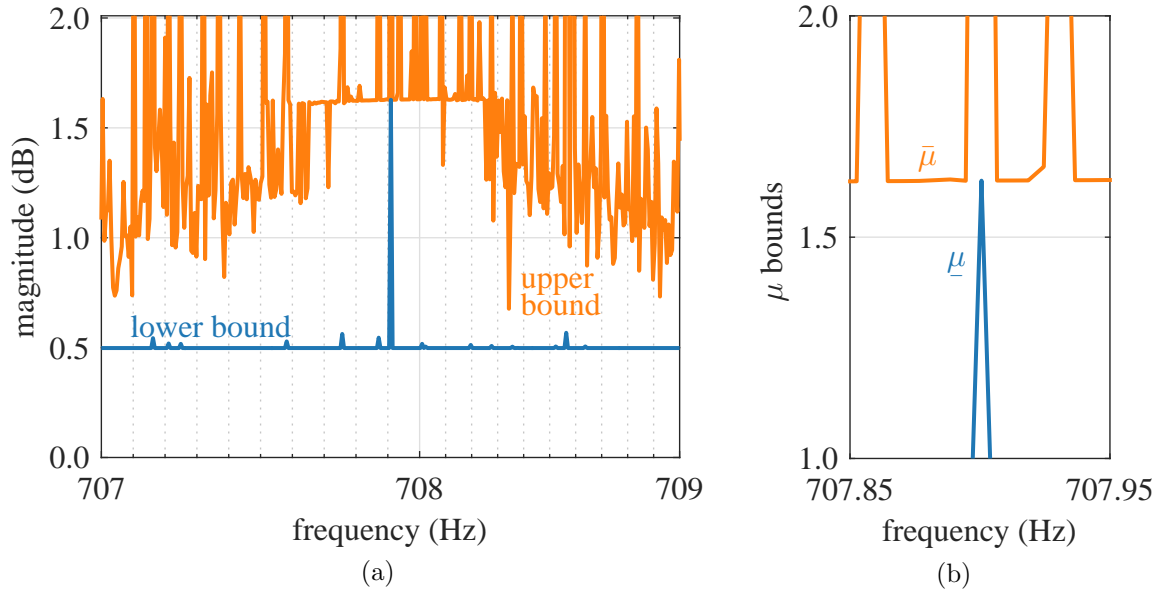


Figure 4.22: System with load uncertainty and no model uncertainty (case I) (a) μ chart to predict critical R (b) zoomed area near peak of μ chart

Table 4.15: System with load uncertainty and no model uncertainty- μ analysis results

Case study	Robust stability margin	$\underline{\mu}$	Critical R	Critical P_o
Case I	0.614	1.63	1.73 Ω	15.0 W

4.7.2 System with model uncertainties

The stability robustness for cases II and III are evaluated in this subsection. The maximum possible errors that may be expected in the nominal values, as given in Table 4.14, are taken into account in the analyses. This is based on the knowledge of the system. For instance, for case II, the tolerances of the capacitors and inductors are known to be well within 10 % of their nominal values. Parasitic elements, which may be non-linear in nature, are generally hard to quantify. Hence, the system parasitics

such as the ESR of the inductors and capacitors, have been considered to vary within a maximum range of $\pm 50\%$ within their estimated nominal values. Further, non-linear terms in the system model may be treated as uncertain elements. Hence in this case, the duty cycle D is set as an uncertain parameter with 4.5% uncertainty, based on its maximum variation range as depicted in Fig. 4.4. This eliminates the need for high order approximations, which has the added advantage of reducing the size of the uncertainty matrix. As in previous case studies, the load R is considered to vary within 50% of its nominal value. In case III, it is considered that the parameter values are known with better accuracy, with variation range of the system inductances, capacitors and ESRs being tighter, as depicted in Table 4.14.

μ analysis is applied to the system model (4.21) based on the uncertain parameters defined in Table 4.14, for cases II and III. Following the LFT operation, the structure of the uncertainty matrix, of size 351×351 , is obtained as (4.31).

$$\begin{aligned} \Delta(j2\pi f) = \text{diag}(\delta_C I_2, \delta_{Cin} I_6, \delta_D I_{189}, \delta_L I_4, \delta_{Lin} I_8, \\ \delta_R I_{41}, \delta_{Rc} I_{13}, \delta_{Rcin} I_{39}, \delta_{Rin} I_{25}, \delta_{Rl} I_{24}) \end{aligned} \quad (4.31)$$

The μ charts for cases II and III are shown in Fig. 4.23a and Fig. 4.23b respectively. The μ lower bound is 4.77 for case II. This corresponds to a robust stability margin of 21 % and a critical R of 2.24Ω , as depicted in Table 4.16. For case III, the μ lower bound is 3.47. The associated robust stability margin is 28.8 %, and the critical R is 2.14Ω . The results are shown in Table 4.16. Thus after taking into account the aforementioned uncertainties in the model, the buck converter is predicted to remain stable for an output power P_o of up to $11.6 W$ for case II, and up to $12.2 W$ for case III, as shown in Table 4.16. The results for case I are included in Table 4.16 for completion.

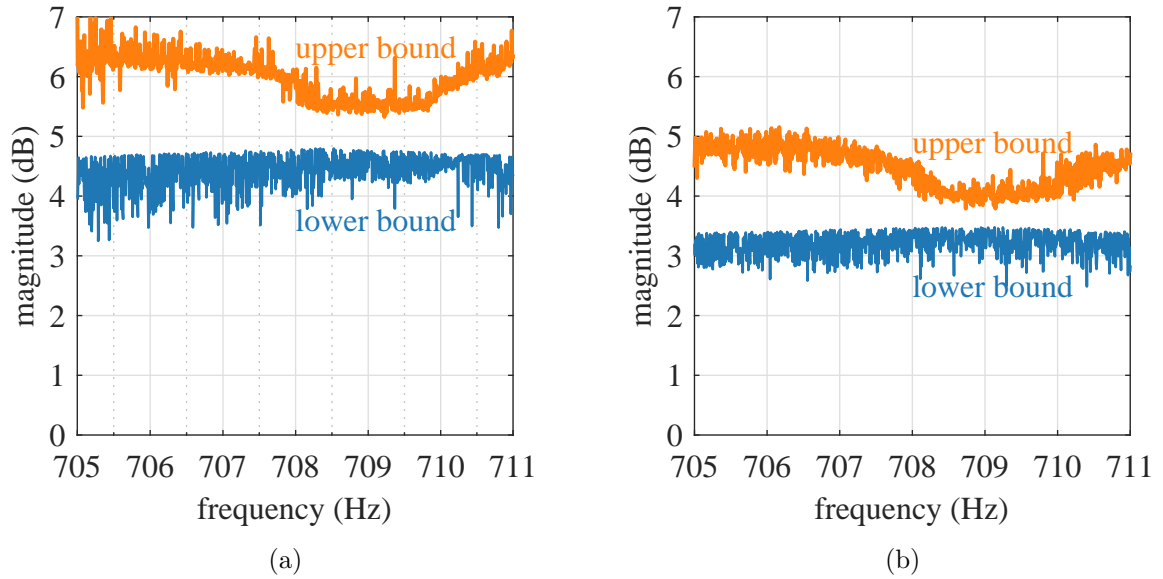


Figure 4.23: System with load and model uncertainties - μ charts to predict critical R (a) for case II (b) case III

Table 4.16: System with load and model uncertainties - μ analysis results

Case Study	Model uncertainties	Robust stability margin	$\underline{\mu}$	Critical R	Critical P_o
Case I	No	0.614	1.63	1.73 Ω	15.0 W
Case II	Yes	0.210	4.76	2.24 Ω	11.6 W
Case III	Yes	0.288	3.47	2.14 Ω	12.2 W

With the aim to verify the μ predictions, the eigenvalues of the nominal model are evaluated against the eigenvalues of the critical model for case II. The corresponding plots of the eigenvalues are depicted in Fig. 4.24a and 4.24b. It is noted that applying the critical values, predicted by μ analysis, to the system model brings the eigenvalues near to the imaginary axis. This confirms that μ analysis has identified the critical values at the boundary of stability.

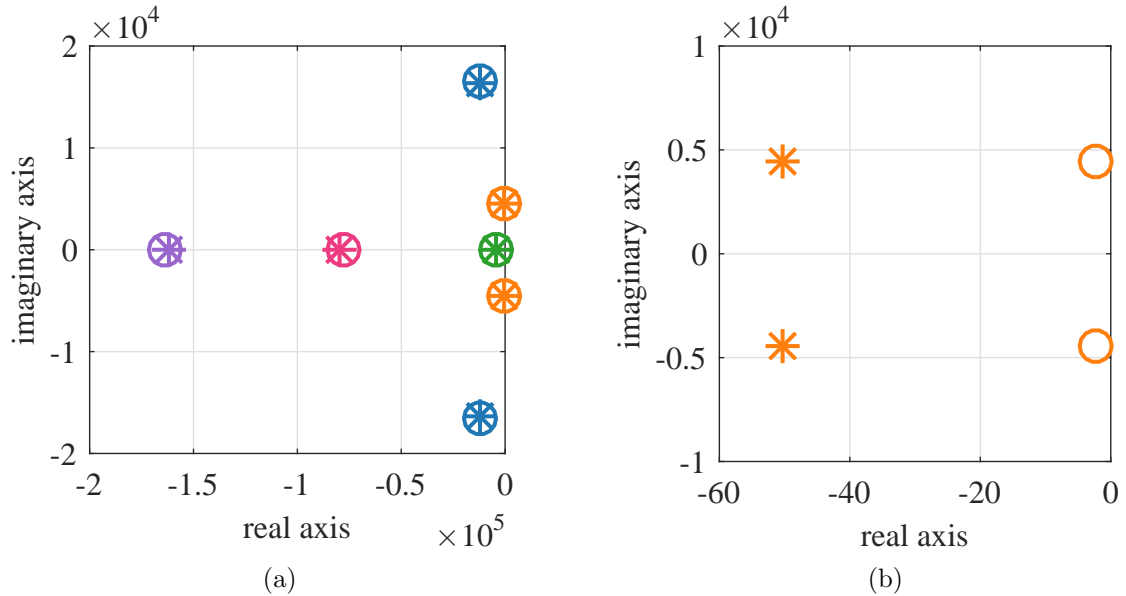


Figure 4.24: System with load and model uncertainties for case II (a) plot of eigenvalues based on μ lower bound predictions, (*) eigenvalues with nominal parameters, (o) eigenvalues with critical parameters (b) zoomed view near the imaginary axis

4.7.3 Results analysis

The robust stability margin ($1/\mu$) for cases I, II and III are depicted in Table 4.16. Based on the work developed in Chapter 3, it is interesting to note that the stability robustness for cases I, II and III are represented by hypercubes, of 10^{th} dimension, centred about the nominal point, but of sizes 0.614, 0.210 and 0.288 respectively. The actual size of the hypercubes can be obtained by using LFT equations, as described in section 4.6.

When uncertainties are not included in the model, the system has the largest hypercube with a robust stability margin of 61.4%, as depicted in Table 4.16. Although, the results may seem to be less conservative, they can not be guaranteed to be reliable, as the nominal parameters are rough estimates. With model uncertainties incorporated in the analysis, the robust stability margin is 21.0% and 28.8% for cases II and III respectively, representing smaller hypercubes with respect to case I. Although, the results seem to be conservative in comparison, they are more reliable. This is be-

cause the analyses take into account uncertainties of the system model, and therefore include worst case scenarios.

Further, the parametric space within which the system in case II is robustly stable, as given by its aforementioned hypercube, is smaller than for case III. These findings indicate that the larger the uncertainty range, the tighter is the resulting robust stability margin, and the smaller the hypercube. Yet, in both cases, the results are reliable since they include model uncertainties. It is to be pointed out that the reliability of the results is still dependent on the validity of the defined bounds of the uncertain system parameters. With μ method, the designer has the flexibility to incorporate any level of fidelity to the model, depending on available information. While the size of their hypercubes, which represent the parametric space within which the systems are robustly stable, may differ, the results are reliable in all the cases.

Of note is that incorporating model uncertainties is computationally more expensive, as can be noted in Table 4.17. This is evident since the size of the uncertainty matrix increases with the number of uncertain parameters.

Table 4.17: Evaluation of system with load and model uncertainties

Case Study	Model Uncertainties	Robust stability margin	Critical R	Size $\Delta(jw)$	Simulation time
I	No	0.614	1.73 Ω	37 \times 37	4 mins
II	Yes	0.210	2.24 Ω	351 \times 351	2.3 hours

However, it is to be noted that the computation time is also dependent on the defined frequency grid. The computation time can be kept reasonably low by using a frequency grid of low density, initially. μ analysis may then be performed around the peak of the μ chart to obtain more accurate results of μ .

4.8 Conclusion

This chapter has presented practical approaches to applying the μ approach to power electronic systems, by using the DC/DC buck converter, which is a key component for MET application.

- The study has shown how the μ method can identify the critical value of an uncertain parameter that can destabilise a system. μ analysis has determined that the buck converter example system becomes unstable when the output power to its resistive load is increased to 16 W . This prediction is supported by experimental results both in the time domain and the frequency domain.
- The work in this chapter has also shown the practical limitations of applying the classical Middlebrook criterion and Nyquist stability criterion to the buck converter system in the laboratory. Experimental application of Middlebrook criterion is often not feasible for certain configuration of component grouping in the hardware. Experimental application of the Nyquist stability criterion could not be used to obtain precise predictions of instability conditions.
- Further, μ analysis has been employed to predict the destabilising output power of the buck converter under study to good accuracy, for varying values of line resistance. All the results have been validated in experiment.
- The chapter has also shown how the μ approach can be employed to take into account uncertainties in operating conditions. The robust stability margin of the buck converter has been found to be 74.5% when uncertainties in temperature are not included, as compared to 50.5% when uncertainties in temperature are included. The findings emphasise the necessity of incorporating operating conditions uncertainties for more reliable stability analysis of a system.
- The study has demonstrated how the μ tool can be employed to account for uncertainties, including certain classes of non-linearities and parasitics, that are inherent in a system model. Although the literature states that the μ

method treats a physical system as an uncertain model, it does not show the practical approach to achieving that. This chapter has catered for this gap in the literature.

μ analysis has predicted the critical output power of the considered buck converter to be 15.0 W , when model uncertainties are neglected. On the other hand, the critical output power has been determined as 12.2 W , when uncertainties are included, while its value dropped to 11.6 W , when the given uncertainties are defined within a relatively wider range.

It can be inferred that results tend to be highly optimistic when uncertainties are neglected, yet more reliable when uncertainties are included. Further, although the robust stability margin is tighter when uncertainties are defined within wider ranges or with less accuracy, the results can be employed more reliably as worse case scenarios are accounted for.

- The methodology that is required to apply the μ method through MATLAB® Robust Control Toolbox has been shown in a manner that is clear enough to enable a user to reapply it to other uncertain systems.
- The influence of the size of perturbation matrices on computational time has been discussed.

The work presented in this chapter has many implications. Often times, the design engineer does not have sufficient information as to the exact values of the system components. Yet, the parameters may be estimated within some reasonable bounds. With the μ approach, the designer is offered the flexibility of determining the best trade-off between accuracy and practicality, by choosing the levels of details that is incorporated into modelling. The great benefit of the μ tool is that different types of uncertainties, in operating conditions and in the model, can be easily included in the analysis, by using the same model but only defining the considered uncertain elements differently. The methodology for applying the μ approach has been presented in a generalised and clear manner, which allows it to be extended to wider applications, and to include yet further sources of uncertainties

Chapter 5

A modelling methodology for μ analysis of non-linear systems

5.1 Introduction

Power electronic systems in the MET may be subject to multiple sources of perturbations, which may be due to variations in their environmental conditions or fluctuations in their load demand. These types of uncertainties may lead to variation in system parameters, which may consequently cause the system operating points to change. As was demonstrated in Chapter 4, these uncertainties may compromise system stability. Based on this insight, it seems necessary to investigate robust stability of such EPS, not only at a given operating point, but over a range of operating points. Such stability assessment is required both at the small and large signal level. As mentioned in the thesis introduction, small-signal stability analysis, being an important concern in the reliable operation of PE systems, is the focus of this work. Most small-signal stability analysis techniques work on linear system models. However the physical systems are generally better represented by non-linear system models. Hence, there is a need for analysis techniques to assess the stability of non-linear systems, under a wide variation of parameter uncertainties and operating points.

In order to apply small-signal analysis technique to a non-linear uncertain EPS, the system must first be divided into a number of linear models, each pertaining to a particular operating point. Each linear model is then analysed with respect to the set of considered parametric uncertainties. It is to be appreciated that this process can lead to an arbitrarily large number of linear models. The task can be challenging, particularly for classical techniques. In addition to the linearisation process, they have to perform extensive iterations on each linear model in order to account for uncertainties. Yet, the authors in [17] have applied the classical impedance-based ESAC criterion to non-linear systems. They have developed a software to make the process automatic. However, in addition to being laborious, it has been reported that the SISO-based techniques may not produce reliable results when applied to systems with multiple uncertainties [31],[33].

The μ approach can reliably be employed to account for all considered parametric uncertainties. However, the method is generally applied to study the effect of uncertainties on the stability of a linear system model, at a particular operating point. One problem of applying the method to a non-linear system is that, the parameters, being allowed to vary within their defined sets, may cause the operating point to change, and that too in a non-linear manner. It is therefore important to account for the dependencies of the operating points on parametric uncertainties in the robust stability assessment. A few studies have applied the μ approach to non-linear systems. The method proposed in [45] approximates the non-linear elements in the state space system matrix by a series of linear terms, while [41] uses combined numerical and symbolic linearisation techniques on the non-linear system. However, due to the applied approximations, these methods may not fully account for all dependencies of operating points on parametric uncertainties. It is to be noted that these methods were developed for large scale power systems, for which the possible loss in accuracy in the results may be justified.

As stated in the introduction chapter, this thesis aims at making the μ approach more applicable to power electronic systems. By shedding light on the μ theory and presenting practical approaches to applying the method, the previous Chapters 2 - 4

have made the μ tool more application-friendly. This study aims at extending the applicability of the μ method to non-linear system models. The objective is to develop a modelling methodology to convert a non-linear system to a unique equivalent linear model, while catering for all dependencies of operating points on systems parameters. The developed model needs to be valid for μ analysis over a defined range of operating points and parameter uncertainties. The methodology is based solely on the symbolic linearisation technique. It must fully account for all system non-linearities, in view of reducing conservativeness in stability assessment. The modelling approach is developed in this chapter, by applying it to a 4 kW PM machine drive system. The method is verified through μ analysis of the equivalent linear model of the considered system with torque uncertainty, over a range of different operating points and under parameter variations. Further, the predictions from μ analysis are to be validated against experimental results. Of note is that the method, proposed in this chapter, has been applied to the EPS with the ideal CPL in Chapter 3 and the DC/DC buck converter in Chapter 4, although it was not fully elaborated in these chapters.

5.2 Permanent magnet machine drive system

5.2.1 System structure

The power system under study is depicted by the circuit representation in Fig. 5.1. The system represents a hybrid distribution topology considered for the MEA power system [52]. The engine driven ac generator, controlled by the generator control unit, is considered as an ideal 3-phase balanced voltage source, for the purpose of this study. The transmission line from the power supply to the rectifier is modelled by an RL circuit. The six-pulse uncontrolled rectifier in Fig. 5.1, represents typically employed multiphase autotransformer-rectifier (ATRU) units of a real on-board system. It provides DC power to the surface mounted PM machine based electromechanical actuator (EMA) through an LC filter. The EMA is a standard vector-controlled PM motor drive depicted in Fig. 5.2 [52].

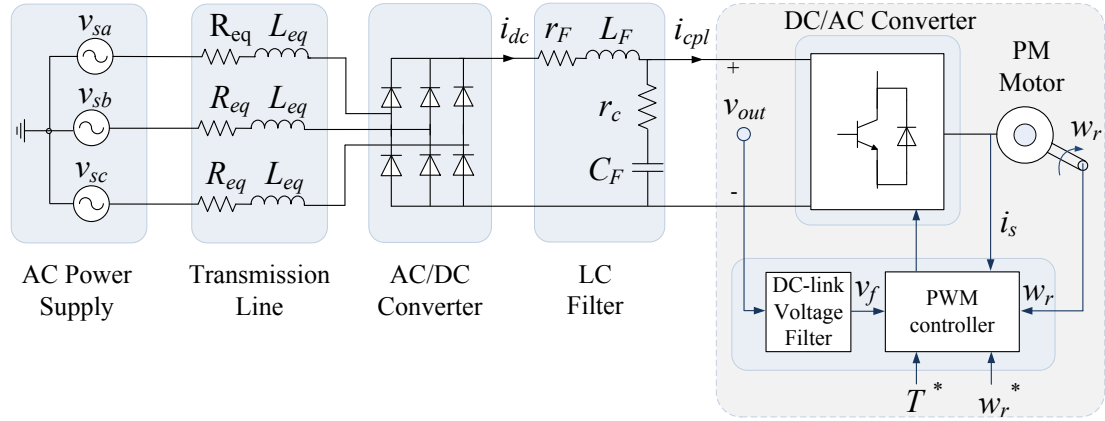


Figure 5.1: The main elements of a distribution system of the aircraft power system architecture

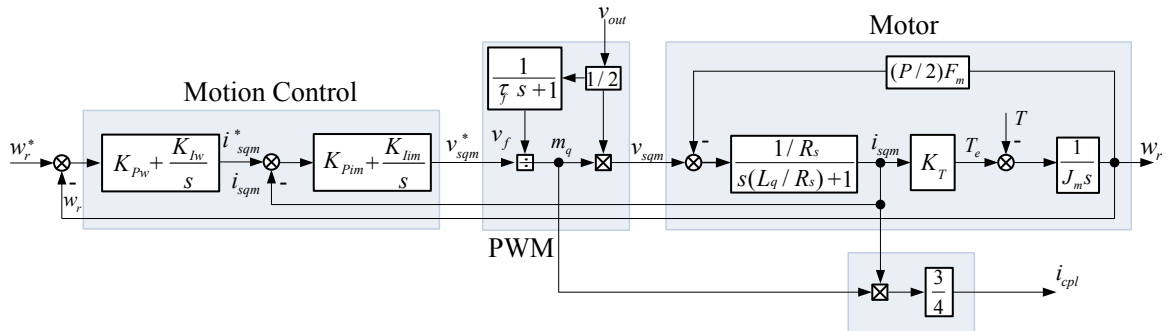


Figure 5.2: Block diagram of the PM motor drive system

The parameters of the example power system are defined in Table 5.1. With the assumption that the amplitude of the AC supply and the DC load current are constant and that commutation occurs only once during a commutation period, the power stage in Fig. 5.1 is modelled by the circuit in Fig. 5.3 by using the average-value modelling method [7],[17],[52].

The six-pulse diode rectifier is modelled by the DC voltage source V_e in series with the equivalent resistance R_e and the equivalent inductance L_e which are given by (5.1) - (5.3). The transmission line inductance causes an overlap angle and hence a commutation voltage drop which is represented on the DC side by r_μ in (5.4), [52].

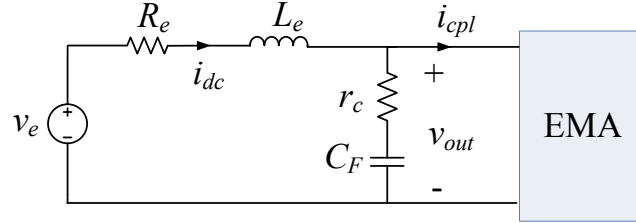


Figure 5.3: Averaged model of the system in Fig. 5.1

$$v_e = \frac{3\sqrt{3}\sqrt{2}}{\pi} v_s \quad (5.1)$$

$$R_e = r_\mu + r_F + 1.824R_{eq} \quad (5.2)$$

$$L_e = L_F + 1.824L_{eq} \quad (5.3)$$

$$r_\mu = \frac{3\omega L_{eq}}{\pi} \quad (5.4)$$

5.2.2 Experimental hardware

In this chapter, μ analysis is employed to predict the destabilising torque of the EPS shown in Fig. 5.1 - 5.3, over a range of operating points and under certain parameter variations. The stability of the aforementioned EPS has been investigated previously both analytically based on the classical eigenvalue method, and experimentally by Kongpan Areerak [52]. The μ predictions, in this study, are to be evaluated against the experimental results reported in [52]. The experimental test rig, used in [52], is described here for the sake of completion [52].

Fig. 5.1 is a good circuit representation of the experimental rig used in [52]. A 12 kVA programmable ac source (model 61705 Chroma) is used as an ideal voltage source. The sinusoidal supply voltage can be varied up to 300 V and the source frequency can be varied up to 1.2 kHz. Three phase line inductance, with a value of 60 μF per phase, is used for the transmission line. A three phase six-pulse diode rectifier provides DC voltage to the 540 V DC bus, through a DC-link filter. The parameter

Table 5.1: Nominal values for system parameters

Symbols	Units	Nominal Values	Description
v_s	V_{rms-ph}	223	phase source voltage
w	rad/s	$2\pi 50$	source frequency
R_{eq}	Ω	0.045	line resistance
L_{eq}	μH	60	line inductance
r_F	Ω	0.2	DC-link inductor resistance
L_F	mH	24.15	DC-link inductance
r_c	Ω	0.4	ESR of DC-link capacitor
C_F	μF	320	DC-link capacitance
w_{rated}	rpm	1140	rated speed
w_r^*	rpm	800	speed reference
T_{rated}	Nm	40	rated load torque
R_s	Ω	0.5	stator resistance
L_q	mH	2.3	stator leakage inductance
P	poles	20	number of poles
J_m	kgm^2	0.004	moment of inertia
F_m	Wb	0.123	constant flux of PM machine
K_{Pim}	-	4.124	current loop proportional gain
K_{Iim}	-	3632	current loop integral gain
$w_{n,current}$	Hz	200	natural frequency of current loop
K_{Pw}	-	0.02	speed loop proportional gain
K_{Iw}	-	0.863	speed loop integral gain
$w_{n,speed}$	Hz	10	natural frequency of speed loop
η	%	88.83	Efficiency of PM motor

values of the DC-link filter are given in Table 5.1. A six phase two level voltage inverter, using 100 A, 1200 V inverter leg modules, is used to supply power to the 4 kW ac PM motor. The controller for the motor drive uses Texas instruments C6713 floating point DSP, and a high speed Actel, ProAsic3 FPGA.

Experiments were performed to measure the destabilising torque of the EPS. A rig dynamometer was used to apply increasing torque to the PM motor. The DC link voltage was observed for sustained oscillations, which indicate that the system is at the boundary of stability. A power analyser and a torque meter were used to measure the power and torque of the PM motor respectively. The experiments were repeated with variations in the system frequency f , bandwidth of the DC-link voltage filter f_{cutoff}

and natural frequency of the speed loop f_n . The system frequency was varied on the programmable ac source. The frequencies f_{cutoff} and f_n were set at different values by changing the code in the controller board. The destabilising torque of the PM machine drive system was measured under variation in load torque, and the aforementioned parameter values. The experimental results, which have been reported in [52], will be used to validate the predictions from μ analysis in the subsequent sections

5.3 Modelling methodology

This section describes the methodology for representing a non-linear system by an equivalent linear model which is valid for all operating points and parameter variations. The approach is illustrated by applying it to the PM machine drive system, which is the most typical electromechanical actuator in the MEA.

5.3.1 Symbolic linearisation

The non-linear equations for the PM machine drive are given by (5.5) - (5.11) where $K_T = 3PF_m/4$ and $i_{cpl} = 3v_{sqm}^*i_{sqm}/4v_f$ [52]. The parameters in the aforementioned equations are defined in Table 5.1. The system voltages, currents, motor speed and torque are shown in Fig. 5.1 - 5.3. The voltage across the DC-link capacitor is assumed to be equal to v_{out} given that the voltage drop across the ESR of the capacitor is very small.

$$\frac{di_{dc}}{dt} = -\frac{(r_c + R_e)}{L_e}i_{dc} + \frac{r_c}{L_e}i_{cpl} - \frac{v_{out}}{L_e} + \frac{v_e}{L_e} \quad (5.5)$$

$$\frac{dv_{out}}{dt} = \frac{1}{C_F}i_{dc} - \frac{1}{C_F}i_{cpl} \quad (5.6)$$

$$\frac{dw_r}{dt} = \frac{K_T}{J_m}i_{sqm} - \frac{1}{J_m}T \quad (5.7)$$

$$\frac{di_{sqm}}{dt} = -\frac{PF_m}{2L_q}w_r - \frac{R_s}{L_q}i_{sqm} + \frac{1}{2L_q}\frac{v_{sqm}^*v_{out}}{v_f} \quad (5.8)$$

$$\frac{dv_f}{dt} = -\frac{1}{\tau_f}v_f + \frac{1}{2\tau_f}v_{out} \quad (5.9)$$

$$\frac{dv_{sqm}^*}{dt} = -K_{Iim}i_{sqm} + K_{Iim}i_{sqm}^* - K_{Pim}\frac{di_{sqm}}{dt} + K_{Pim}\frac{di_{sqm}^*}{dt} \quad (5.10)$$

$$\frac{di_{sqm}^*}{dt} = -K_{Iw}w_r + K_{Iw}w_r^* - K_{Pw}\frac{dw_r}{dt} + K_{Pw}\frac{dw_r^*}{dt} \quad (5.11)$$

Prior to the linearisation of the system model, the non-linear equations are converted into a non-linear state space form where the vectors x , u and y denote system states, inputs and outputs respectively, and are given as:

$$x: \quad i_{dc}, v_{out}, w_r, i_{sqm}, v_f, v_{sqm}^*, i_{sqm}^*$$

$$u: \quad v_e, w_r^*, T$$

$$y: \quad v_{out}$$

An arbitrary equilibrium point is defined by X_o and U_o which denote steady state values of state vector x and input vector u respectively, and are given as:

$$X_o: \quad I_{dco}, V_{outo}, w_{ro}, I_{sqmo}, V_{fo}, V_{sqmo}^*, I_{sqmo}^*$$

$$U_o: \quad V_e, w_r^*, T_o$$

The input V_e and w_r^* are constant over all operating points. The load torque T is denoted as T_o at steady state. Finally, the non-linear state space system is linearised around equilibrium point (X_o, U_o) by using standard linearisation technique.

5.3.2 State space matrix elements expressed in terms of system parameters and inputs

This step involves expressing explicitly all elements of the resulting linearised state space model as functions of only system parameters and inputs. Any indeterminate elements in the system model such as equilibrium points must be expressed in terms of definable system parameters and inputs.

For the system under study, firstly, X_o , as given by (5.12) - (5.18), is derived by setting (5.5) - (5.11) to zero.

$$I_{dco} = I_{cpl0} = 3V_{sqmo}^* I_{sqmo} / 2V_{out0} \quad (5.12)$$

$$V_{out0} = -R_e I_{dco} - V_e \quad (5.13)$$

$$w_{ro} = w_r^* \quad (5.14)$$

$$I_{sqmo} = T_o / K_T \quad (5.15)$$

$$V_{fo} = V_{out0} / 2 \quad (5.16)$$

$$V_{sqmo}^* = V_{sqmo} = R_s I_{sqmo} + PF_m w_{ro} / 2 \quad (5.17)$$

$$I_{sqmo}^* = I_{sqmo} = T_o / K_T \quad (5.18)$$

The steady state variables I_{dco} in (5.12) and V_{sqmo}^* in (5.17) are then further rearranged and expressed as (5.19) and (5.20). In addition, V_{out0} in (5.13) is expressed as (5.21) by using the constant power load equation $I_{dco} = P_o / V_{out0}$ where $P_o = T_o w_{ro} / \eta$.

$$I_{dco} = \frac{(3T_o / 2K_T)(R_s T_o / K_T + PF_m w_{ro} / 2)}{V_{out0}} \quad (5.19)$$

$$V_{sqmo}^* = R_s T_o / K_T + PF_m w_{ro} / 2 \quad (5.20)$$

$$V_{out0} = \frac{V_e}{2} \left[1 + \sqrt{1 - \frac{4R_e T_o w_{ro}}{\eta V_e^2}} \right] \quad (5.21)$$

The flexibility of the linearised model, which now contains only determinate parameters and inputs in symbolic form, serves to cater for the system non-linearities. However, the linearised model contain non-rational terms in (5.21), which is not suitable for LFT modelling.

5.3.3 Rational approximation of non-rational terms

All non-rational elements in the linearised system model are to be expressed in their rational forms as is required for the conversion of the system model in its corresponding LFT configuration. In our case, the non-rational expression of V_{outo} in (5.21) is estimated in its rational form as in (5.22) by using the first two terms of the binomial expansion of the square root term in (5.21). The expression (5.22) is a good approximation of V_{outo} with respect to variations in torque as shown in Fig. 5.4.

$$V_{outo-est} = V_e - \frac{R_e T_o w_{ro}}{\eta V_e} \quad (5.22)$$

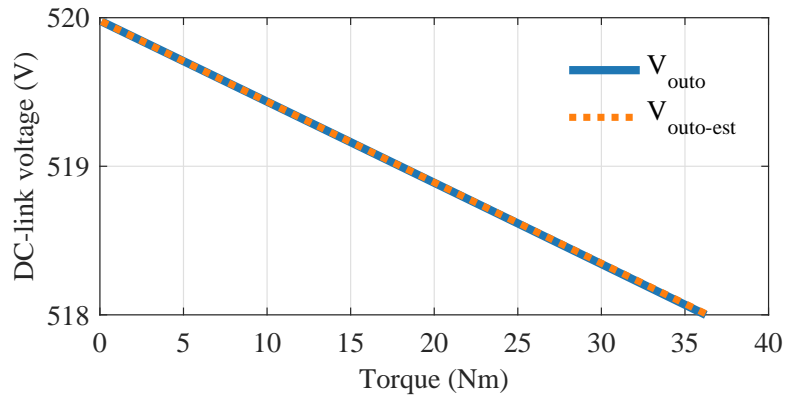


Figure 5.4: Polynomial approximation of the steady state DC-link voltage V_{outo}

5.3.4 The equivalent linear model

After applying the above steps, the state space model $\begin{pmatrix} A & B \\ C & D \end{pmatrix}$, given by matrices (5.25), is obtained where V_{sqmo}^* , $V_{outo-est}$, A_{subs1} and A_{subs2} are given by (5.20), (5.22), (5.23) and (5.24) respectively. The developed model represents with good accuracy the system for all operating points and parameter variations, and is directly suited for μ analysis.

$$A_{subs1} = \left(-K_{Pim}K_{Iw} + \frac{K_{Pim}PF_m}{2L_q} \right) \quad (5.23)$$

$$A_{subs2} = -K_{Iim} - \frac{K_{Pim}K_{Pw}K_T}{J_m} + \frac{K_{Pim}R_s}{L_q} \quad (5.24)$$

5.3.5 Validity of the equivalent linear model over a range of operating points

The equivalent linear model represents the non-linear system over a range of operating points and parameter variations. In order to illustrate this point, in this section, the nominal values of R_e and the speed reference w_r^* , in the studied system in Fig. 5.1 - 5.3, denoted by R_{eo} and w_{ro}^* have deliberately been set to 3.6Ω and 3000 rpm respectively. The nominal torque T_{oo} is kept at 20 Nm and the other system parameters are defined as in Table 5.1. These larger parameter values introduce more non-linearity in the system by causing a larger voltage drop in the DC-link voltage v_{out} , as can be noted from (5.21). This increase in non-linearity better serves the purpose of illustration. For practical systems, with long interconnecting cables and large source impedance, it is not improbable that the value of R_e is very high. Based on the new parameter values, the voltage V_{outo} is now better estimated by the third order binomial approximation, denoted by $V_{outoest3}$ and shown in Fig. 5.5.

$$\begin{array}{c}
\left[\begin{array}{cccccccc}
-\frac{r_c + R_e}{L_e} & -\frac{1}{L_e} & 0 & \frac{3r_c V_{sqmo}^*}{2L_e V_{\text{outo-est}}} & -\frac{3r_c T_o V_{sqmo}^*}{L_e K_T V_{\text{outo-est}}^2} & \frac{3r_c T_o}{2K_T L_e V_{\text{outo-est}}} & 0 & \frac{1}{L_e} & 0 & 0 \\
\frac{1}{C_F} & 0 & 0 & \frac{-3V_{sqmo}^*}{2C_F V_{\text{outo-est}}} & \frac{3V_{sqmo}^* T_o}{C_F K_T V_{\text{outo-est}}^2} & \frac{-3T_o}{2C_F K_T V_{\text{outo-est}}} & 0 & 0 & 0 & 0 \\
0 & 0 & 0 & \frac{K_T}{J_m} & 0 & 0 & 0 & 0 & 0 & -\frac{1}{J_m} \\
0 & \frac{V_{sqmo}^*}{L_q V_{\text{outo-est}}} & \frac{-PF_m}{2L_q} & \frac{-R_s}{L_q} & \frac{-2V_{sqmo}^*}{L_q V_{\text{outo-est}}} & \frac{1}{L_q} & 0 & 0 & 0 & 0 \\
0 & \frac{1}{2T_f} & 0 & 0 & \frac{1}{-T_f} & 0 & 0 & 0 & 0 & 0 \\
0 & \frac{-K_{Pim} V_{sqmo}^*}{L_q V_{\text{outo-est}}} & A_{subs1} & A_{subs2} & \frac{2K_{Pim} V_{sqmo}^*}{L_q V_{\text{outo-est}}} & \frac{-K_{Pim}}{L_q} & K_{Iim} & 0 & K_{Pim} K_{Iw} & \frac{K_{Pim} K_{Pw}}{J_m} \\
0 & 0 & -K_{Iw} & \frac{-K_{Pw} K_T}{J_m} & 0 & 0 & 0 & 0 & K_{Iw} & \frac{K_{Pw}}{J_m} \\
\frac{1}{L_e} & 0 & 0 & 0 & 0 & 0 & 0 & 0 & 0 & 0 \\
0 & 1 & 0 & 0 & 0 & 0 & 0 & 0 & 0 & 0
\end{array} \right] \quad (5.25)
\end{array}$$

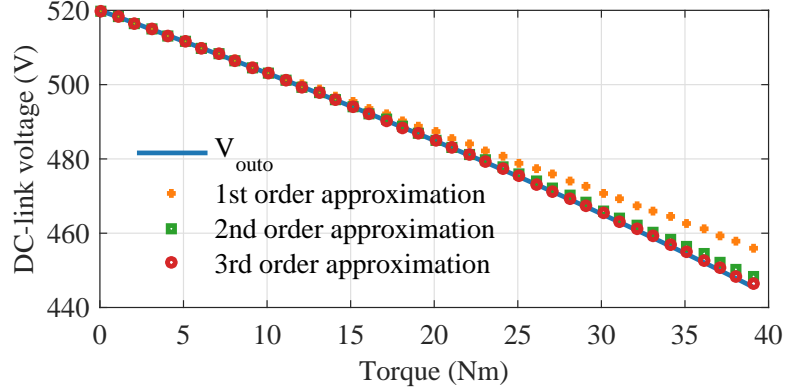


Figure 5.5: Polynomial approximation of the steady state DC-link voltage V_{outo} with $R_e = 3.6 \Omega$ and $w_r^* = 3000 \text{ rpm}$

In view of illustrating the validity of the equivalent linear model over a range of operating conditions, a number of operating points of the system ($I_{cpl0}, V_{outo-est3}$) are plotted in Fig. 5.6, when both T_o and R_e are subject to variations. With R_e , w_r^* and T_o set to the aforementioned nominal values and the rest of the system parameters defined as in Table 5.1, the nominal operating point can be shown to lie at the point Eq_{10} in Fig. 5.6. For variable R_e ($\pm 40\%$ of R_{eo}) and fixed torque (20 Nm), the operating points move along curve 1 in Fig. 5.6. On the other hand, for variable T_o ($\pm 90\%$ of T_{oo}) and fixed R_{eo} (3.6Ω), the operating point moves between Eq_{20} and Eq_{30} . The operating points Eq_{20} and Eq_{30} correspond to the minimum and maximum torque respectively. Hence, when both T_o and R_e vary, the operating points will lie between curves 2 and 3.

Thus, the generalised linear model converts to specific linear models about distinct operating points depending on the values assigned to the system parameters and inputs. The equivalent linear model is thus valid for all defined operating points and parameter uncertainties of the system.

Furthermore, the developed system model being linear is now suitable for μ analysis. Since the μ approach explicitly takes into account all varying system parameters and inputs, it becomes clear that in fact it assesses stability robustness of a non-

linear system over all corresponding operating points, as will be demonstrated in the subsequent section.

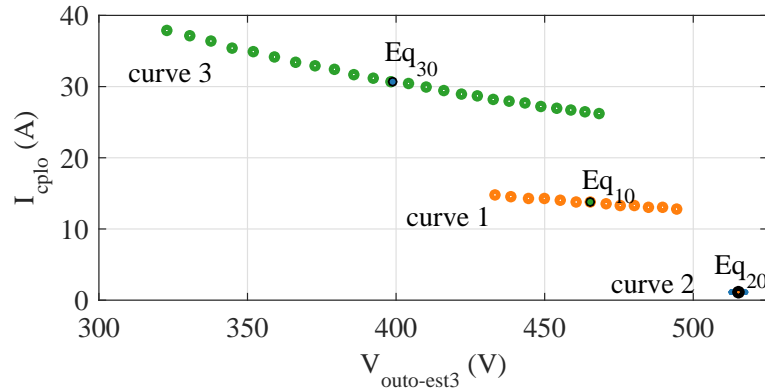


Figure 5.6: Operating points with varying torque T_o and line resistance R_e

5.4 Load uncertainty

In this section, μ analysis is applied to determine stability robustness of the EPS, shown in Fig. 5.1 - 5.2, when it is subject to uncertainty in load torque. The torque T_o is considered to vary within $\pm 90\%$ of its nominal value of 20 Nm as depicted in Table 5.2, while all other system parameters are assumed to be constant and equal to their nominal values as defined in Table 5.1. The system is studied with no DC-link voltage filter. The destabilising torque predicted by μ analysis is also verified against experimental results.

Table 5.2: Torque Uncertainty

Parameter	Average value (T_{oo})	Range of variation wrt average value (T_{var})
Torque (T_o)	20 Nm	$\pm 90\%$

5.4.1 LFT modelling

The application of μ analysis requires that the equivalent linear model be first converted in the LFT form [53]. The function ‘robuststab(sys, omega)’, in MATLAB[®] Robust Stability Toolbox, performs both LFT operation and μ analysis on the state space system model, denoted as ‘sys’, over the defined grid of frequencies, denoted as ‘omega’. For this case study, ‘sys’ is given by (5.25).

The operation of LFT involves firstly expressing all uncertain parameters in the system model as LFTs. The torque T_o , which is bounded in the interval [2 Nm, 38 Nm], (i.e. within $\pm 90\%$ of T_{oo}), can be represented as a perturbation in its normalised form δ_T bounded within [-1, 1]. Thus, T_o can be expressed as an LFT in δ_T based on (5.26) and the values in Table 5.2 [53],[67].

$$T_o = T_{oo} + T_{oo}T_{var}\delta_T, \quad \delta_T = [-1, 1] \quad (5.26)$$

From Fig. 5.7, which is an illustration of (5.26), it can be seen that when the ‘perturbation’ in torque is absent, $\delta_T = 0$, the torque is equal to its average value of $T_o = T_{oo} = 20$ Nm. When the ‘perturbation’ is at its maximum, either $\delta_T = -1$ at the low end of the uncertainty range where $T_o = T_{min} = 2$ Nm, or $\delta_T = 1$ at the high end of the uncertainty range where $T_o = T_{max} = 38$ Nm. The critical torque, as represented by the point $(\delta_{T_{cr}}, T_{cr})$ in Fig. 5.7, will be determined by μ analysis in the next section.

Based on the LFT operation, all normalised parameters δ_T are then extracted from the system model (5.25) and grouped in a diagonal matrix in a feedback form. This results in the system model being converted in its LFT form as shown in Fig. 2.3a. The resulting disturbance matrix is given by (5.27) where δ_T appears 24 times since T_o appears that number of times in the uncertain system model.

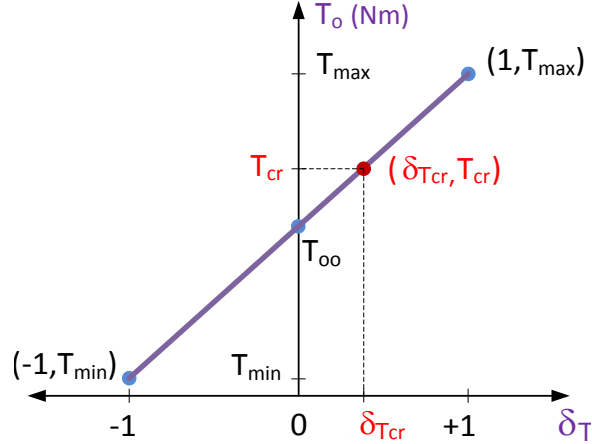


Figure 5.7: Relationship between torque and the normalised disturbance in torque

$$\Delta(j\omega) = \delta_T I_{24 \times 24} \quad (5.27)$$

It is worth noting that the order of an uncertainty matrix is dependent on the number of uncertain parameters as well as on the size and complexity of the power system being analysed. It also depends on the order of polynomial approximation of certain system elements, such as V_{outo} in (5.22) for the system under study. Unfortunately, the higher the order of the uncertainty matrix, the higher is the computational burden [34]. Nevertheless, there exists some order reduction methods that can be used to minimise the size of these matrices [68].

5.4.2 μ analysis

By applying SSV analysis to the system in its LFT form, the smallest disturbance matrix that causes instability is identified. MATLAB[®] Robust stability toolbox has been employed to compute μ bounds of the system under study [53][50][67]. The results of μ analysis, as depicted in Fig. 5.8a - 5.8b, show the peak values of the lower and upper bounds of μ , which are in this case the same and equal to 2.38 at the frequency of 57.04 Hz.

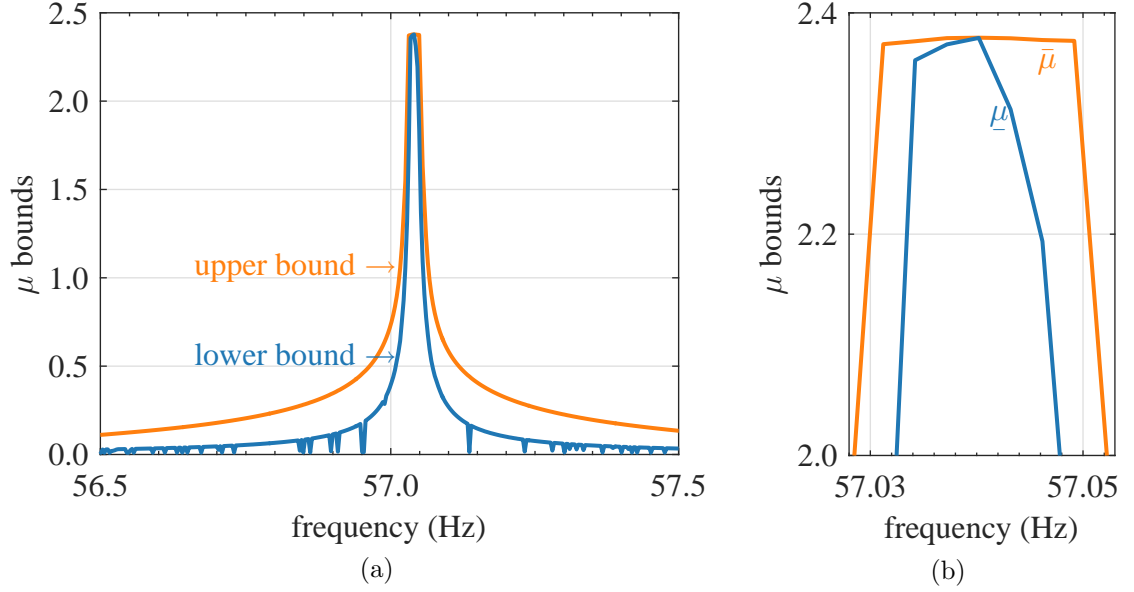


Figure 5.8: System with uncertain torque (a) μ chart to predict critical T (b) zoomed area near peak of μ chart

The critical frequency corresponds to the resonant frequency of the LC filter which can be estimated as $1/(2\pi\sqrt{L_F C_F})$. Based on the μ analysis results, the smallest destabilising disturbance matrix is extracted as in (5.28), and the robust stability margin is calculated as $\min(\bar{\sigma}(\Delta)) = 1/\mu = 0.42$. The destabilising torque T_{cr} , computed from (5.29) and $\delta_{T_{cr}} = 0.42$, is equal to 27.6 Nm which is equivalent to the critical power of 2.6 kW.

$$\Delta_{cr}(j2\pi 57.04) = \delta_{T_{cr}} I_{24 \times 24} = 0.42 I_{24 \times 24} \quad (5.28)$$

$$\begin{aligned} T_{cr} &= T_{oo} + T_{oo} T_{var} \delta_{T_{cr}} \\ &= 20 + 20 \times 0.9 \times (0.42) \\ &= 20 + 20 \times 37.8\% = 27.6 \end{aligned} \quad (5.29)$$

The system is not robustly stable, as confirmed by the result, $\mu > 1$. This indicates that the system may become unstable if operated within its defined maximum uncer-

tainty set (i.e. within 20 ± 18 Nm). The robust stability margin of 0.42 represents the ratio by which the maximum range of uncertainty in torque must be scaled to ensure stability robustness, as discussed in Chapter 2, and depicted in Fig. 5.9. This requires that the operation of the EPS under study be limited within $(20 \pm 37.8\%)$ or $(20 \pm 7.6\text{Nm})$, which can be derived based on computation shown in (5.29). In the same light of thought, the PM machine drive can be ensured robustly stable within the hypercube, of single dimension, of size 0.42, about the nominal point, as shown in Fig. 3.7 in Chapter 3, and in Fig 5.9. The correlation between the robust stability margin and the hypercube of the case under study is clearly depicted in Fig. 5.9. Based on the positive sign of $\delta_{T_{cr}}$, as shown in (5.28), the destabilising torque is confirmed as the upper limit of this range at 27.6 Nm. This section has shown how μ can provide a direct a measure of stability robustness of an EPS.

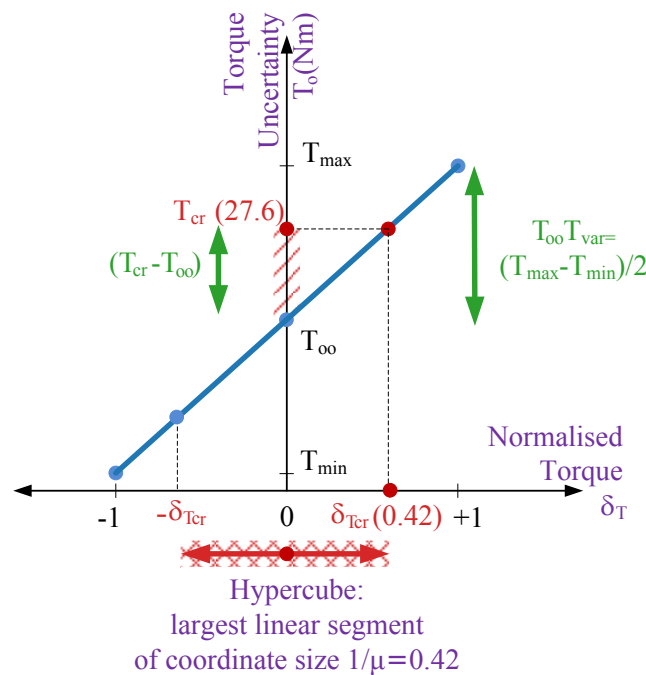


Figure 5.9: Robust stability margin and hypercube for system with uncertain torque

One known difficulty with μ analysis, as reported in section 2.6 in Chapter 2, is that the the lower μ bound may fail to converge when uncertain parameters are purely real [36],[37],[50]. This problem was encountered at the outset of this study. Hence,

a very small complexity of $\alpha = 0.1\%$ was added to the real parametric uncertainty torque T_o by using the command “complexify” in MATLAB[®] Robust stability toolbox, as described in appendix A. This was sufficient to make the μ lower bound converge [53].

5.4.3 Simulation results

The PM machine drive, modelled in the Simulink[®] environment, has enabled time-domain verification of the result from μ analysis. The time domain simulation results are depicted in Fig. 5.10a - 5.10b.

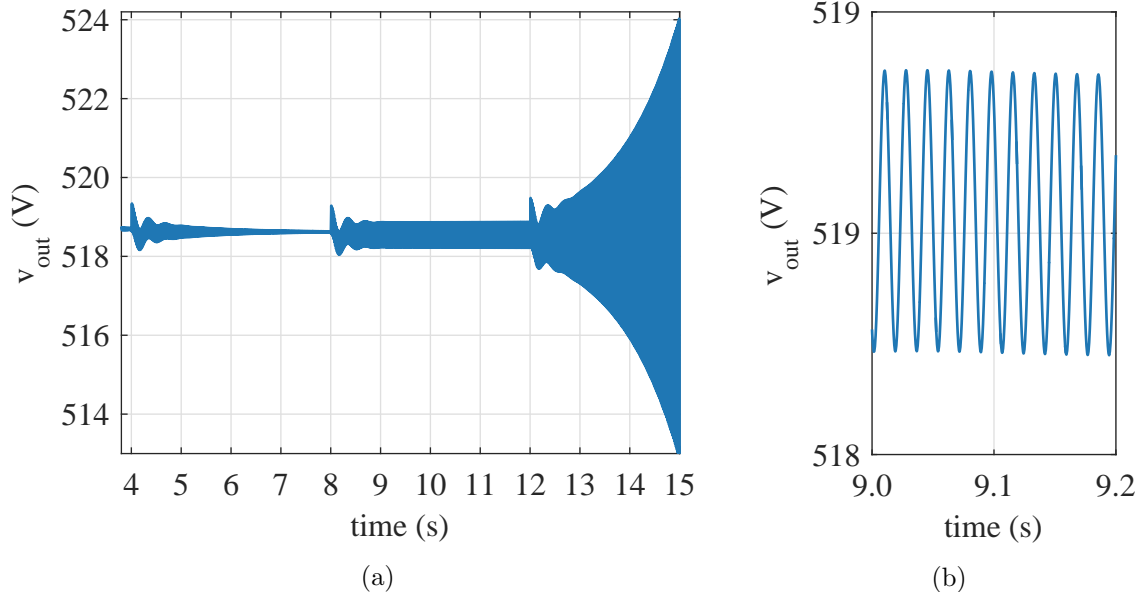


Figure 5.10: Time domain simulation of DC-link voltage $v_{out}(t)$ (a) (i) at $t=4s$, $T = 0.95T_{cr}$ (ii) at $t=8s$, $T = T_{cr}$ (iii) at $t=12s$, $T = 1.05T_{cr}$, where T_{cr} is the critical torque (b) zoomed area near $t = 9.1 s$

With the speed kept constant at 800 rpm, three values of torque are applied in steps to the model. At time $t = 4 s$, 95% of the critical torque (26.2 Nm) is applied to the

system and the DC-link voltage $v_{out}(t)$ stabilises with time as can be seen in Fig. 5.10a and 5.10b. At time $t = 8$ s, application of the critical torque $T_{cr} = 27.6$ Nm causes the system to reach boundary stability with sustained DC-link voltage oscillations. This confirms the results from μ analysis which predicted the critical torque of 27.6 Nm. Applying an additional torque of 5% over its critical value at $t = 12$ s causes the system to become unstable as shown in Fig. 5.10a.

5.4.4 Experimental results

A number of experiments were undertaken on the considered PM machine drive test rig, as described in section 5.2.2, and reported in [52]. It was found in the experiment that when the torque was increased to 26.7 Nm at a speed of 800 rpm, the DC-link voltage showed sustained oscillations as depicted in Fig. 10 in [52]. This is in very close agreement with the critical torque of 27.6 Nm determined from μ analysis. Thus, both experimental and simulation results confirm the validity of the proposed modelling approach.

5.4.5 Discussion

μ analysis directly provides an explicit measure of the amount of variability that is allowed in uncertain parameters for the system to remain stable. For the case under study, the robust stability margin equal to 0.42 implies that maintaining the normalised torque within 42 % of its nominal value ensures system stability. This information is very useful and can directly be employed in the design of the electrical power systems. For instance, in order to ensure that the system under study remains stable over the whole uncertainty range, μ should be less than 1. One way to do this is to limit the operating range to $T_o = 20$ Nm \pm 38%, (which can be derived from $T_o = T_{oo} \pm T_{oo} T_{var} \delta_{T_{cr}}$). However, if the operating range is to be maintained within 20 Nm \pm 90%, the input filter parameters L_F and C_F can be modelled as uncertainties in the procedure for filter design.

Furthermore, the SSV method is less demanding for a user. The only inputs that are to be provided to the software are firstly nominal values and a variation range of uncertain parameters, and then an equivalent linear state space model.

In contrast, the classical eigenvalue approach applied in [52] to determine the critical torque of the PM machine drive is not direct and involves an extensive process. Firstly, the operating range is divided into a finite number of points. Then, for each operating point, numerical linearisation is performed and eigenvalues are calculated. The iterative process has to be further refined until the critical parameter value is obtained to a satisfactory accuracy.

The modelling methodology proposed in this work has been successfully applied to the power system under study. It is still to be tested on system-level architectures where source and load subsystems, of the order of the EPS under consideration, are interconnected.

5.5 Effect of parameter variations on stability robustness

In the previous section, we found that stability can be guaranteed for the system under study up to the maximum power of 2.6 kW. In this section, the effect of parameter variations on the destabilising power is investigated by using the μ method that was described in section 5.4. In particular this analysis includes variations in system frequency, bandwidth of the DC-link voltage filter and natural frequency of the speed loop. All the other system parameters are kept constant as given in Table 5.1 unless specified otherwise. The results from μ analysis are verified against experimental results reported in [52].

5.5.1 System frequency

While conventional aircraft tends to use constant frequency ac power, the future aircraft is more likely to operate on variable frequency ac supply, typically ranging between 360 Hz and 720 Hz [69]. Based on the use of power electronic converters, the aircraft generator is allowed to rotate at variable speed, thus eliminating the need for constant speed drive. Variable frequency supply can lead to an increase in efficiency [69]. It is important to analyse how stability robustness of the power system is affected by variations in system frequency [70]. For the purpose of illustration, μ analysis is applied to determine the critical torque that destabilises the power system, when the system frequency is allowed to vary between 1 Hz and 300 Hz . For every frequency under study, the uncertain torque is as defined in Table 5.2. The system is investigated with no DC-link voltage filter. The critical power is then computed from the critical torque, determined from μ analysis at each frequency point, based on $P = T_{cr}w_r/\eta$. Fig. 5.11 depicts the results from μ analysis. Further, a number of experiments were performed on the system to identify the destabilising power for frequencies of 50 Hz , 100 Hz , 200 Hz and 300 Hz . Fig. 5.11 shows the experimental results which have also been reported in Fig. 11 in [52]. There is a close agreement between the μ analysis predictions and the experimental results as can be seen in Fig. 5.11. It can be noted that an increase in system frequency causes an improvement in system stability.

5.5.2 Bandwidth of the DC-link voltage filter

The DC-link voltage v_{out} is filtered for the computation of the modulation index in the digital signal processor (DSP) as shown in Fig. 5.2 [52],[71]. The critical torque is determined for different values of the DC-link voltage filter (f_{cutoff}) ranging from 0 Hz to 300 Hz . The critical power is then computed from the critical torque, predicted by μ analysis at the different values of f_{cutoff} , based on $P = T_{cr}w_r$. Fig. 5.12 depicts the power stability threshold obtained from μ analysis.

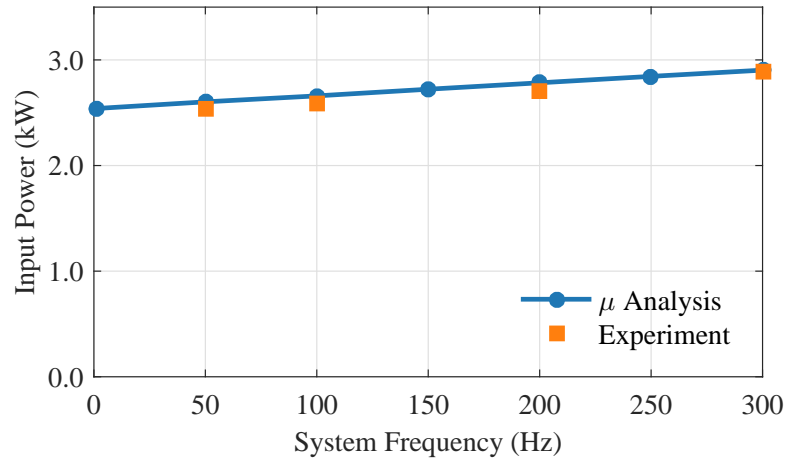


Figure 5.11: Experimental results and μ predictions of critical power with varying system frequency

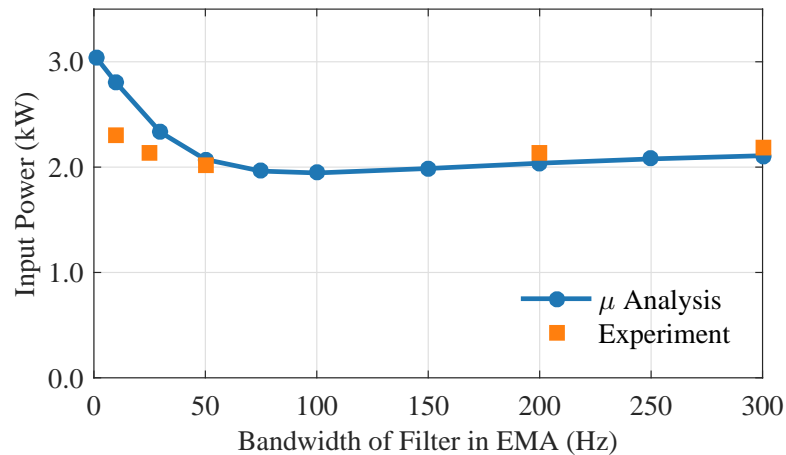


Figure 5.12: Experimental results and μ predictions of critical power with varying bandwidth of the DC-link voltage filter

In addition, the critical power was measured experimentally at the shaft of the motor for f_{cutoff} of 10 Hz, 25 Hz, 50 Hz, 200 Hz and 300 Hz. Fig. 5.12 depicts the experimental results which have also been reported in Fig. 12 in [52]. These experimental results agree fairly well with μ analysis predictions as can be noted in Fig. 5.12. It

can be noted that the effect of the DC-link voltage filter bandwidth on stability robustness is not monotonic and is around 75 Hz at the point where the system is the least robustly stable.

5.5.3 Natural frequency of the speed loop

μ analysis is applied to determine the destabilising power for different values of natural frequency of the speed loop (f_n) ranging from 1 Hz to 25 Hz. The DC-link voltage filter bandwidth is fixed at 50 Hz. Fig. 5.13 shows the results from μ analysis. Moreover, the critical power was measured experimentally at the shaft of the motor when f_n was set at 5 Hz, 10 Hz, 15 Hz and 20 Hz. Fig. 5.13 shows the experimental results which have also been reported in Fig. 13 in [52]. The experimental results agree closely with the μ analysis predictions as can be seen in Fig. 5.13. The system stability is seen to degrade with an increase in the natural frequency of the speed loop.

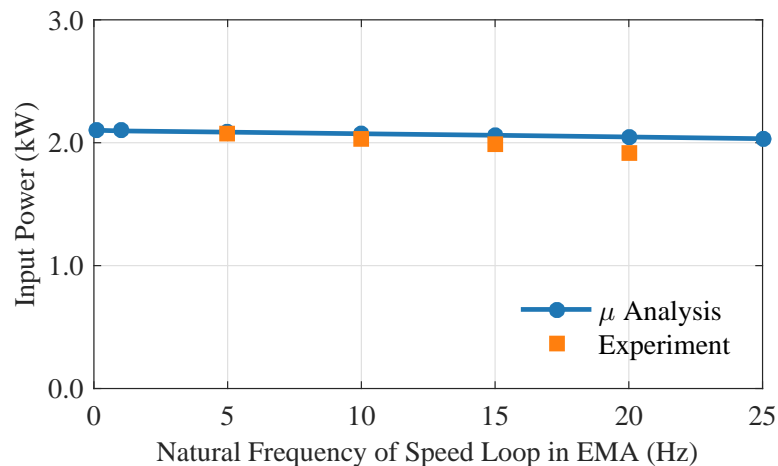


Figure 5.13: Experimental results and μ predictions of critical power with varying natural frequency of the speed loop

5.5.4 Discussion

This section has demonstrated how parameter variations can affect system stability. The μ analysis results match closely the experimental results which were reported in [52] and also shown in Fig. 5.11 - 5.13 for the sake of completeness. This validates the methodology proposed in this paper.

5.6 Conclusion

This chapter has demonstrated how the the μ method, which is generally employed for linear models, can be applied to non-linear system models. The study has been applied it to the PM machine based electromechanical actuation system, which is widely used for MEA application.

- This study has developed a modelling methodology that extends the applicability of the μ approach to non-linear system models. The novelty of the method is that it converts a non-linear system into an equivalent linear model that is valid for all defined operating points and parameter uncertainties of the system. In addition it fully accounts for non-linear dependencies of operating points on parameter uncertainties. The study has illustrated how the generalised model, in symbolic form, converts to specific linear models about distinct operating points depending on the values assigned to the system parameters and inputs. The methodology has been developed based on the symbolic linearisation of the non-linear model around an arbitrary equilibrium point. Further, it has required that all the elements of the linearised model be explicitly expressed in terms of determinate parameters and inputs only.
- This approach, with respect to classical methods, eliminates the need for exhaustive linearisation and extensive iterations under parameter variations. The design engineer only requires an equivalent linear model and a definition of the

uncertain parameters, so as to obtain a direct measure of robust stability margin of the non-linear system.

- In addition, the modelling approach reduces conservativeness in stability assessment. This has been achieved by fully catering for the non-linear dependencies of operating points on parameter uncertainties.
- The proposed modelling methodology has been verified through the μ analysis of a 4 kW PM machine drive system, which has successfully predicted the critical torque that causes system instability. The investigation has included uncertainties in load, with variations in system frequency, bandwidth of the DC-link filter voltage and natural frequency of the speed loop. Further, all μ analysis predictions have been validated based on experimental results reported in [52].

Electrical power systems are generally represented by non-linear models. Through the development of the proposed modelling methodology, this work has extended the applicability of the μ approach to non-linear system models.

Chapter 6

Conclusions

Power electronics is at the heart of the technology transition that is required to put transportation on a more sustainable pathway. The “more electric transport” is one of the main long term solutions to reducing CO_2 emissions and preserving fossil fuel reserves. The key problem with power electronic driven loads lies in their susceptibility to instability, which may be further compromised by uncertainties inherently present in these systems. There is a need to adopt robust analysis techniques to assess and ensure stability of these generally non-linear systems in the face of uncertainties. While power electronics is fast evolving, the stability analysis techniques for these systems are still widely based on classical methods, which treat the physical system as a fixed model. However, it is necessary to adopt new techniques that include the uncertain nature of the physical systems. This work has proposed to use the μ approach as a practical method that assesses the stability robustness of such systems in the face of uncertainties.

By working with the uncertain model of the physical system, the μ method justifiably takes into account all considered structured uncertainties in the system, while producing reliable robust stability assessment results. However, three main limitations, as identified in this work, tend to make the approach hard to apply.

- First is the complexity of its underlying theoretical framework.
- Secondly, practical approaches to applying the method to power electronic systems seem lacking in the literature. This include the necessary methodology to be employed through the use of associated software.
- Thirdly, the μ method is generally applied to linear systems while most systems analysed have non-linear behaviour.

This work has addressed these three shortcomings, as will be discussed in the following section. In doing so, it has demonstrated the applicability, flexibility and effectiveness of the μ method, while realising the full benefits of the approach.

6.1 Research outcomes

The research findings of the thesis are presented herein. The main contributions along with the implications of the study are emphasised.

6.1.1 Theoretical aspects

Chapter 2 has provided a clear and thorough examination of the key concepts of the μ framework, through application to the well established *RLC* example system. These concepts, often considered complex, are not always examined from the engineering viewpoint in the literature. The study has clearly illustrated the modelling technique of LFT, and the robust stability margin ($1/\mu$). The principle of μ , as well as the attributes and limitations of its bounds, have been treated in a comprehensive manner. Further, the computational limitations of the μ method and the possible solutions have been discussed. This part of the work has thus brought a clearer understanding of the μ theorem, which is essential in both the application of the method and in the interpretation of results.

The work developed in Chapter 3 is novel in that it has extended and applied the concept of the hypercube, to show the significance and usefulness of the robust stability measure μ with respect to single and multiple parametric uncertainties. The hypercube is presented at a purely conceptual level in the literature. This study has constructed hypercubes of a basic electrical power system connected to an ideal CPL, when it is subject to multiple parametric uncertainties, based on data from μ analysis. The CPL is pivotal in the stability studies of PE systems. In addition, this study has translated the μ results from the frequency domain to the parametric domain, making μ easier to work with.

Through the generated hypercubes of the considered system, it has been shown how μ identifies the largest parametric space within which stability robustness is guaranteed. More specifically, for a system subject to N parametric uncertainties, the μ approach provides the largest hypercube of dimension N , centred about the nominal point and of coordinate size $1/\mu$, within which the system can be guaranteed to be robustly stable. $1/\mu$ is a measure of the robust stability margin of the EPS. The hypercube becomes the largest line segment, square and cube of coordinate size $1/\mu$, for a system subject to a single, two and three parametric uncertainties respectively. The hypercube concept, as presented in Chapter 3, can be further explored and applied to a large range of uncertain systems. For instance, the hypercube can be utilised for the optimum selection of parameters in the design of robustly stable systems.

Following the application of the hypercube concept and the translation of the μ results in the more perceivable parametric space, this work has helped to make the μ method easier to understand and apply, particularly for systems with multiple parametric uncertainties.

6.1.2 Practical aspects

Chapter 4 has presented a number of practical approaches to incorporate uncertainties in μ analysis of power electronic systems, by using the widely employed DC/DC

buck converter. It has demonstrated the importance of incorporating uncertainties in stability assessment and the necessity for adopting a robust analysis tool, such as the μ approach.

μ analysis has been applied to predict the destabilising load of the buck converter system, for different values of line resistance. The results have been validated in experiment both in the time domain and in the frequency domain. Although μ analysis results have been validated in the literature, the studies generally pertain to large power systems rather than power electronic systems. The study has shown that a decrease in line impedance has a negative impact on the robust stability margin of the EPS. The practical limitations of applying the classical Middlebrook criterion and the more formal Nyquist stability criterion to the experimental buck converter have been discussed.

The study has demonstrated how key uncertainties, such as extreme operating temperature variations, can be included in μ analysis of the buck converter, in order to obtain more reliable results. It has been shown that the consequence of neglecting operating temperature variations may lead to highly optimistic but often unreliable results. Given that electrical systems of the MET may be subject to wide fluctuations in operating temperature, it is crucial to include this type of uncertainty in the system stability assessment for these safety critical applications.

The study has shown how the μ approach can be used to its full potential by including model uncertainties in the analysis, and hence justifiably catering for the uncertain nature of the physical system. These aspects may have been suggested in the literature, but they have not been applied. Further, the findings have shown that robust stability margin tends to be larger, if model uncertainties can be defined within narrower range. In all cases, the results tend to be more reliable, if uncertainties are included in the analysis, rather than using the nominal system model with fixed parameter values.

The method required to apply the μ method, through the use of the software namely MATLAB[®] Robust Stability Toolbox, has been presented clearly such that it can be easily reapplied to other systems. This aspect is often left out in the literature. Furthermore, the effect of the size of the problem on computational time has been discussed through certain cases studied in this chapter.

The study has important implications. The approach can bring flexibility to a user, by allowing the user to choose the degree of accuracy of the parameters in a system model, depending on available data. The user may even define system non-linearities as uncertain elements, in order to reduce the complexity of the system model. Parasitics, generally hard to measure, can be treated as uncertainties. The robust stability margin may be tighter when the parameters are known with less accuracy and defined within a wider range of values. Yet, the results tend to be more reliable, which may justify the approach from a practical viewpoint.

This chapter has presented practical approaches to μ analysis in a manner that is clear enough to enable a user to apply the method to similar or more complex systems, and to extend the applications to include yet further sources of uncertainties.

6.1.3 Application to non-linear systems

The last part of the work in Chapter 5 has developed a modelling methodology that enables the μ method to be applied to non-linear systems. The novelty of the method is that it converts a non-linear system into a unique equivalent linear model, while fully catering for system non-linearities. The equivalent linear model is valid for μ analysis over a range of defined operating points and system parameters. The generalised model represents the complete set of all possible linear models that can result due to variations in uncertain parameters and operating points.

The strength of the approach, over classical methods, is that it eliminates the need for exhaustive linearisation and iterations. The μ approach requires only the equivalent

linear model together with its nominal data and uncertain parameters upper and lower limits, in order to provide a direct and reliable measure of robust stability margin.

In addition, the modelling approach reduces conservativeness in stability assessment as it preserves all dependencies of varying operating points on parameter uncertainties. This may contribute to the design of more optimised systems, for instance through the selection of smaller filters.

μ analysis has been applied to the developed equivalent linear model of a 4 kW PM machine based electromechanical actuation system, and has successfully predicted the critical torque that causes system instability. The investigation has included uncertainties in load, with variations in system frequency, bandwidth of the DC-link filter voltage and natural frequency of the speed loop. Further, the experimental results reported in [52] have allowed the validation of both the μ predictions and the modelling methodology.

This last part of the work has demonstrated that the μ method can effectively be extended to non-linear systems, through the use of the experimentally validated and proposed modelling approach.

6.1.4 Research summary

The μ approach is an effective method that can be adopted for the robust stability assessment of electrical power systems for the MET. Yet, the method is not widely employed due to certain limiting factors. One drawback relates to the complexity of its theoretical framework. The practical approaches to applying the method to power electronic systems are not adequately covered in the literature. In addition, the μ approach is not directly applicable to non-linear system models, that are generally used to represent physical systems. With the aim to making the approach more applicable, this work has addressed these key limitations. It has provided a comprehensive understanding of the μ theoretical framework and has presented practical approaches

to employing the μ method, and in addition has extended application of the approach to non-linear systems. This has been done in manner that is comprehensible enough to make it more application-friendly while offering the possibility of it being extended to similar or more complex systems. Based on the strong foundation laid in this work, it is the author's belief that the μ approach can be used as commonly as classical techniques, and to great effect.

6.2 Future research

This thesis is hoped to be a stepping stone to future studies, with the possibilities of deepening knowledge of the subject and broadening the area of application. Three main areas, amongst many others, may be explored further.

- First, the μ approach may be applied on system-level architectures, where source and load subsystems, of the order of the systems analysed in this work, are interconnected. It will be interesting to investigate how the local stability of a subsystem affect the global stability of the whole network, based on the μ approach.
- Secondly, μ sensitivity, which is a related feature of the μ approach, can be studied. μ sensitivity can be employed to identify which uncertain parameters in the system model is most critical to stability robustness. This knowledge may be used to narrow stability assessment with respect to the critical elements of the model, and further reduce size and complexity of the uncertain model.
- Finally and very importantly, there needs to be a continuous investigation into currently available computational tools for μ analysis. Tools to optimise any state space system in order to obtain smaller uncertainty matrices as well as order reduction methods are to be explored. These include but are not limited to MATLAB[®] Robust Stability Toolbox and ONERA[®] Skew mu toolbox. Finding the right tools may significantly improve the accuracy of the μ bounds

and decrease computational burden to reasonable limits, which is particularly important for assessing large scale problems.

By making the μ method more applicable for the robust stability of power electronic systems, this thesis has provided a strong basis for addressing the issue of stability for the larger and more complex electrical networks of the more electric transport.

References

- [1] I. E. Agency, *Transport Energy and CO₂: Moving Towards Sustainability*. OECD Publishing, 2009.
- [2] U. DfT, “Low carbon transport: A greener future. a carbon reduction strategy for transport,” 2009.
- [3] L. Chapman, “Transport and climate change: a review,” *Journal of transport geography*, vol. 15, no. 5, pp. 354–367, 2007.
- [4] I. Moir and A. Seabridge, *Aircraft systems: mechanical, electrical and avionics subsystems integration*, vol. 52. John Wiley & Sons, 2011.
- [5] J. A. Rosero, J. A. Ortega, E. Aldabas, and L. Romeral, “Moving towards a more electric aircraft,” *IEEE Aerospace and Electronic Systems Magazine*, vol. 22, pp. 3–9, March 2007.
- [6] T. G. Wilson, “The evolution of power electronics,” in *Applied Power Electronics Conference and Exposition, 1999. APEC '99. Fourteenth Annual*, vol. 1, pp. 3–9 vol.1, Mar 1999.
- [7] K. Areerak, *Modelling and stability analysis of aircraft power systems*. PhD thesis, University of Nottingham, 2009.
- [8] K. N. Areerak, S. V. Bozhko, G. M. Asher, L. D. Lillo, and D. W. P. Thomas, “Stability study for a hybrid ac-dc more-electric aircraft power system,” *IEEE Transactions on Aerospace and Electronic Systems*, vol. 48, pp. 329–347, Jan 2012.

-
- [9] K. N. Areerak, S. V. Bozhko, G. M. Asher, and D. W. P. Thomas, "Dq-transformation approach for modelling and stability analysis of ac-dc power system with controlled pwm rectifier and constant power loads," in *Power Electronics and Motion Control Conference, 2008. EPE-PEMC 2008. 13th*, pp. 2049–2054, Sept 2008.
- [10] F. Barruel, A. Caisley, N. Retiere, and J. L. Schanen, "Stability approach for vehicles dc power network: Application to aircraft on-board system," in *2005 IEEE 36th Power Electronics Specialists Conference*, pp. 1163–1169, June 2005.
- [11] K. N. Areerak, S. V. Bozhko, G. M. Asher, and D. W. P. Thomas, "Stability analysis and modelling of ac-dc system with mixed load using dq-transformation method," in *2008 IEEE International Symposium on Industrial Electronics*, pp. 19–24, June 2008.
- [12] A. B. Jusoh, "The instability effect of constant power loads," in *Power and Energy Conference, 2004. PECon 2004. Proceedings. National*, pp. 175–179, IEEE, 2004.
- [13] R. W. Erickson and D. Maksimovic, *Fundamentals of power electronics*. Springer Science & Business Media, 2001.
- [14] R. D. Middlebrook, "Input filter considerations in design and application of switching regulators," *IAS Record*, 1976, 1976.
- [15] A. Riccobono and E. Santi, "Comprehensive review of stability criteria for DC power distribution systems," *Industry Applications, IEEE Transactions on*, vol. 50, no. 5, pp. 3525–3535, 2014.
- [16] A. M. Rahimi and A. Emadi, "An analytical investigation of dc/dc power electronic converters with constant power loads in vehicular power systems," *Vehicular Technology, IEEE Transactions on*, vol. 58, no. 6, pp. 2689–2702, 2009.
- [17] S. Sudhoff and O. Wasynczuk, "Analysis and average-value modeling of line-commutated converter-synchronous machine systems," *Energy Conversion, IEEE Transactions on*, vol. 8, no. 1, pp. 92–99, 1993.

-
- [18] A. Emadi, A. Khaligh, C. H. Rivetta, and G. A. Williamson, "Constant power loads and negative impedance instability in automotive systems: definition, modeling, stability, and control of power electronic converters and motor drives," *IEEE Transactions on Vehicular Technology*, vol. 55, pp. 1112–1125, July 2006.
- [19] Y. Che, X. Liu, and Z. Yang, "Large signal stability analysis of aircraft electric power system based on averaged-value model," in *2015 6th International Conference on Power Electronics Systems and Applications (PESA)*, pp. 1–5, Dec 2015.
- [20] A. Griffo and J. Wang, "Large signal stability analysis of 'more electric' aircraft power systems with constant power loads," *IEEE Transactions on Aerospace and Electronic Systems*, vol. 48, no. 1, pp. 477–489, 2012.
- [21] S. Rosado, R. Burgos, F. Wang, and D. Boroyevich, "Large-signal stability analysis in power systems with a synchronous generator connected to a large motor drive," in *2007 IEEE Electric Ship Technologies Symposium*, pp. 42–47, May 2007.
- [22] H. Zhang, C. Saudemont, B. Robyns, and M. Petit, "Comparison of technical features between a more electric aircraft and a hybrid electric vehicle," in *2008 IEEE Vehicle Power and Propulsion Conference*, pp. 1–6, Sept 2008.
- [23] G. F. Franklin, J. D. Powell, A. Emami-Naeini, and J. D. Powell, *Feedback control of dynamic systems*, vol. 2. Addison-Wesley Reading, 1994.
- [24] R. C. Dorf and R. H. Bishop, "Modern control systems," 1998.
- [25] M. R. Roussel, "Stability analysis for odes," *Nonlinear Dynamics, lecture notes. University Hall, Canada*, 2005.
- [26] W. E. Sollecito and D. A. Swann, "Computer evaluation of high-temperature aircraft a-c electrical system designs," *Transactions of the American Institute of Electrical Engineers, Part II: Applications and Industry*, vol. 78, pp. 434–444, Jan 1960.

-
- [27] J. Doyle, "Analysis of feedback systems with structured uncertainties," in *IEE Proceedings D (Control Theory and Applications)*, vol. 129, pp. 242–250, IET, 1982.
- [28] J. C. Doyle, B. A. Francis, and A. Tannenbaum, *Feedback control theory*, vol. 1. Macmillan Publishing Company New York, 1992.
- [29] M. Green and D. J. Limebeer, *Linear robust control*. Courier Corporation, 2012.
- [30] S. D. Sudhoff, S. F. Glover, P. T. Lamm, D. H. Schmucker, and D. Delisle, "Admittance space stability analysis of power electronic systems," *Aerospace and Electronic Systems, IEEE Transactions on*, vol. 36, no. 3, pp. 965–973, 2000.
- [31] M. Kuhn, Y. Ji, and D. Schrder, "Stability studies of critical DC power system component for More Electric Aircraft using mu sensitivity," in *Control & Automation, 2007. MED'07. Mediterranean Conference on*, pp. 1–6, IEEE, 2007.
- [32] J. Elizondo, R. Y. Zhang, J. K. White, and J. L. Kirtley, "Robust small signal stability for microgrids under uncertainty," in *Power Electronics for Distributed Generation Systems (PEDG), 2015 IEEE 6th International Symposium on*, pp. 1–8, IEEE, 2015.
- [33] P. M. Young, M. P. Newlin, and J. C. Doyle, " μ analysis with real parametric uncertainty," in *Decision and Control, 1991., Proceedings of the 30th IEEE Conference on*, pp. 1251–1256, IEEE, 1991.
- [34] G. Ferreres, *A practical approach to robustness analysis with aeronautical applications*. Springer Science & Business Media, 1999.
- [35] K. Zhou, J. Doyle, and K. Glover, *Robust and Optimal Control*. Feher/Prentice Hall Digital and, Prentice Hall, 1996.
- [36] S. Skogestad and I. Postlethwaite, *Multivariable Feedback Control: Analysis and Design*. Multivariable Feedback Control: Analysis and Design, Wiley, 2005.
- [37] A. Packard and J. Doyle, "The complex structured singular value," *Automatica*, vol. 29, no. 1, pp. 71–109, 1993.

-
- [38] G. J. Balas, J. C. Doyle, K. Glover, A. Packard, and R. Smith, “ μ -analysis and synthesis toolbox,” *MUSYN Inc. and The MathWorks, Natick MA*, 1993.
- [39] G. Ferreres, J.-M. Biannic, and J.-F. Magni, “A skew mu toolbox (smt) for robustness analysis,” in *Computer Aided Control Systems Design, 2004 IEEE International Symposium on*, pp. 309–314, Sept 2004.
- [40] A. Fabrizio, C. Roos, and J.-M. Biannic, “A detailed comparative analysis of μ lower bound algorithms,” in *European Control Conference 2014*, 2014.
- [41] A. Varga, G. Looye, D. Moormann, and G. Gräbel, “Automated generation of LFT-based parametric uncertainty descriptions from generic aircraft models,” *Mathematical and Computer Modelling of Dynamical Systems*, vol. 4, no. 4, pp. 249–274, 1998.
- [42] G. Balas, R. Chiang, A. Packard, and M. Safonov, “Robust control toolbox,” *For Use with Matlab. User’s Guide, Version*, vol. 3, 2005.
- [43] R. Castellanos, C. Juarez, J. Hernandez, and A. Messina, “Robustness analysis of large power systems with parametric uncertainties,” in *Power Engineering Society General Meeting, 2006. IEEE*, pp. 8–pp, IEEE.
- [44] M. Djukanovic, M. Khammash, and V. Vittal, “Application of structured singular value theory for robust stability and control analysis in multimachine power systems. ii. numerical simulations and results,” *IEEE Transactions on Power Systems*, vol. 13, pp. 1317–1322, Nov 1998.
- [45] R. Castellanos, A. Messina, and H. Sarmiento, “Robust stability analysis of large power systems using the structured singular value theory,” *International Journal of Electrical Power & Energy Systems*, vol. 27, no. 5, pp. 389–397, 2005.
- [46] M. Djukanovic, M. Khammash, and V. Vittal, “Application of the structured singular value theory for robust stability and control analysis in multimachine power systems. i. framework development,” *IEEE Transactions on Power Systems*, vol. 13, pp. 1311–1316, Nov 1998.

-
- [47] S. Chen and O. P. Malik, "Power system stabilizer design using μ -synthesis," *IEEE Transactions on Energy Conversion*, vol. 10, pp. 175–181, Mar 1995.
- [48] A. Haddadi, B. Boulet, A. Yazdani, and G. Joós, "A μ -based approach to small-signal stability analysis of an interconnected distributed energy resource unit and load," *IEEE Transactions on Power Delivery*, vol. 30, no. 4, pp. 1715–1726, 2015.
- [49] D.-W. Gu, *Robust control design with MATLAB®*, vol. 1. Springer Science & Business Media, 2005.
- [50] G. J. Balas, J. C. Doyle, K. Glover, A. Packard, and R. Smith, " μ -analysis and synthesis toolbox: For use with matlab," 2001.
- [51] S. Buso, "Design of a robust voltage controller for a buck-boost converter using μ -synthesis," *IEEE Transactions on Control Systems Technology*, vol. 7, pp. 222–229, Mar 1999.
- [52] K.-N. Areerak, S. Bozhko, L. de Lillo, G. Asher, D. Thomas, A. Watson, and T. Wu, "The stability analysis of ac-dc systems including actuator dynamics for aircraft power systems," in *Power Electronics and Applications, 2009. EPE '09. 13th European Conference on*, pp. 1–10, Sept 2009.
- [53] S. Sumsurooah, M. Odavic, and D. Boroyevich, "Modelling and robust stability analysis of uncertain systems," in *Proceedings of the 2013 Grand Challenges on Modeling and Simulation Conference*, p. 13, Society for Modeling & Simulation International, 2013.
- [54] S. Skogestad and I. Postlethwaite, *Multivariable feedback control: analysis and design*, vol. 2. Wiley New York, 2007.
- [55] FrontlineSolvers, "Optimisation problem types - convex optimization." [Online]. Available: <http://www.solver.com/convex-optimization>. [Accessed: 13 July 2016].
- [56] J. Magni, "User manual of the linear fractional representation toolbox version 2.0," 2006.

-
- [57] C. M. Belcastro and B.-C. Chang, "On parametric uncertainty modeling for real parameter variations," in *Decision and Control, 1992., Proceedings of the 31st IEEE Conference on*, pp. 674–679, IEEE, 1992.
- [58] S. Sumsurooah, M. Odavic, and S. Bozhko, "Development of LFT-based models for robust stability analysis of a generic electrical power system over all operating conditions," in *Electrical Systems for Aircraft, Railway, Ship Propulsion and Road Vehicles (ESARS), 2015 International Conference on*, pp. 1–6, IEEE, 2015.
- [59] J. Flower, C. Hodge, and Honorary, "Stability and transient-behavioural assessment of power-electronics-based dc-distribution systems: Part 1: The root-locus technique," *Journal of Marine Engineering & Technology*, vol. 3, no. 2, pp. 13–21, 2004.
- [60] H. J. Zhang, "Modeling and loop compensation design of switching mode power supplies," *Power Electronics Technology*, 2015.
- [61] M. Hassan and A. A. Elbaset, "Small-signal matlab/simulink model of dc-dc buck converter using state-space averaging method,"
- [62] S. Sumsurooah, M. Odavic, and S. Bozhko, "A modeling methodology for robust stability analysis of nonlinear electrical power systems under parameter uncertainties," *IEEE Transactions on Industry Applications*, vol. 52, pp. 4416–4425, Sept 2016.
- [63] CPES, "Modeling and control design of dc/dc converters - a cpes professional short course at virginia tech: Laboratory manual, unpublished."
- [64] D. Mattingly, "Designing stable compensation networks for single phase voltage mode buck regulators," *Intersil Technical Brief*, 2003.
- [65] D. Meeks, "Loop stability analysis of voltage mode buck regulator with different output capacitor types—continuous and discontinuous modes," *Texas Instruments Application Report, SLVA301*, pp. 1–36, 2008.

-
- [66] C. M. Wildrick, F. C. Lee, B. H. Cho, and B. Choi, "A method of defining the load impedance specification for a stable distributed power system," *IEEE Transactions on Power Electronics*, vol. 10, no. 3, pp. 280–285, 1995.
- [67] S. Sumsurooah, M. Odavic, S. Bozhko, and D. Boroyevich, "Stability and robustness analysis of a dc/dc power conversion system under operating conditions uncertainties," in *Industrial Electronics Society, IECON 2015 - 41st Annual Conference of the IEEE*, pp. 003110–003115, Nov 2015.
- [68] A. Varga, "Balancing free square-root algorithm for computing singular perturbation approximations," in *Decision and Control, 1991., Proceedings of the 30th IEEE Conference on*, pp. 1062–1065, IEEE, 1991.
- [69] J. Chang and A. Wang, "New vf-power system architecture and evaluation for future aircraft," *IEEE Transactions on Aerospace and Electronic Systems*, vol. 42, pp. 527–539, April 2006.
- [70] K. N. Areerak, T. Wu, S. V. Bozhko, G. M. Asher, and D. W. P. Thomas, "Aircraft power system stability study including effect of voltage control and actuators dynamic," *IEEE Transactions on Aerospace and Electronic Systems*, vol. 47, pp. 2574–2589, OCTOBER 2011.
- [71] L. de Lillo, P. Wheeler, L. Empringham, C. Gerada, *et al.*, "A power converter for fault tolerant machine development in aerospace applications," in *Power Electronics and Motion Control Conference, 2008. EPE-PEMC 2008. 13th*, pp. 388–392, IEEE, 2008.

Appendix A

Computational aids

This appendix provides some computational aids in using MATLAB[®] Robust Stability Toolbox for the evaluation of robust stability. Further details may be found in MATLAB[®] documentation.

A.1 μ analysis

The function ‘robuststab(ufrd(sys,omega))’ performs both LFT operation and μ analysis of the considered system. Prior to applying the function, the following elements must be defined:

- The nominal parameters
- The uncertain parameters using the function ‘ureal’
- The frequency grid as ‘omega=logspace(w_{min} , w_{max} , n)’ where w_{min} , w_{max} are the minimum and maximum frequency and n is the number of points in the grid.
- The system ‘sys’ in state space configuration and symbolic form

A.2 Problem of convergence of the μ lower bound

One known problem is that the μ lower bound may fail to converge when the uncertain parameters are purely real [38],[42],[53]. This issue has been encountered in this work for case studies with a single parametric uncertainty. A small complexity of value up to 1%, added to the real parametric uncertainty by using the command “complexify”, has proved to be sufficient to make the μ lower bound converge [53]. The use of the command is shown below. The term ‘sys’ refers to the uncertain system in state space configuration and symbolic form. μ analysis is performed on the system defined by ‘sysreg’ instead of ‘sys’.

- `alpha=0.01`
- `sysreg = complexify(sys,alpha,'ultidyn');`

It is to be added that the MATLAB[®] command, shown hereunder for the parameter r , may be used to extract the real value of the critical r , after excluding the complex part. The variables ‘destabunc’ and ‘stabmarg.DestabilizingFrequency’ contain information regarding the critical value of r and the critical frequency respectively.

- `real(destabunc.r + freqresp(destabunc.r_cmpxfy,stabmarg.DestabilizingFrequency))`

An alternative algorithm in MATLAB Robust Control Toolbox, that makes use of the coordinate-wise optimization (i.e. the “gain-based lower bound” method) can be employed for good convergence of the μ lower bound [42]. It does not require the use of complexity. The method is reported to be slower than the approach with added complexity [42]. Furthermore, it has been reported that different runs of the algorithm may produce different values of the μ lower bound [40].

A.3 Accuracy of μ bounds

A rough frequency grid can initially be chosen to identify the peak value of the μ bounds. It has been found that the accuracy of the μ bounds can be further improved by rerunning the analysis but this time specifying a tighter frequency grid around the critical frequency of μ . In some cases, making the frequency grid denser also improves the results.

A.4 Accuracy of the upper bound

The gap between the lower and upper bound was initially large for case study II in both chapters 2 and 3. Using the computation option 'a', which calculates the upper bound with greater accuracy, lead the gap to reduce, in this case. The command has to be modified as shown below. Of note is that this option did not work for the larger systems analysed in chapters 4 and 5, since it is computationally expensive.

- `robuststaboptions('Mussv','a')`
- `robuststab(ufrd(sys,omega),ropt)`

Appendix B

Experimental measurements of input impedance

The network analyser has been employed for the experimental measurements of certain small signal transfer functions of the closed loop buck converter in Chapter 4 [13],[63]. In section 4.3, the equipment has been used to measure the loop gain, input impedance (Z_i) and output impedance (Z_o) of the buck converter, in view of refining the system model of the EPS. In section 4.4.3, Z_i and Z_o of the buck converter have been measured by means of the equipment, in order to assess the stability of the EPS, based on Nyquist stability criterion. This appendix describes how the network analyser is used to experimentally measure the input impedance of the buck converter.

The input impedance is the transfer function describing how perturbation in the input current \hat{i}_{in} affects the input voltage \hat{v}_{in} . The experimental set-up for the small signal input impedance measurement is shown in Fig. B.1 and B.2. The network analyser injects a small signal at a desired location in the considered system from its output denoted as *OUT*, as depicted in Fig. B.2. It then takes measurements of interest through its inputs denoted as *R* and *A*, as shown in Fig. B.2. The injection terminals of the network analyser is connected to the buck converter through an

isolating transformer and a series connected DC capacitor, as depicted in Fig. B.1 and B.2. The isolating transformer is required so as to prevent the injected current from flowing back to the source through the ground terminal of the measurement probes. Any leakage current through the ground causes a voltage drop in the probes which may reduce accuracy in measurements. Besides, the DC blocking capacitor acts as a short for high frequency signals and as an open circuit for low frequency signal. Hence, it prevents the DC and low frequency signals in the injection voltage from upsetting the input DC source voltage of the converter.

As depicted in Fig. B.1 and B.2, the network analyser injects a sinusoidal source of controllable amplitude and frequency to the input of the buck converter. Using a current injection caused most of the current to flow into the low impedance source side. Hence a series voltage injection was used to inject perturbation into the circuit through the gate of a FET. In order to obtain smooth waveforms of transfer functions, power of around 15 *dB* was injected for the measurements of Z_i , while only -5 *dB* was required for the loop gain measurements. Following the small signal injection, the input voltage \hat{v}_{in} and the current \hat{i}_{in} were measured at intervals of 30 *Hz* over a range of frequency between 100 *Hz* and 50 *kHz*. The current \hat{i}_{in} was obtained by measuring the voltage \hat{v}_r across a resistance of 1 Ω , as shown in Fig. B.1 and B.2. The ratio of $\hat{v}_{in}/\hat{i}_{in}$ produces the frequency response of Z_i , as given in (B.1) and (B.2).

$$\text{Magnitude plot } |Z_i| = \left| \frac{\hat{v}_{in}}{\hat{i}_{in}} \right| \quad (\text{B.1})$$

$$\text{Phase plot } \angle Z_i = \angle \frac{\hat{v}_{in}}{\hat{i}_{in}} \quad (\text{B.2})$$

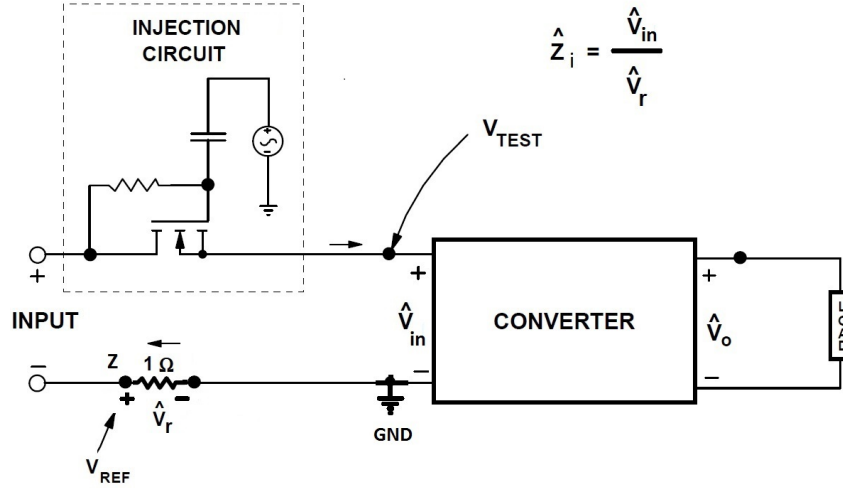


Figure B.1: Practical implementation of input impedance measurements

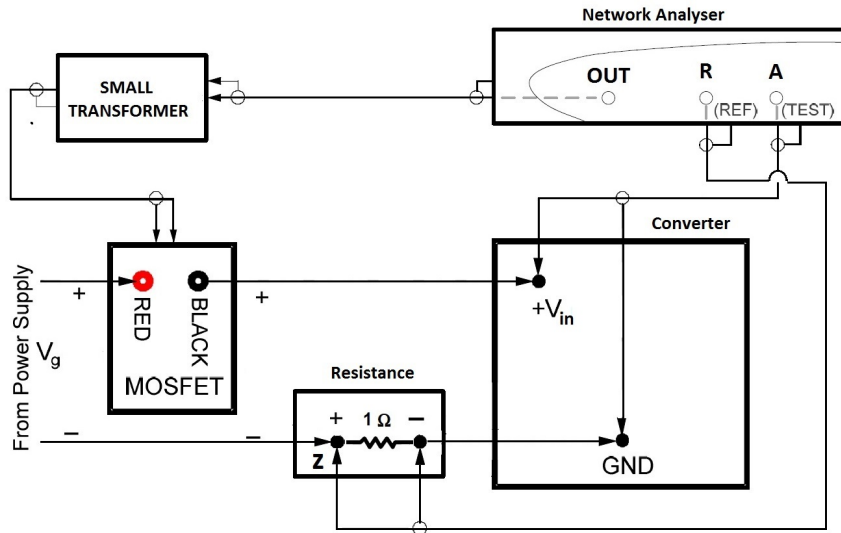


Figure B.2: Equipment set-up for input impedance measurements